The Impact of Three Dimensional Flow Anisotropy and Transients on Turbulence Ingestion Noise in Open Rotors

Jarrod T. Banks

Dissertation submitted to the Faculty of the
Virginia Polytechnic Institute and State University
in partial fulfillment of the requirements for the degree of

Doctor of Philosophy
in
Aerospace Engineering

William J. Devenport, Chair
Nathan W. Alexander
Todd K. Lowe
Craig Woolsey
Jason Anderson

May 29th, 2024
Blacksburg, Virginia

Keywords: turbulence, three dimensional separation, rotor noise, turbulence ingestion noise, transient disturbances

The Impact of Three Dimensional Flow Anisotropy and Transients on Turbulence Ingestion Noise in Open Rotors

Jarrod T. Banks

(ABSTRACT)

The effect of flow anisotropy and three dimensional separation on the turbulent structure and radiated turbulence ingestion noise of a rotor in two experimental configurations is studied. The first consists of a non-axisymmetric boundary layer wake ingested by a rotor mounted at the aft of a body of revolution inclined at 5^o angle of attack. In the second configuration a transient disturbance is generated by an upstream wing body junction pitching from zero to 20^o angle of attack . This disturbance is convected downstream and ingested into a rotor immersed in a wall boundary layer. In both cases flow velocimetry at the rotor inflow is done and the far field sound is measured. The flow velocimetry in the wake of the inclined body of revolution shows evidence of three dimensional separation and vortex rollup between the lee and body sides. A boundary layer embedded shear layer develops as the turbulent kinetic energy is pulled off the wall by the flow separation and is visible in the port side velocimetry. The turbulent structure of this shear layer and the boundary layer on the lee of the body is visualized using compact eddy structure representation and the modes on the port side are shown to be stretched versions of similar modes seen in an equilibrium, zero pressure gradient boundary layer. The effect these structures had on the radiated sound served to both increase blade to blade correlation and the overall broadband levels of the sound. Measurements of the sound using an acoustic array showed directivity effects that resulted from the location of the embedded shear layer and rollup vortices. Although the vortices likely have some effect on the spectra, most of the noise is dominated by the turbulence ingestion

of the embedded shear layer.

For the second experimental configuration the transient motion was documented through repeated measurements of the flow field and sound, and an ensemble average of the measurements taken. Overall the flow was unsteady, particularly in the outer region of the boundary layer. The sound radiated was shown to be tonal during the first half of the interaction, where the flow is dominated by a deterministic mean flow change, and attributed to a form of periodic unsteady loading. During the latter half of the disturbance the broadband and overall sound levels increased significantly and are associated with the interaction of the rotor with flow separation over the wing body junction when it reached a critical, 16^o angle of attack.

The Impact of Three Dimensional Flow Anisotropy and Transients on Turbulence Ingestion Noise in Open Rotors

Jarrod T. Banks

(GENERAL AUDIENCE ABSTRACT)

The interaction of rotors and propellers with turbulence is commonly encountered when vehicles transit fluid mediums. In vehicles with aft mounted propellers, such as pusher type aircraft or underwater vehicles, turbulent boundary layers developed over the vehicle surface are ingested by the propeller. The size or scale of the average turbulent eddy greatly affects the type of sound generated by the interaction. For eddies that are small enough to only interact with one blade, the blade angle of attack varies randomly as it rotates through the turbulence and this radiates broadband sound. However, if the blade encounters eddies that are large or long enough to interact with multiple blades then the angle of attack, and thus the fluctuating lift force, begins to be correlated for each passage of the blade. This is known as blade to blade correlation and produces energy and sound concentration around the frequencies that correspond to the blade passage. This phenomenon is fairly well understood and many attempts have been made to model and predict the sound spectra from a rotor encountering turbulence in this manner. However these models often assume isotropic and homogenous turbulence when making predictions. This assumption works well in many applications, however, often the turbulence the rotor encounters is anisotropic with significant flow inhomogeneities. Thus, experimental investigations into the mechanisms and sources of sound in inhomogenous and anisotropic flows is necessary in an attempt to inform further flow and acoustic models.

In this dissertation the inflow and acoustic response of a rotor ingesting significantly complex and anisotropic flows is characterized. It focuses on two commonly encountered flow arrangements; a rotor mounted at the stern of a body of revolution at an angle of attack, and a rotor ingesting a turbulent wall boundary layer with transient disturbances introduced by an upstream wing body junction. In both cases the flow is three dimensional and the rotor encounters significant circumferential turbulence variation during its rotation through the resultant turbulent flow field. For the flow about the body of revolution the flow and noise appear to be driven by the rotor interaction with an embedded shear layer that results from three dimensional separation between the lee and windward sides of the body. For the transient disturbance interaction the rotor noise response shows two separate noise sources. During the first half of the disturbance the blade response is tonal and associated with a deterministic blade angle of attack change as the rotor interacts with the transient. In the latter half of the disturbance the rotor broadband noise is significantly increased due to flow separation over the wing body junction.

Dedication

For the cats that warmed my lap along the way, Basil and Annie

Acknowledgments

First and foremost I would like to thank my advisor Dr. William Devenport. His kindness, encouragement, and faith in me have helped so much along the way. To the remainder of my committee, Drs. Nathan Alexander, Todd Lowe, Craig Woolsey, and Jason Anderson, thank you for your guidance and input as part of this journey. To my undergraduate advisor Dr Michael Brooks thank you for encouraging me to pursue a post graduate degree. And to Mr Michael Marcolini, thanks for all your soapbox speeches.

Too often we get lost in the theory of it all and forget about the hands on aspects that make an experimental PhD. This would not have been possible if it wasn't for the pragmatic and grumpy team at the Stability Wind Tunnel and AoE machine shop. Thanks to Bill Oetjens for his work keeping us safe in the tunnel, and James Lambert and Cameron Hollandsworth for their input on designs, manufacturing, and various practicalities.

Special thanks goes to all my funding sources, to Drs. Yin Lu Young, Ki-Han Kim and John Muench under ONR grant N00014-20-1-2650 for sponsoring this project. And to the Virginia Space Grant Consortium and the SMART program for the financial support.

A huge thanks goes to Humza Butt, and Shishir Damani, my office mates, idea bouncers, and question askers. Being able to struggle through things we don't understand together has helped immensely. Additionally, I would not have got very far without the help of my fellow graduate researchers. In my formative years as a PhD student thanks to Drs. Chris Hickling, Agastya Balantrapu, Aldo Garguilo, Danny Fritsch, Vidya Vishwanathan, Aditya

Acharya, and Addison Collins for advice and friendship. In more recent years thanks to my project mates Szu-Fu Huang, Shaheen Palanganda, and Daji Chen. Also to Shreyas Chaware, Bhavika Sharma, Rachel Andrews, Advait Borole, Agata Grzyb, Monica Shanmugan, and many others in CREATe.

And most importantly to my wife, Merete. Your support and love during this time in my life has been immeasurable. To Brett, for beating me to a graduate degree, and to Mom, Dad, and Sharon for your love and support.

Contents

List of Figures

List of Tables

Abbreviations

APG	-	Adverse Pressure Gradient
BOR	-	Body of Revolution
BPF	-	Blade Passage Frequency
BVI/BWI	-	Blade Vortex/Wake Interaction
CES	-	Compact Eddy Structure
DG	-	Disturbance Generator
ESL	-	Embedded Shear Layer
J	-	advance ratio (U_∞/nD)
LES	-	Large Eddy Simulation
LSE	-	Linear Stochastic Estimation
NACA	-	National Advisory Committee for Aeronautics
NSWCCD	-	Naval Surface Warfare Center Carderock
PIV	-	Particle Image Velocimetry
POD	-	Proper Orthogonal Decomposition
RANS	-	Reynolds Averaged Navier Stokes
RDT	-	Rapid Distortion Theory
R_e	-	Reynolds Number
RPM	-	Revolutions Per Minute
SPL	-	Sound Power Level
TIN	-	Turbulence Ingestion Noise
TKE	-	Turbulent Kinetic Energy
UAV	-	Unmanned Aerial Vehicle
UND	-	University of Notre Dame
UUV	-	Unmanned Underwater Vehicle

VTOL/eVTOL	-	electric Vertical Take-off and Landing
VTSWT	-	Virginia Tech Stability Wind Tunnel
ZPG	-	Zero Pressure Gradient

Chapter 1

Introduction

Turbulent boundary layer flows are ubiquitous in vehicles transiting through a fluid medium. The interaction of turbulent boundary layers with vehicle surfaces, rotors, propulsors, and fans excite unsteady forces over the vehicle and blade surfaces. The unsteady forces radiate to the far field as sound with their spectral form and intensity dependent on the turbulence energy and surface response. In many practical configurations the boundary layers are under the effects of curvature and pressure gradients, for example boundary layers developed over the surface of a vehicle and then ingested into a rotor such as in many pusher, Vertical Take-Off and Landing (VTOL) rotorcraft, submarines, small Unmanned Aerial Vehicles (UAV's), and Unmanned Underwater Vehicles (UUV's). Typically these shear layers are also under the influence of some form of pressure gradient induced by the vehicle body surface.

1.1 Noise Generating Mechanisms in Rotor Systems

Noise radiation from rotors can be split into a few, distinct noise generating mechanisms. At low frequencies, below a couple of kHz in most low speed applications, broadband noise from the leading edge dominates the sound spectrum in the form of broadband spectral humps that are centred about the blade passage frequencies and its harmonics. This is referred to as turbulence ingestion noise (TIN). Trailing edge noise, also known as airfoil self-noise, is generated by the interaction of the turbulent flow over the trailing edge of the rotor, and

vortex shedding off the trailing edge. This noise typically occurs at higher frequencies than leading edge noise and is more dominant when the rotor is ingesting clean flow with low turbulence levels. Blade vortex interactions (BVI) are specific phenomena that occur when a rotor blade cuts the tip vortex of the preceding blade. Most often seen in helicopters in certain maneuvers (such as descending flight) this produces high instantaneous sound pressure levels in the far field at the blade passage frequency and can be heard as loud thumps. This can be analogous to an airfoil passing through a vortex or disturbance where the intensity and lengthscale of the disturbance will determine if the sound resembles a BVI or the more general broadband haystack. Circumferentially varying inhomogeneities in the flow field are often responsible for tone generation at the blade passage frequencies. The rotor interacts with the flow variation a certain number of times per rotation so the blade response is then amplified at the blade passage frequency. This dissertation will focus on the sub category of rotor noise referred to as turbulence ingestion noise and the following section will introduce its fundamentals.

1.2 Turbulence Ingestion Noise

The far field sound radiated by a rotor within a turbulent flow due to leading edge/turbulence ingestion noise is dependent on several fundamental variables. The most important being the thrust response of the rotor to an incoming eddy, the rotor blade passage frequency (related to the number of blades and advance ratio of the rotor) and the turbulent length scales within the flow. The spectrum of the sound radiated by a rotor is characterized by two broadband frequency shapes; broadband haystacking blue shifted from the blade passage frequency and broadband sound at all other frequencies. In order to understand the difference in the physical interpretation for these two it is useful to consider two different

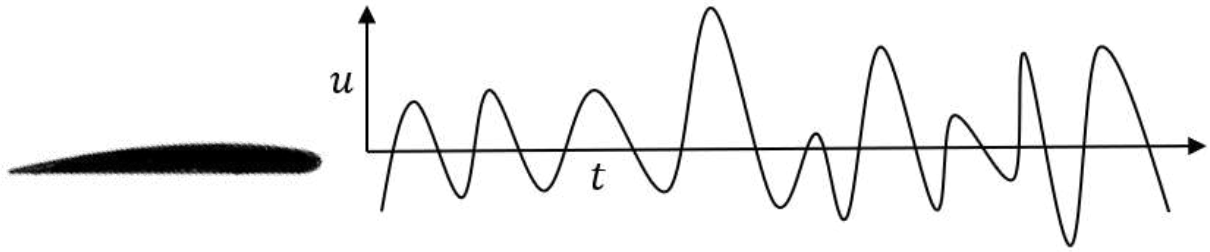

Figure 1.1: Turbulent velocity time signal seen by a rotor blade (pictured left) as it rotates through a turbulent velocity field. u represents the velocity fluctuations experienced by the blade through time, t.

frames of reference.

The first is that of a frame of reference rotating with the blade such that the blade is stationary and the turbulence is sampled as it rotates. This is shown in figure 1.1. For turbulent time scales smaller than the blade passage time, an eddy interaction with the blade produces a local induced angle of attack. The blade passing through many of these small eddies over the course of its rotation results in the blade experiencing a fluctuating lift force which radiates into the far field as broadband sound.

The second is a Lagrangian frame of reference that convects with an eddy with a time scale greater than the blade passage frequency. This is shown in two parts in figure 1.2. Figure 1.2a shows the blade cascade of the rotor from the perspective of a stationary observer viewing a wind tunnel experiment.

This is then put into the eddy frame of reference in figure 1.2b. In the figure U_∞ is the freestream velocity of the fluid, U_c is the convection speed of the eddy, and f_{BPF} is the frequency with which the blade cuts through the eddy. The sound spectrum is dependent on the correlation of the turbulence structures to the blade passage; that is to say, if the time between blade passages is greater than the turbulence scale the response of each successive blade is uncorrelated with that of the previous blade. However, if multiple blades pass

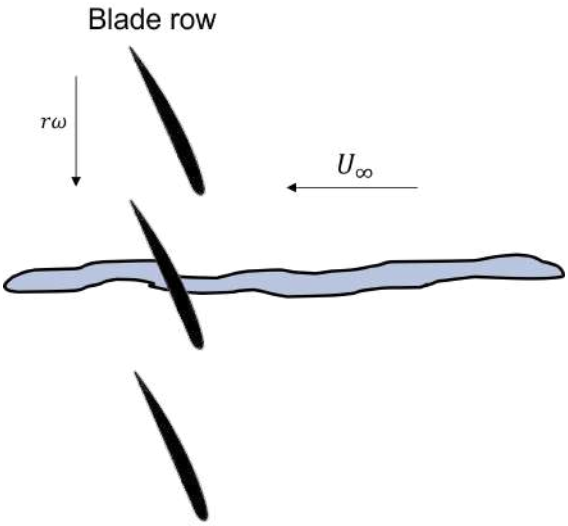

(a) Eulerian (laboratory) frame of reference.

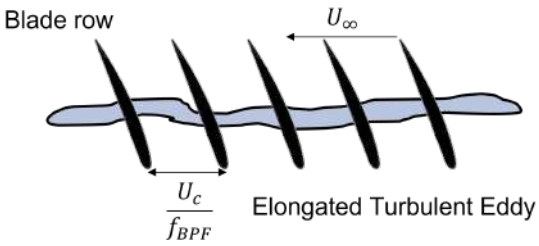

(b) Lagrangian (eddy) frame of reference.

Figure 1.2: Illustration of a blade row for the case where the eddy lengthscale is larger than the time it takes for one blade passage. a) shows an imagined instantaneous image of the eddy with the blade row shown in a laborotory (Eulerian) frame of reference and b) shows the passage of the blade through the eddy multiple times from the frame of reference of the eddy (Lagrangian).

through the same turbulent eddy (time between blade passages is significantly smaller than the turbulence scale), then the thrust responses of some of the blades are correlated with each other and the radiated spectral content is concentrated about the blade passage frequency. This produces the haystacking evident in Sevik [79], Balantrapu et al. [48], Murray et al. [72] amongst many others. This correlation between successive blades is well illustrated in figure 1.3 of LES data from Zhou et al. [92]. They performed LES calculations on a turbulent boundary layer as it grows over an axisymmetric body of revolution and is eventually ingested into a rotor at the aft end of a ramp. The contours are levels of velocity correlation between specific data points that vary in time on the horizontal axis, and in radial distance from the rotor hub on the vertical axis. These show turbulent correlations that have peaks at intervals of the blade passage period, the coherence of the turbulence shown here demonstrate a rotors ability to influence the turbulence it ingests. Further evidence of the impact a thrusting rotor

has on the inflow turbulence to a rotating fan was discussed in Majumdar and Peake [64] and the stretching of the turbulence and its effect on flow lengthscales and subsequently the far field radiated noise was discussed. They modeled and measured the ingestion of atmospheric turbulence in a static engine test. For static conditions the turbulence within the streamtube was strongly distorted due to the quiescent air surrounding the fan, allowing the fan thrust to more strongly distort the turbulence as it is ingested. However for inflight conditions the turbulence distortion is significantly weaker and the spectral humps were less prominent in the acoustic spectra. A similar study was conducted by Hanson [43] for a rotor in static conditions and significant stretching of the streamwise eddies was found; up to a lengthscale ratio of 400:1 between the streamwise and transverse directions. These resulted in exaggerated spectral humps within the acoustic spectra. So much so that they could very easily be confused with pure tones. He further suggested that some experiments incorrectly attributed tone generation to fixed flow distortions when they were, in fact, due to highly coherent streamwise structures ingested into the fan.

One of the seminal bodies of research into turbulence ingestion noise in rotors is the work done by Sevik in 1971 [79]. He developed a model using a correlation method and assuming isotropic inflow turbulence. To verify the model predictions he measured the unsteady force spectrum on a 10-bladed, 4 inch rotor subjected to grid generated turbulence. He was among the first to observe the haystacking phenomenon but attributed it to blade resonances rather than a blade response to the turbulence. In the modelling he assumed, due to the high advance ratio, that all blades are rotationally uncorrelated and each blade can be regarded as responding individually to the ingested turbulence. Thus the spectral response is strictly broadband. His experimental results belied that assumption and are illustrated in figure 1.4.

Chapter 2 will first review the literature available on experimental work into turbulence in-

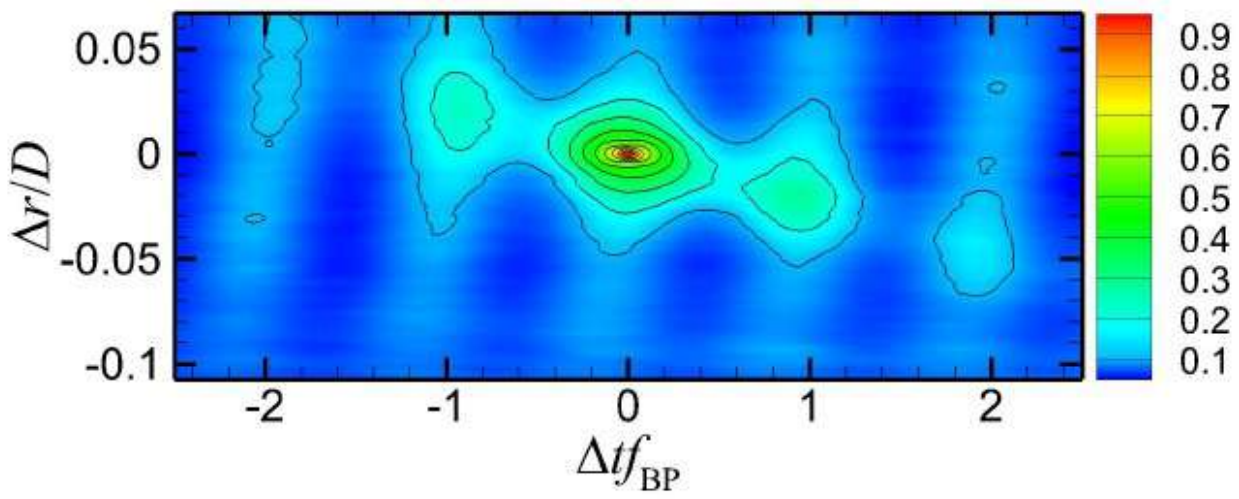

Figure 1.3: Radial space-time correlations at the inlet of a rotor operating in a turbulent boundary layer. The contours show the correlation between streamwise velocities. The vertical axis is a plane extending from the anchor point radially, and the horizontal axis is the time separation of the velocity time series. Figure courtesy of Zhou et al. [92].

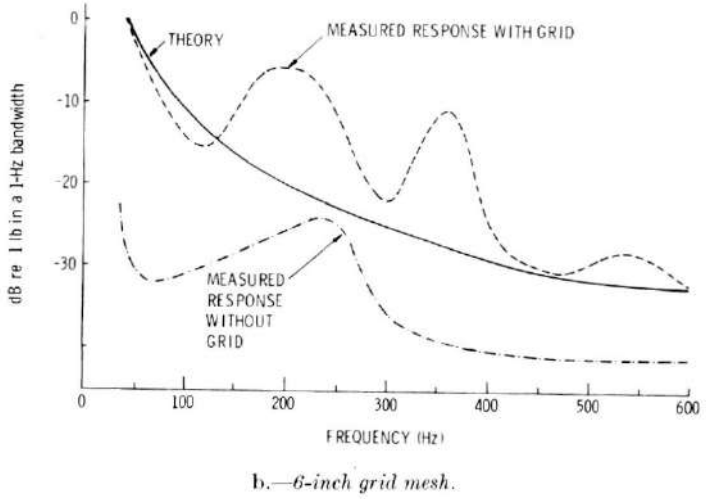

b.—*6-inch grid mesh.*

Figure 1.4: Measured fluctuating thrust by Sevik [79] in clean flow (dash-dot) and with grid generated turbulence (dotted) compared to his developed model (solid).

gestion noise. It will then cover the development of isotropic models for turbulence ingestion noise, go on to discuss the little available work that covers transient disturbance ingestion in rotor systems before providing the background of TIN research. Finally, a review of flow about bodies of revolution inclined at various angles of attack is done and conclusions regarding the literature are presented.

Chapter 2

Review of Literature

2.1 Isotropic Models and Grid Turbulence Ingestion

A significant body of work on various parts of the turbulence ingestion noise puzzle was worked on over a period of two decades at the University of Notre Dame and includes works from researchers such as Scharpf, Minniti, Martinez, Lynch, Wojno, Mueller, and Blake. Much of the work involves the use of isotropic turbulence models and comparisons of these results to rotors ingesting grid generated turbulence.

Blake's [20] model superimposes the sound spectrum of large wavenumber (small scales) and small wavenumber (large scales) to obtain an overall sound spectrum. The large wavenumber acoustic spectrum produces the more broadband response, while the small wavenumber acoustic spectrum produces the haystacks typical of turbulence ingestion noise. The upwash component of the blade inflow velocity is denoted u_2 in the propeller coordinates (with x_1, x_3 being the transverse directions in the propeller plane). This fluctuating velocity is written in wavenumber frequency space by applying a Fourier transform to the fluctuating velocity as follows,

$$u_2(\overline{k},\omega) = \frac{1}{(2\pi)^3}\int\int\int\int u_2(\overline{x},t)e^{-i(\overline{k}.\overline{x}-\omega t)}d\overline{x}dt \tag{2.1}$$

The lift per unit radius in the frequency domain can be given by the following equation,

$$dL_s(\omega)/dr = \rho\pi u_2(\overline{k},\omega)U(r)S_{2D}(k_1C/2)e^{i(k_3r+k_{12}sb-\omega t)} \tag{2.2}$$

where $u_2(\overline{k}\omega)$ is the spectrum of the upwash velocity given in Equation 2.1, C is the chord length of the blade, $U(r)$ is the net inflow velocity to the rotor blade in a frame of reference fixed on the blade at that radius, S_{2D} is the 2 dimensional Sears function which the describes the response of the blade lift to an incident gust, and b is the blade spacing.

This equation gives the unsteady lift per unit radius and from there the unsteady force is determined by summing the unsteady lift over all blades and integrating over the blade radius from the hub to the tip in the following manner,

$$F_i(\overline{k},\omega) = \int_{R_H}^{R_T} \rho\pi C u_2(\overline{k},\omega)U(r)n_i(\phi)S_{2D}(k_1C/2)A_s(k_{12}b)e^{-i(k_3r-\omega t)}dr \tag{2.3}$$

In this equation $n_i(\phi)$ is the direction cosine in the ith blade direction and the term A_s is referred to as a filtering function and is the summation over the blades, N, defined in the following manner,

$$\begin{aligned} A_s(k_{12}b) &= \sum_{s=0}^{N-1} e^{ik_{12}sb} \\ &= \frac{\sin(Nk_{12}b/2)e^{i(N-1)k_{12}b/2}}{\sin(k_{12}b/2)} \end{aligned} \tag{2.4}$$

This function serves as a spatial filter over rotational wave numbers for each blade and demonstrates how the blades sample the incoming turbulence. The wavenumber directions are defined in the same manner as the coordinate system (x_1, x_2, x_3) described in the previous paragraphs with k_1 downstream, k_2 normal to the blade, and k_3 aligned with the rotor

disc. The frequency spectrum of the fluctuating force is then found by integrating the force autocorrelation over all wavenumbers. This equation is given here as,

$$\Psi_{ii}(\omega) = \int_{k_1}\int_{k_2}\int_{k_3}\int_{R_H}^{R_T}\int_{R_H}^{R_T} \rho^2\pi^2 C^2 |Se_{2D}(k_1 C/2)|^2 |A_s(k_{12}b)|^2 U(r_1)U(r_2) \Phi_{22}(\overline{k},\omega) n_i(\gamma_1) n_i(\gamma_2) e^{ik_3(r_2-r_1)} dr_2 dr_1 d\overline{k} \tag{2.5}$$

Thus far each variable in this equation has been defined for Equations 2.1 to 2.4. This frequency spectrum depends on a turbulence force spectrum $\Phi_{22}(\overline{k},\omega)$ which is assumed to be wavenumber separable and written in terms of the wavenumber spectrum in each principal direction. Blake then writes the wavenumber spectrum, $\phi_i(k_i)$,inspired by the Leipmann [58] spectrum, as,

$$\phi_i(k_i) = \frac{1}{\pi}\frac{\Lambda_i}{1+(\Lambda_i k_i)^2} \tag{2.6}$$

where Λ_i is the length scale of the flow. The full derivation of the turbulence force spectrum will not be shown here but can be found in Chapter 6 of Blake [20]. For values of Λ_i smaller than U_c/f_{BPF}, (ie. when all blades are uncorrelated with each other) the turbulence force spectrum simplifies to,

$$\Phi_{ii}(\omega) = \frac{8\pi^2}{3n_s}(\frac{1}{2}\rho V^2)^2 R_T^4 (\frac{C}{R_T})^2 (\frac{\pi}{J})^2 \frac{\overline{u}_2^2}{V^2}\frac{2\Lambda_3}{R_T}\frac{\Lambda_1/\pi R_T}{1+(\Lambda_1\omega_s/\Omega_s R_T)^2}\frac{1}{1+\pi\omega C/\Omega_s R_T} \tag{2.7}$$

And for values of Λ_i greater than U_c/f_{BPF}, (ie. when multiple blades cut the same turbulent structure and the response is coherent) the turbulence spectrum then becomes,

$$\Phi_{ii}(\omega) = \frac{8N\pi^2}{3n_s}(\frac{1}{2}\rho V^2)^2 R_T^4 (\frac{C}{R_T})^2 (\frac{\pi}{J})^2 \frac{\overline{u}_2^2}{V^2}\frac{2\Lambda_3}{R_T}\frac{\Lambda_1/\pi R_T}{1+(\Lambda_1 mN/R_T)^2}\frac{|A_s[(k_2\sin(\gamma)+\frac{\omega}{U_t}\cos(\gamma)b]|^2}{1+\pi mNC/R_T} \tag{2.8}$$

Equation 2.7 replicates the broadband spectrum similar to that modelled by Sevik. It is a result of the fluctuating force induced by the varying angle of attack of each individual blade as it rotates through the turbulent field. Equation 2.8 shows the haystacking seen when successive blades are correlated with each other. The disadvantage to this model is that the large and small lengthscales have to be treated seperately. Jiang et al. [52] were able to condense the modelling of the spectrum response by predicting the broadband and blade passage haystacks simultaneously for an isotropic, homogenous turbulence field. They approached the modelling of unsteady propeller forces due to turbulence using the correlation approach used by Sevik [79] rather than the spectral approach just described in Blake [20]. However, the major difference between the Jiang model and Sevik model is that Jiang's model accounts for the rotor rotation and therefore captures the haystacking in the predicted force spectrum.

The isotropy and homogeneity of grid generated turbulence is well studied experimentally. Roach [75] studied grid turbulence parametrically and presented evidence that grid generated turbulence is isotropic in nature based on the relationship between the microscales λ_z, and λ_y. He also showed that the turbulence energy is dependent on the rod dimensions rather than mesh size or solidity. The assumption of isotropic and homogenous turbulence greatly simplifies the characteristics of the flow so it is often used in experimental measurements and in the development of analytical predictions. This assumption allows the velocity correlation between two points to be written as a scalar multiple of the longitudinal and transverse autocorrelation functions.

Scharpf and Mueller [77] sought to understand the structure of the turbulence in the wake of a rotor in order to develop insight into the noise radiated by a rotor in low speed turbulence. They took hotwire measurements of the wake of a 4-bladed, 10 in. diameter rotor extending from the hub to beyond the rotor disc to quantify the wake turbulence as a function of

rotor radius. Microphone measurements were taken in an arc from 50°to 130°as well as from 230°to 310°(where 0°corresponds to the rotor inflow and angles are positive anti-clockwise) to obtain acoustic spectra and document the rotor directivity. The experimental setup is shown in figure 2.1.

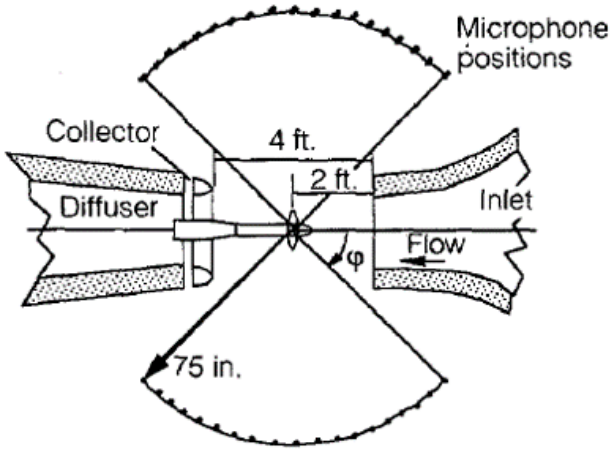

Figure 2.1: Experimental setup for the experiments at UND courtesy of [77].

The lengthscales of the turbulence in this experiment were small so there was little blade to blade correlation and the spectra reflected this by being exclusively broadband. They subjected the rotor to both clean flow and grid generated turbulent flow and examined the resultant autobicoherence. The autobicoherence for the clean flow showed high values at the blade passage frequency and harmonics near the hub and tip indicating strong phase-coherence on the passage of the blades. Comparatively the turbulent inflow showed significantly lower bicoherence at all measured positions (from hub to tip). This is indicative that the energetic turbulent flow overcame any phase locked behaviour from the blade passage and the sound radiating from this inflow is mostly broadband and independent of the rotor blade passage harmonics.

It is well understood in the study of turbulence ingestion noise that the haystacks appearing centered on the blade passage frequency are, in fact, right shifted (blue shifted, or shifted

to higher frequencies) some 5-10%. Martinez [66] undertook research into the analytical mechanism of this frequency shift using the modelling developed in Martinez [65]. He stated that the analytical mechanism for this frequency shift is as a result of the rotor acting as a three dimensional flow sampler on the turbulent flows' probabilistic character. Omitting either the sampling of the fluid by the rotor, or the probabilistic nature of the turbulence would result in a spectral shape with no frequency shifts for the haystacks. He proposed equations that, when applied to a turbulent flow and rotor with specific flow length scales, blade numbers, and advance ratio predicted the right shift to some degree of accuracy even in inhomogenous flows. He concluded that the right-shift rises with the square of the advance ratio and can be attributed to the increasing tip velocity forcing greater turbulent flow sampling of eddies parallel to its rotational plane.

Lynch et al. ([61], [62], [63], [60]) conducted extended investigation into the nature of the correlation length scales and predictions of the far field sound radiated based on both the classic integral length scale and the correlation length scale. Starting with [61] and [62] Lynch et al. sought to investigate the aeroacoustic response of a rotor/stator pair. The experiment was performed in the Anechoic Wind Tunnel at the Hessert Center for Aerodynamic Research at UND which is an open jet anechoic tunnel. The setup is shown in figure 2.2 below and consisted of a rotor ingesting grid generated turbulence with an airfoil just downstream of the rotor to simulate the stator.

The focus was on the wake contribution to the downstream turbulence. X-wire hotwire anemometry measurements were taken 3 inches downstream of the rotor trailing edge to examine the turbulence statistics. Based on the clearly defined wake influence they suggested that the sound from the stator could be modelled using superposition of the turbulence ingestion and the wake effects. They were able to show that the integral length scales and correlation length scales within the wake are on the order of the wake thickness as well as the

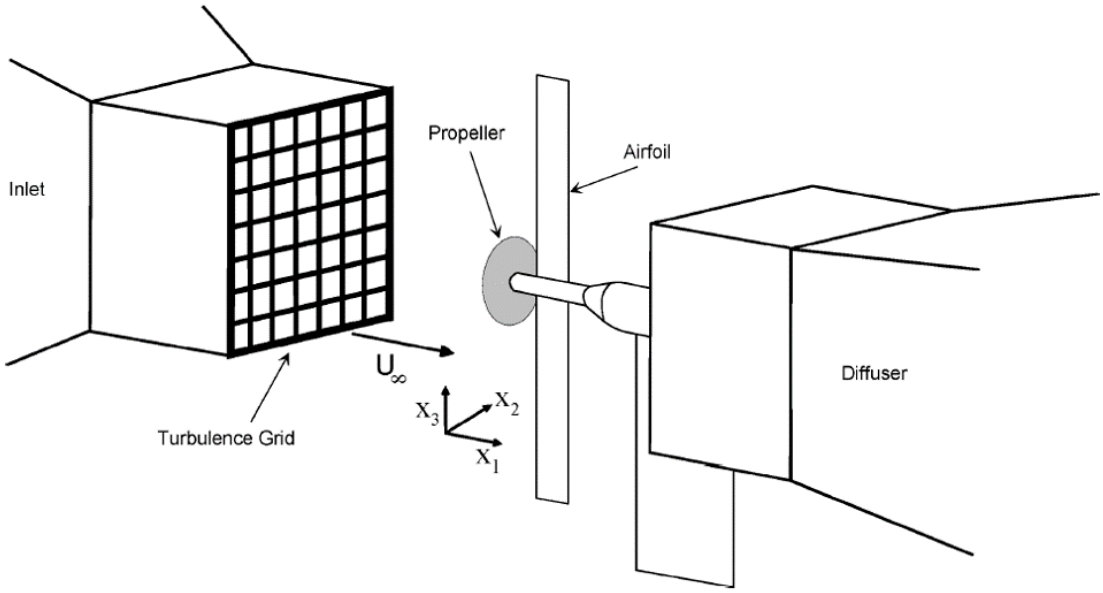

Figure 2.2: Experimental setup used by Lynch et al ([61], [62], [63], [60]) in their investigation into rotor/stator pair noise.

velocity profile half-width. In the follow up paper [62] they examine the modification of the broadband component of the downstream turbulence. Modification of turbulence passing through a rotor is fairly well addressed using rapid distortion theory (RDT) as presented by Batchelor and Proudman [18] for isotropic turbulence and Sreenivasan and Narasimha [82] for anisotropic turbulence. Graham [42] extended RDT to account for a two dimensional cascade of thin plates, with the intention of application to rotor turbulent distortion. The cascade represents the blade passage in a rotating frame of reference. Results from this paper (Lynch et al. [61], [62]) show no acoustics, but instead try to show how the broadband turbulence in the rotor wake (ie. the pieces of the flow not associated with the blade passage) is modified, they examine how well the RDT method of Graham predicts the mean velocity deficit subtracted turbulence spectrum. Overall Graham's RDT model predicts the modified turbulence spectrum well.

More recently work focused on inhomogenous, anisotropic shear flows was undertaken at

NSWCCD (Naval Surface Warfare Center, Carderock) by Catlett et al. [24] and revealed the inaccuracies associated with the application of homogenous, isotropic turbulence assumptions to anisotropic shear flows.

Figure 2.3: Image showing the experimental setup used in the AFF for the NSWCCD Carderock experiment courtesy Catlett et al. [24]

Catlett et al. [24] examined the acoustic response off a 7-bladed rotor to the ingestion of a highly turbulent and anisotropic flow field induced by a full span airfoil just upstream of the rotor. The airfoil produced a turbulent boundary layer that fully engulfed the rotor. They then made comparisons using the measured acoustic spectra, modelling using a homogenous, isotropic turbulence assumption, and modelling using a correlation function determined empirically through hotwire anemometry measurements, which would account for anisotropy and spatial variation of the upwash velocity space-time correlations. An image of the experimental setup is given in figure 2.3. As evidenced in Figure 2.4 the isotropic assumption (red curve) greatly underestimates the measured acoustic response. However, including the

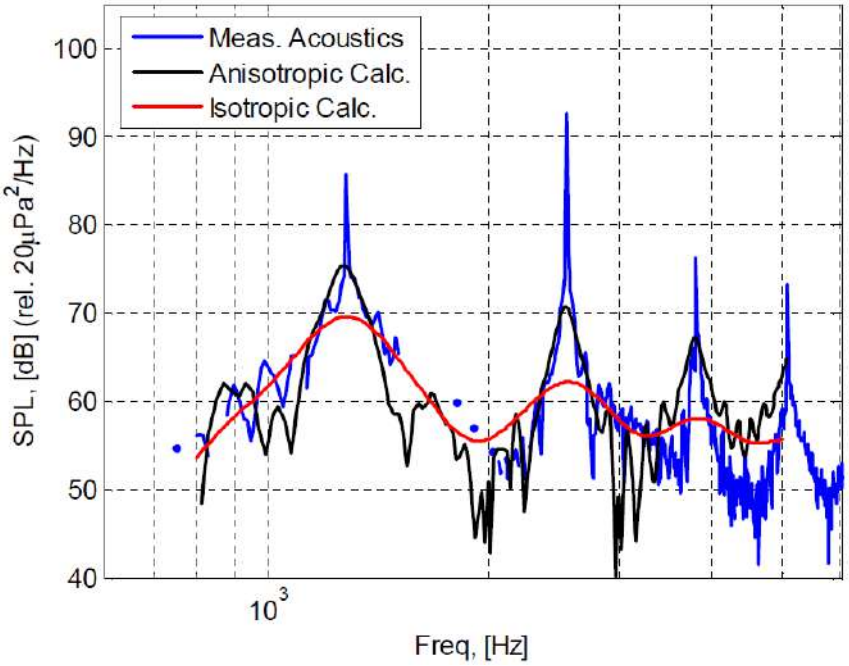

Figure 2.4: Rotor noise predictions done by Catlett et al. [24] showing a comparison of measured acoustics (blue curve), modelling using an anisotropic correlation function (black curve), and modelling using an isotropic correlation function (red curve).

modifications made in the modelling, which captured the anisotropy and spatial variations of the upwash velocity correlations, Catlett et al. brings the narrowband haystacking closer to that seen in the measured acoustics. Additionally seen in the measured noise spectra is the existence of tones at the blade passage frequency that arise from the mean flow deficit introduced by the airfoil wake. A turbulence velocity correlation approach cannot account for these tones as they exist in the mean and thus the modelled spectra does not reflect them.

2.2 An Overview of Turbulence Ingestion Noise Research

The experimental study of turbulence ingestion noise has been expanded considerably in the past two decades by researchers at Virginia Tech and Florida Atlantic University, among others. This paragraph summarizes the sequence of studies while the following paragraphs explore more details on the specifics and experimental findings. Most of these studies were conducted on a modified Sevik rotor ingesting either a turbulent boundary layer or a cylinder wake. The turbulent boundary layer was developed over a flat wall as well as a body of revolution. Morton et al. [68] measured the 4 point (x,y,z,t) space-time correlation function of a zero pressure gradient, equilibrium boundary layer. This was then used by Alexander et al. [5], [3] and Glegg et al. [39] in the development and testing of an analytical, time domain, correlation based, turbulence ingestion noise model. The models effectiveness at predicting tones from a BVI like flow interaction was discussed in Glegg et al. [36] and Murray et al. [72]. Alexander et al. [6] and Molinaro et al. [67] presented results of the Sevik rotor ingesting a cylinder wake which was extended further by Hickling [47]. More recently Balantrapu [14], [15] investigated the ingestion of an axisymmetric and significantly inhomogenous boundary layer subjected to a strong adverse pressure gradient by a modified Boswell rotor. The following paragraphs discuss the experimental specifics and relevant results of each study.

Some of the first forays into turbulence ingestion noise research at Virginia Tech were undertaken by Morton et al. [68]. They investigated the turbulence structure of an equilibrium boundary layer developed along a wall in the Virginia Tech Stability Wind Tunnel. This tunnel is a closed circuit wind tunnel with a 6ft by 6ft test section. The boundary layer was two dimensional, zero pressure gradient and measured at $Re_\theta = 16,607$ and $Re_\delta = 194,306$.

They characterized the turbulence using 3-component hot wire measurements in a cross-sectional plane. The coordinate system used was right handed with x positive downstream, z normal to the wall, and y spanwise completing the right handed system. The detailed measurements of the correlation structure revealed significant anisotropy in the turbulence and a slice of the space-time correlation function is shown in figure 2.5. The correlation

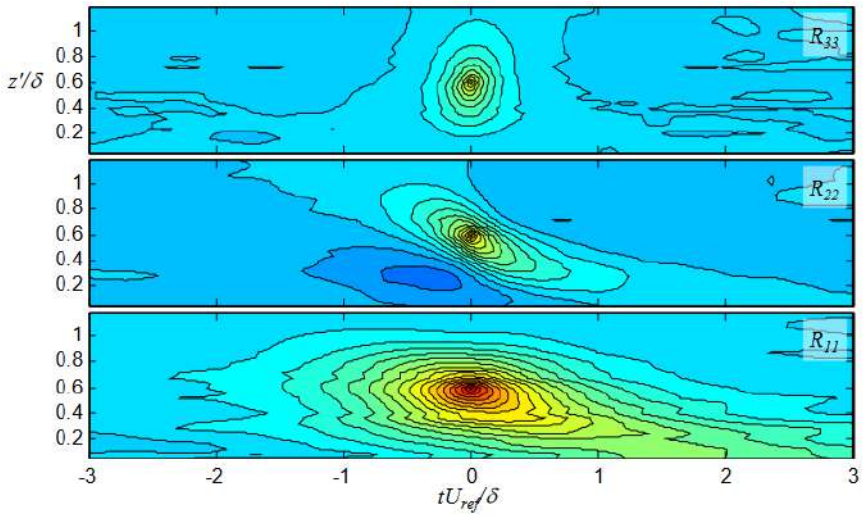

Figure 2.5: Cut through the four dimensional two-point cross correlation function for the 3 normal components, normalized on free stream velocity and boundary layer thickness, $R_{ij}(0.6\delta, z', 0, t)$ in a wall bounded turbulent boundary layer measured in [68].

structure showed stretching in the streamwise direction and was inclined to the wall at 30^o yielding asymmetry in the blade to blade upwash correlation.

This 4-dimensional (x,y,z,t) space-time correlation structure was used by Morton as an input to a noise prediction code based on Glegg et al. [35] that attempted to predict the broadband signature of the radiated noise by a 10-bladed Sevik rotor ingesting a turbulent boundary layer. These predictions were based on the idealization of a Sevik rotor on the wall of the test section with the blades immersed in the wall boundary layer. Predictions of the sound radiation were presented, however, the predictions were not compared to any experimental measurements of the radiated noise. The noise prediction model used in this paper is based

on an unsteady loading theory for inhomogenous turbulence developed by Glegg and gives the far field noise spectrum at an observer location $\overline{x}$ and angular frequency ω as shown below,

$$S_{pp}(\overline{x},\omega) = (\frac{\omega}{c_0 r_0})^2 \sum_{n=1}^{B}\sum_{k=1}^{B}\sum_{m=-\infty}^{B}\int_{R_{hub}}^{R_{tip}}\int_{R_{hub}}^{R_{tip}} K_m(R,\overline{x},\omega)K_m^*(R',\overline{x},\omega)S_{LL}^{(n,k)}(R,R',\omega-m\Omega) \\ e^{-im(\phi_n-\phi_k)}dRdR' \tag{2.9}$$

where ω is the angular frequency, c_0 is the speed of sound, r_0 is the distance to the observer, and K_m and K_m^* are Fourier coefficients used to determine the propagation of sound from the rotor to the observer and account for the retarded time in the blade rotation. $S_{LL}^{(n,k)}$ is the unsteady lift spectrum between blades n and k, and can be written in terms of the upwash correlation function, $S_{ww}^{(n,k)}$,

$$S_{LL}^{(n,k)}(\omega,R,R') = [\pi\rho_o cUS(\sigma)]_R[\pi\rho_o cUS(\sigma)]_{R'}^* S_{ww}^{(n,k)} \tag{2.10}$$

Here, U is the appropriate velocity and $S(\sigma)$ is the two dimensional Sears function. The upwash correlation function can be found using the two point space-time correlation function measured by the hotwire measurements mentioned previously. The equation for this is given here,

$$S_{ww}^{(n,k)}(\omega,R,R') = \frac{1}{4\pi^2}\frac{\pi}{T}\int_{-T}^{T}\int_{-T}^{T} n_i^{(n)}(R,\tau)n_j^{(k)}(R',\tau')R_{ij}(\overline{z}_n(\tau),\overline{z}_k(\tau'),\tau-\tau')e^{i\omega(\tau-\tau')}d\tau d\tau' \tag{2.11}$$

Here $n_i(R, \tau)$ is the vector normal to the blade chord that specifies the lift force component and R_{ij} is the correlation function of the turbulence in the blade rotating frame of reference. Now, moving backwards through these equations using the measured two point space-time correlation function the far field noise spectrum at a specific observer location and angular frequency can be semi-analytically determined. This time-domain approach was done for the 10-bladed Sevik rotor ingesting a planar wall boundary layer. An experimental campaign in the Virginia Tech Stability Wind Tunnel was done and acoustic measurements were taken. The experimental setup for [3], [4], [71], [86], [36], and [5] is shown in Figure 2.6. The prediction results using the previously described semi-analytical method were compared to the measured acoustic spectra in Figure 2.7. The predictions showed the broadband nature

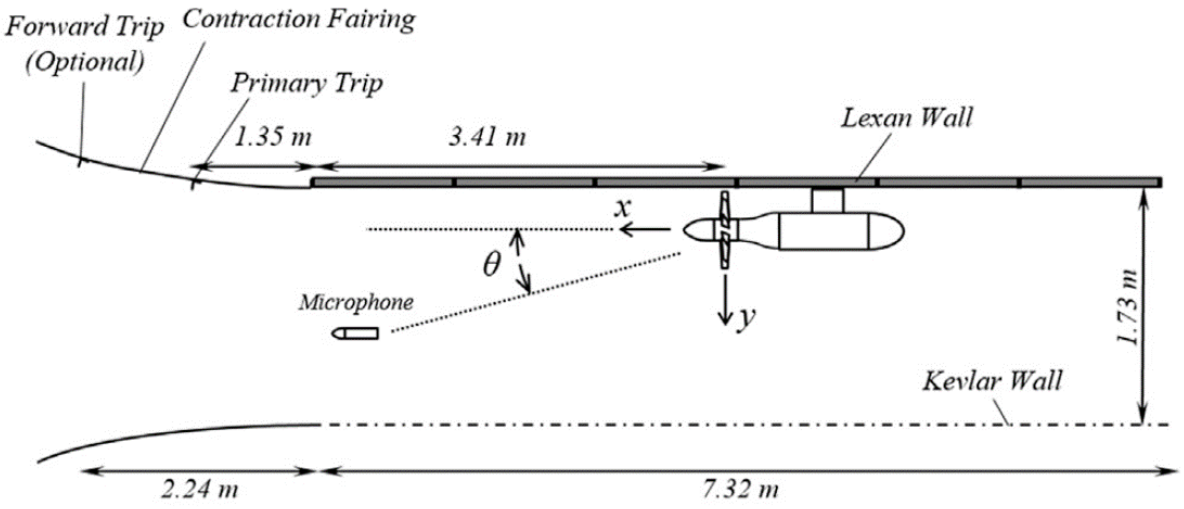

Figure 2.6: Experimental setup at the Virginia Tech Stability Wind Tunnel for the Sevik test results shown in [5], [3].

of turbulence ingestion noise with spectral humps at the blade passage frequencies. The natural extension of this work is to experimentally measure the resultant far field noise. Alexander et al [3] did precisely this and compared the measured spectra to those predicted in Morton et al. [68]. The predicted sound spectra is shown in figure 2.7 and matches that

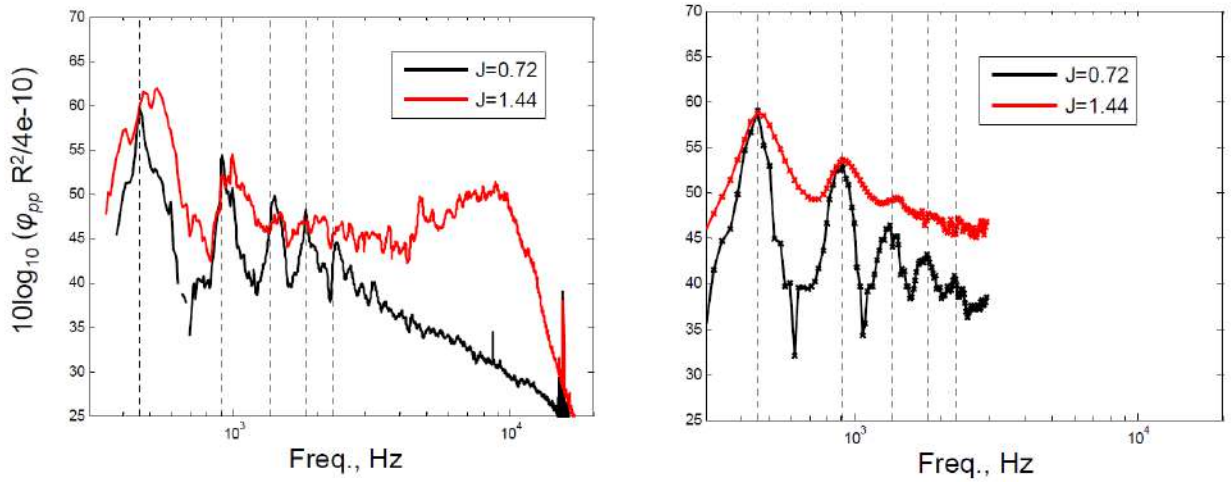

Figure 2.7: a) Measured sound spectra for the Sevik rotor at $J = 0.72$ and $J = 1.44$, b) predicted sound spectra from the 4-dimensional correlation function for $J = 0.72$ and $J = 1.44$. $U_\infty = 30m/s$ for $J = 1.44$ and $U_\infty = 15m/s$ for $J = 0.72$, 2734 RPM at a directivity angle of $\theta = 15°$. Results courtesy of Alexander et al. [3]

of the experimentally measured spectra quite closely. They found that the haystacks seen at BPF multiples increase in SPL and narrow in spectral shape with a decrease in J. As will be discussed further, this is a universally true phenomena which can be explained by the decrease in blade passage time, and thus an increase in blade to blade correlations when cutting through turbulent structures. He further developed a method for determining the turbulence characteristics (namely lateral scale and time-frequency distribution) from the averaged sound spectra, he found that the lateral scale remains unchanged with advance ratio but the turbulence time scale drops with decreasing advance ratio.

Glegg et al. [39] then extended the above time-domain approach with a similar, but slightly different, formulation. In this formulation the overall noise spectrum is given as,

$$S_{pp}(\overline{x},\overline{\omega}) = \frac{1}{4\pi T}\sum_{n=1}^{B}\sum_{M=1}^{B}\int_{R_{min}}^{R_{max}}\int_{R_{min}}^{R_{max}}\int_{-T}^{T}\int_{-T}^{T}\{arg\}\,dRdR'd\tau d\tau' \tag{2.12}$$

Where the argument $\{arg\}$ is given below

$$\left\{\frac{\partial}{\partial x_i}\frac{n_i^{(n)}(R,\tau)e^{i\omega r^{(n)}(\tau)/c_o}}{4\pi r^{(n)}(\tau)}\right\}\left\{\frac{\partial}{\partial x_j}\frac{n_j^{(m)}(R',\tau')e^{-i\omega r^{(m)}(\tau')/c_o}}{4\pi r^{(m)}(\tau')}\right\}R_{FF}^{(n,m)}(R,R',\tau,\tau') \tag{2.13}$$

R_{FF} is the unsteady loading correlation function which can be found from the correlation function of the upwash velocity in the following manner,

$$R_{FF}^{(n,m)} = \int_{-\infty}^{\tau}\int_{-\infty}^{\tau} s(R,\tau-\tau_o)s(R',\tau'-\tau_o)R_{ww}^{(n,m)}(R,R',\tau_o,\tau_o')d\tau_o d\tau_o' \tag{2.14}$$

Where $s()$ is the Kussner function and $R_{ww}^{(n,m)}$ is the correlation function of the upwash velocity. Finally the upwash velocity can be determined from the measured two point space-time correlation function of the inflow turbulence.

$$R_{ww}^{(n,m)}(R,R',\tau_o,\tau_o') = n_i^{(0)}(R,\tau_m)n_j^{(0)}(R',\tau_m'-s\Delta\tau)R_{ij}(y^{(0)}(\tau_m,R),y^{(0)}(\tau_m'-s\Delta\tau,R'),\tau_m-\tau_m') \tag{2.15}$$

From this the far field sound spectrum can be computed knowing just the rotor geometry and the inflow turbulence correlation function.

Alexander et al. [4] repeated the experiment in [3] but modified one of the Sevik rotor blades to include a hotwire on 2 consecutive blades at 80%, 90%, 95%, and 98.5% for the leading blade and at 90% and 98.5% on the trailing blade [4]. These hotwires were used to measure the ingested turbulence in a rotating frame of reference. Observations of the coherence between consecutive blade tips show features similar to haystacking at multiples of the BPF. The hotwire measurements further show that the turbulence distortion does not undergo a lateral contraction, agreeing with the previous conclusions from [3]. Below

an advance ratio of 0.79 a flow reversal phenomenon was identified. This flow reversal is thought to be the same phenomena identified by Huse et al. [49] as a propeller hull vortex generated by a rotor operating at high thrust near a ship hull. The propeller hull vortex is a form of cavitation identified by Huse et al. [49] at certain thrusting conditions of a marine propeller tested in the Norwegian Ship Model Experiment Tank. It consists of vortices with cavitating cores extending from the propeller to the hull above and ahead of it.

Predictions for the radiated noise using both rapid distortion theory in [3] and Glegg's time-domain approach (detailed in [39]) were performed. Both break down below this advance ratio as turbulence ingestions' influence on the radiated sound diminishes in favour of the highly coherent propeller hull vortex. Murray et al. [86] built on the foundation set by Morton and Alexander and examined the same rotor seen in figure 2.6 with a focus on the dependence of the radiated sound on rotor yaw angle. He noted in [71] that there is significant asymmetry in the rotor inflow when the rotor disk is yawed as well as there being significant effects on the radiated sound at different yaw angles. The trailing edge noise was more prominent in the case where the rotor was yawed. Murray measured the flow field in the tip gap using PIV for two advance ratios and identified the existence of 2 contra-rotating arch vortices for very low advance ratios [86]. Instantaneous images seen in figure 2.8 show that, even though the flow reversal is unsteady, the arch vortices are almost always present. The existence of these arch vortices are due to the highly thrusting rotor pulling fluid off the wall.

The flow reversal from the Sevik rotor operating near a wall at high thrust was expanded on in a Glegg et al. paper [36] and the physical mechanism of this phenomena is shown to be a form of blade vortex interaction. This noise source is similar to that generated by helicopter rotors when a blade cuts the vortex generated by the blade preceding it. This produces a highly coherent blade vortex interaction and is a tonal mechanism seen at the

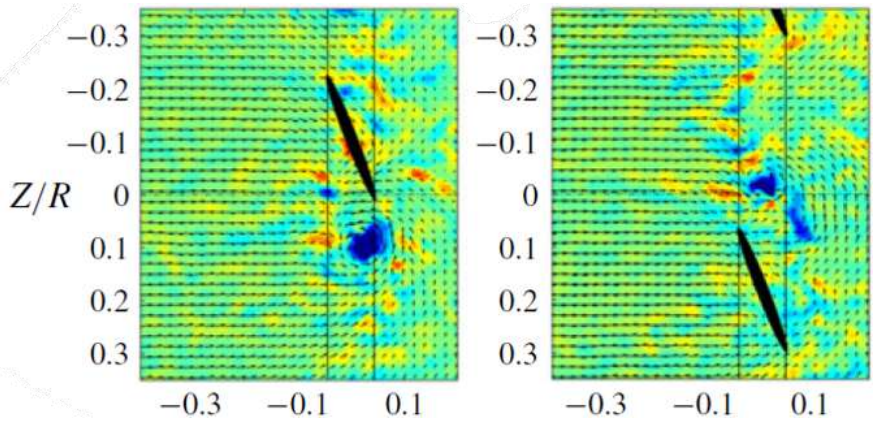

Figure 2.8: Instantaneous images of the particle image velocimetry results showing the structure most often seen in the measurements, "a single strong counterclockwise vortex" [72].

blade passage frequency as well as its harmonics. A prediction method using Howe's theory of vortex sound was developed and shown to predict the noise at low advance ratios well.

Alexander et al. [5] examined the effect of boundary layer thickness δ and thrust on the noise radiated using the same configuration as [3]. For the highest thrusting case examined there is little to no difference in the spectra produced between the two boundary layer thicknesses; this is once again attributable to the dominant source of noise for this case being a blade vortex interaction induced by local flow separation beneath the rotor tips. However, at the zero thrust condition (J=1.44) we see the thicker boundary layers corresponding to higher overall sound power levels. This can be explained by noting that the thicker boundary layer is associated with larger turbulence scales (both in general and shown by the rotating frame turbulence measurements).

Alexander et al [6] and Molinaro et al. [67] investigated the interaction of the Sevik rotor and a cylinder wake (experimental schematic shown in figure 2.9). The rotor was mounted in the center of the VTSWT test section and the cylinder placed 1.016 m upstream of the rotor disc at varying spanwise locations. They found that the rotor drew the streamtube of the cylinder wake towards the rotor hub. This meant that for a centered wake strike

the streamlines contracted due to thrust; and for an asymmetric wake strike the wake was drawn towards the hub. Boundary layer turbulence ingestion and cylinder wake turbulence ingestion were compared and it was found that the turbulence ingested by the boundary layer had a lower overall sound power level but more defined haystacking at moderate thrust when compared to the cylinder wake ingestion case. Boundary layer eddies have a smaller spanwise extent than those in the wake of the cylinder so the blade response is more impulsive. The overall SPL increase in the case of the cylinder wake is due to the increased turbulence intensities within the boundary layer.

Further configurations for turbulence ingestion were developed by Hickling [47] and Balantrapu [14] and included an axisymmetric body of revolution with a rotor at the tail ingesting the turbulent boundary layer developed by the body surface. A schematic showing the axisymmetric body of revolution model as studied is shown in figure 2.10. Initial development of the model included 1/4 scale model tests as well as no-rotor wake analysis using a rotating pitot probe rake. The body was designed such that no flow separation occurred at the corner and this was confirmed through RANS calculations as well as the previously mentioned 1/4 scale model tests. In [15] Balantrapu et al. examine a number of flow measurements for the turbulent boundary under adverse pressure gradient and body curvature effects. These results from the body of revolution test were done under the umbrella of turbulence ingestion noise research but are applicable to more general adverse pressure gradient boundary layer research. He used several scaling methods including a Zagarola-Smits scaling ($U_{zs} - \delta$), a standard edge velocity and boundary layer thickness/displacement thickness scaling ($U_e - \delta / U_e - \delta_1$) and an embedded shear layer scaling developed by Schatzman and Thomas [78] to attempt to collapse the turbulence statistics profiles within the strong APG flow region. The ESL scaling worked well under the strong adverse pressure gradient, non-equilibrium flow. Perhaps the most relevant finding from this paper is the effect of

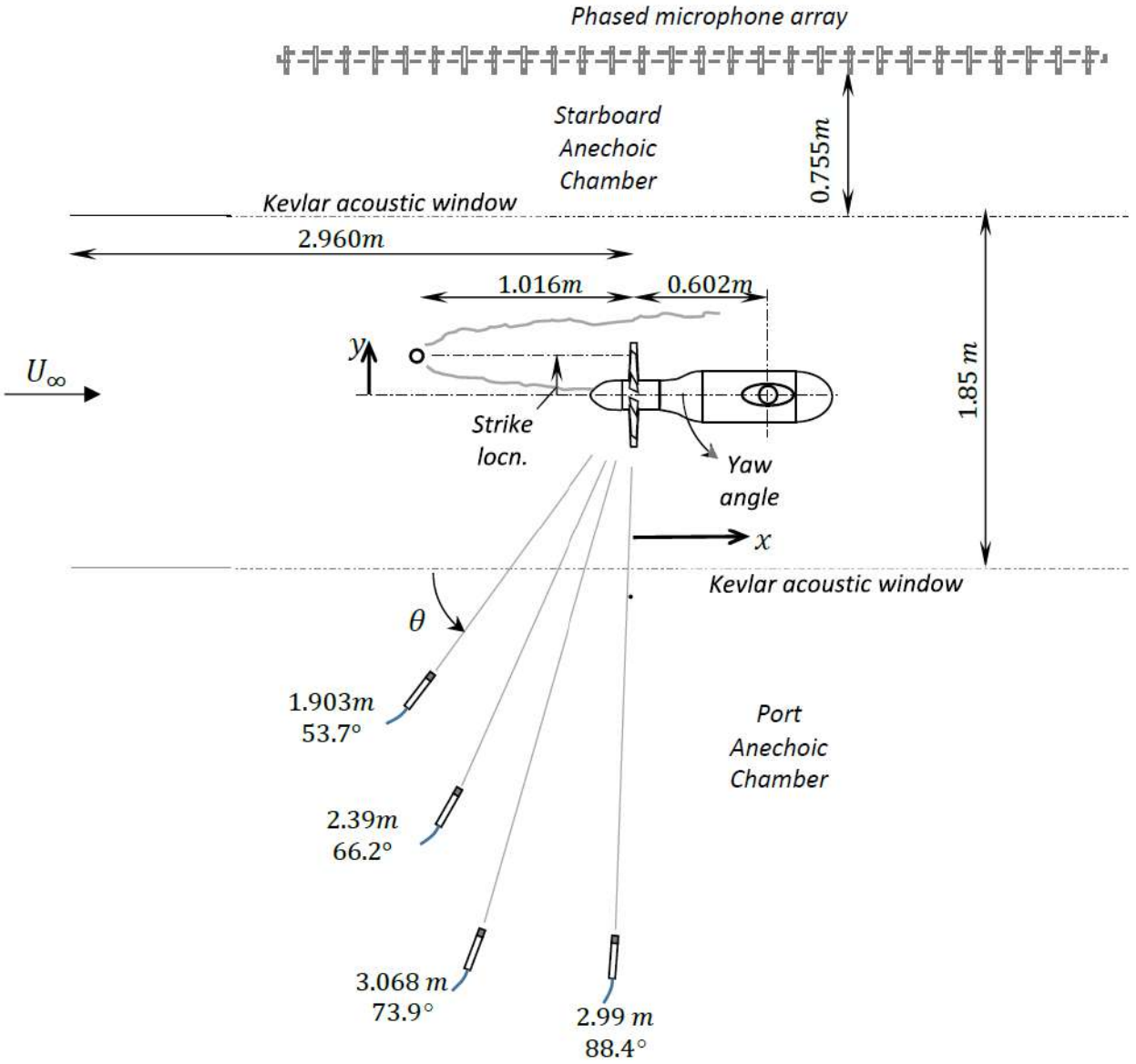

Figure 2.9: Experimental schematic illustrating the experimental setup for the rotor/cylinder wake interaction discussed in [6] and [67].

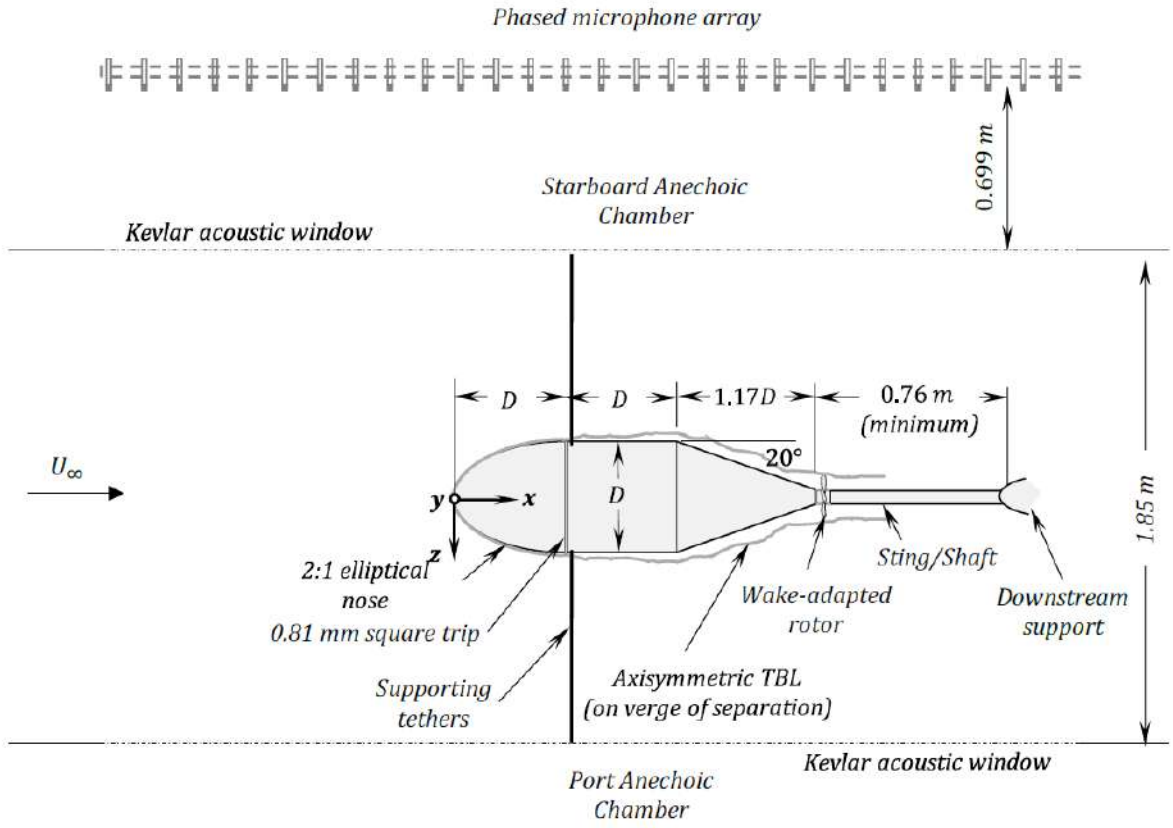

Figure 2.10: Schematic showing the axisymmetric body of revolution model as tested. Image courtesy of [47].

non-linearities on the apparent eddy convection speed when estimating length scales using single point statistics. Using two point correlations calculated from the PIV measurements and the single point correlations calculated from the hotwire measurements, he found that single point statistics and Taylor's hypothesis underpredict the integral length scales within the inner part of the boundary layer, with the predictions worsening closer to the wall.

2.3 Transient Disturbance Ingestion into Open Rotors

Research into the effect of transient disturbances and vortex ingestion into rotor systems has largely been restricted to helicopter blade vortex interaction applications. Typically the response to a blade vortex interaction is most pronounced when the vorticity vector of the shed tip vortex is aligned parallel to the blade span. The blade vortex interaction then occurs impulsively and is nearly perfectly correlated with the successive blade passages. The resultant sound spectrum is dominated by an impulsive, tonal response. This condition occurs only at specific flight conditions when the rotor blades cut the tip vortices of the preceding blade in the correct orientation to produce this sound. Some of the earliest forays into this field were undertaken by Leverton and Taylor [57]. Then referred to colloquially as blade slap, they simulated a blade vortex interaction by blowing two jets of air in opposite directions, normal to the blade surface, slightly offset from each other. This induced a sinusoidal velocity variation as the rotor passed through the two jets that approximated a gust impulse. Furthermore they were able to vary the vortex configuration by changing the vortex circulation and phase shifting the resultant gust. The configurations are shown below in Figure 2.11.

Consider, instead, a vortex with a vorticity vector that is aligned perpendicular to the blade. Rather than an impulsive sound source, this sound source is non-deterministic and causes

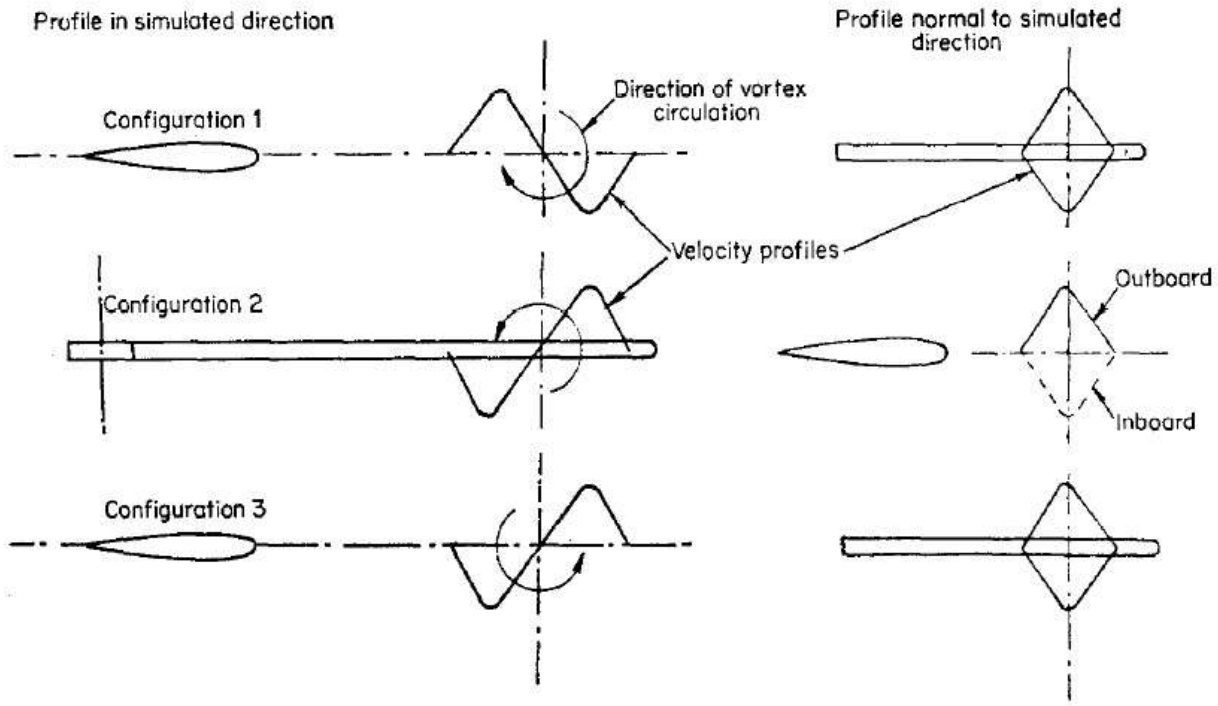

Figure 2.11: Vortex configurations for Leverton and Taylors investigations into blade slap (Blade Vortex Interactions) [57].

broadband blade wake interaction noise. The way this generates broadband sound is in the interaction of the turbulence within the vortex with the blade. As the blade cuts through the vortex the angle of attack of the blade varies stochastically and generates an unsteady force on the blade, radiating sound into the far field. This type of blade wake interaction was studied to some extent by Wittmer et al. [40], [87], [89], and [88]. In a pair of papers Wittmer et al. [88], [89] examined the effect a downstream blade had on a vortex at various blade-vortex separations, blade angle of attack, and vortex strength. They found that for blade-vortex separations less than 30% of the blade chord, the circulation of the vortex weakens and the size of the vortex expands to become significantly more turbulent over a larger area (approximately 70% of the blade chord). This implies that the sound signature for perpendicular blade-vortex interaction on subsequent blade passages is likely to be a

broadband response, rather than an impulsive one.

The interaction of ship wakes with a helicopter rotor system is a source of significant interest for many due to the incorporation of helicopter operations on many naval ships around the world. Ship airwakes are characterized by highly unsteady vortex interactions with flow separation over the hanger deck which leads to the generation of horseshoe vortices, and downstream reattachment [80]. These flow structures have been shown to be energy dominant at low frequencies, between 0.1 and 10 Hz [45], [53]. Other experimental studies by Lee and Zan [55] have demonstrated that a majority of the turbulent energy is significant below 0.5 Hz.

Nacakli [73] aimed to understand the interaction between rotor downwash and the ship airwake and identified regions in the ship airwake that were statistically coupled with the rotor interaction. He did this by first taking isolated flow measurements of a scale model ship and rotor wake and then taking coupled flow measurements with both in place. Other studies by Healey et al [53] have demonstrated that the overall ship airwake flow is Reynolds number independent above 10^4 however the Reynolds number impact on the rotor/ship airwake interaction has not been studied [80].

While these studies have produced a reasonable understanding of some of the turbulent flow physics within the ship airwake/rotor interaction, it is currently unclear how the transient interactions within the above studies affects the noise radiated by rotors. Furthermore the effects of the rotor/ship airwake coupling on the unsteady nature of the interaction warrants further examination.

2.4 Flow About Slender Bodies of Revolution at Angle of Attack

A further example of a potentially anisotropic flow field that is often ingested into rotors is the wake shed by a slender body of revolution. In this case the focus is on bodies with a length to diameter ratio greater than 3:1. The following studies examine flows with body length based Reynolds numbers on the order of $1x10^6$to $5x10^6$.

Studies from as early as the 1930's show evidence of two concentrated vortices in the wake of a body of revolution when inclined at angles less than 15^o in subsonic flow. Harrington [44] was one of the first to determine the existence of these body vortices. He made measurements of the velocity in the wake of an ellipsoid of revolution with a length to diameter ratio of 6:1 at angle of attack using a yawmeter. From iso-vorticity plots downstream of the body the existence of a vortex sheet rolling up into a pair of asymmetric strength vortices was discovered. This research showed the existence of the wake vortices but made no measurements along the body to determine their origin.

Further evidence of the concentrated vortex pair in the wake of a highly slender body at low angles of attack was found by Spence and Trebble [81]. At subsonic speeds and small angles of attack they concluded that a spiral vortex sheet developed on the body lee side and gave rise to a pair of counterrotating, concentrated vortices both along the aft sections and in the wake. Above 10^o the vortices in the wake became asymmetric. Eichelbrenner and Oudart [33] redefined three dimensional separation to be the flow seeking a more favorable pressure gradient while still remaining attached to the body. This differs from the typical two dimensional, detached flow associated with two dimensional separation and allows for a more robust examination of separation in the case of three dimensional bodies. Rodgers [76] however suggests that the vortex sheet rolling up into a pair of concentrated vortices is

a highly simplified model of the real three dimensional flow and in fact does not exist over the length of the body. While he is correct that the flow is not simple, multiple subsequent studies have shown the body vortices can be highly coherent at low angles of attack. Lloyd and Campbell [59] studied the flow along a body of revolution moving in a curved path at a Reynolds number of 1x10^6 and a length to diameter ratio of 8.5. They found that, at low angles of attack, a region of high vorticity can be found between the lee and side of the body which grows in strength with distance downstream. Chesnakas et al. ([26], [27], and [28]) examined the turbulent structure of the flow about a 6:1 prolate spheroid at Re_l=4.2x10^6 and quite clearly show the existence of the primary vortex at 1x10^o and demonstrate that the formation of this vortex is as a result of separation on the side of the body and reattachment towards the lee of the body. They further show that secondary and even, tertiary vortices can form from multiple separation and attachment regions that increase as a function of angle of attack and Reynolds number.

To qualitatively understand the effect of angle of attack and Reynolds number on separation over the same 6:1 prolate spheroid studied by Chesnakes, Ahn [2] used oil flow interferometry to determine the location of the primary and secondary separation regions. These tests were undertaken at length based Reynolds numbers from 2.85x10^6 to 4.2x10^6 and angles of attack from 5^o to 30^o and the results are shown in figure 2.12 and 2.13. As the angle of attack increases the separation line extends further upstream and towards the lee side of the body. Towards the tail the separation line shifts towards the windward side for all angles of attack but specifically for $\alpha = 5^o$ the gradient of the separation line is quite dramatic.

Measurements of a turbulent wake for a body of Re_l = 2.4x10^6 up to 30x10^6 at angles of attack from 0^o to 12^o were conducted on the DARPA SUBOFF submarine model by Ashok et al. [11]. The DARPA SUBOFF model is a standardized submarine idealization that is axisymmetric with an overall length to body diameter ratio of 8.6:1. The forebody is twice the

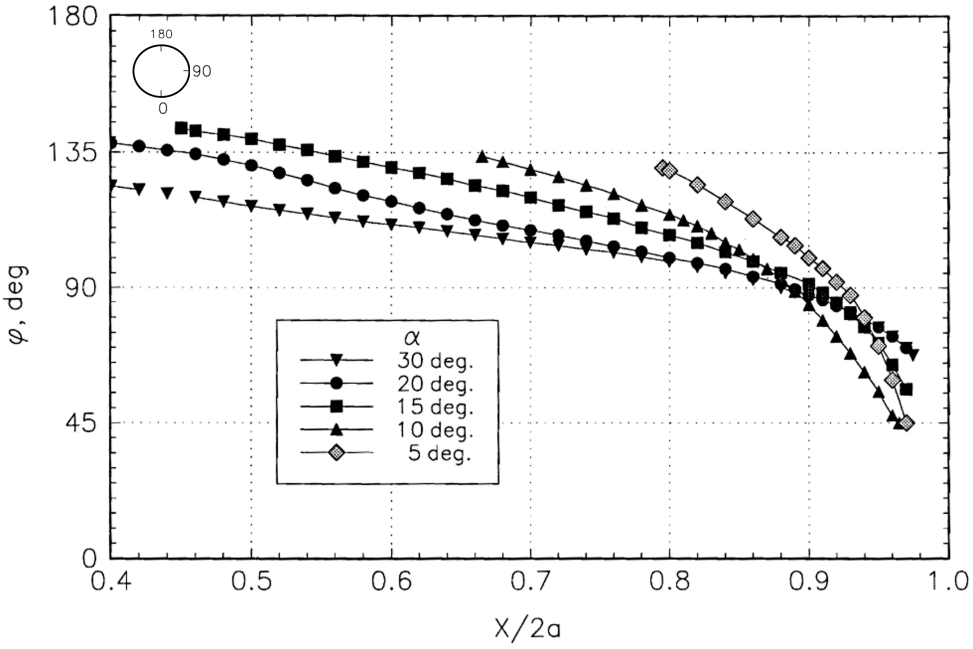

Figure 2.12: Effect of angle of attack on the location of the primary separation line for a 6:1 prolate spheroid at $Re_l = 4.2\text{x}10^6$ (Ahn [2])

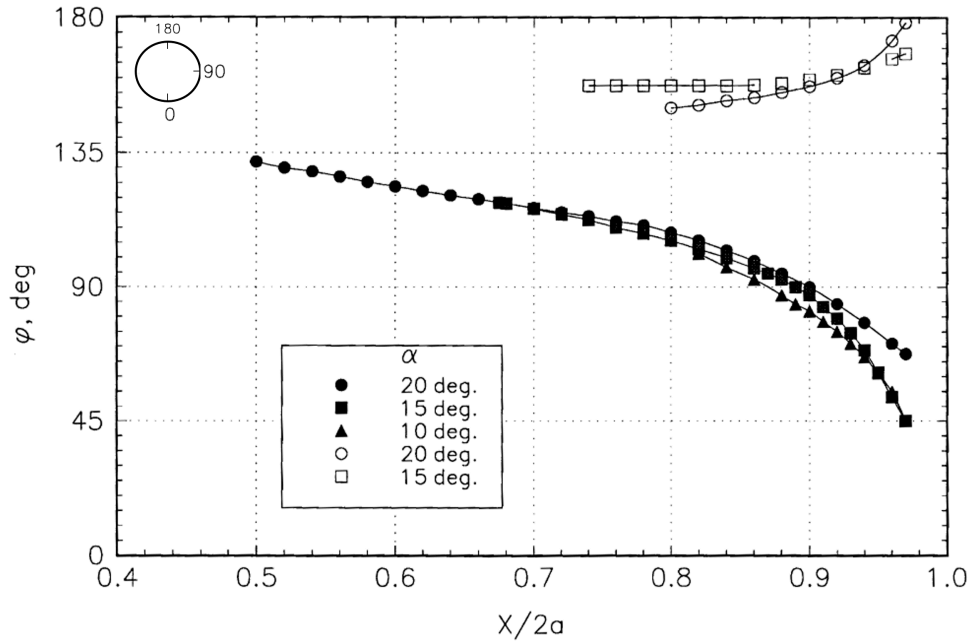

Figure 2.13: Primary and secondary separation locations for a 6:1 prolate spheroid with a $Re_l = 2.85x10^6$ and varying inclination angles between 10^o and 20^o. The primary separation radial position is given by the closed symbols, while the secondary separation location is given by the open symbols (Ahn [2]).

maximum body diameter in length and the afterbody tapers gradually with a length to body diameter ratio of 2.2. Velocity measurements using single component hotwires and stereo particle image velocimetry was done within the wake at distances of $x/D = 2, 5, 8, 11, 16, 21,$ and 26 downstream of the body. At small streamwise separations from the body the vortex pair appeared well defined but fairly asymmetric in all measurements. As the vortex moved downstream the circulation strength and vortex appearance weakened. They suggested that the asymmetry is a result of convective instabilities affecting the vortex evolution downstream of the body.

2.5 Conclusions

A significant body of work has been done investigating the prediction of far field rotor noise from the ingestion of shear layer turbulence. The models typically take one of two approaches, a spectral approach or a correlation approach. With the spectral approach a model for the turbulence spectrum is assumed and then the frequency spectrum of the fluctuating force is calculated by integrating over the blade from hub to tip and over all wavenumbers. In the correlation approach the form of the correlation function is assumed and a blade response function is used to determine the unsteady force applied to the rotor blades. A number of isotropic models have been developed ([60]-[77]) and, in general, these models predict the far field sound spectrum well. However, they break down when applied to anisotropic or inhomogenous turbulence. Attempts to account for anistoropy and inhomogeneity have yielded promising results in Catlett et al. [24] and Anderson et al. [7] but there is still insufficient experimental research into anisotropic, inhomogenous turbulence ingestion into open rotor systems. Glegg et al. proposed a time-domain based semi-analytical formulation that allowed the far field sound spectrum from a rotor operating in a turbulent shear layer

to be calculated provided the two point space-time correlation function is known. Andersons model described in Catlett et al. [24] similarly utilizes a two point correlation function approach that is able to capture the anisotropic nature of a sheared boundary layer in the radiated noise. The subsonic flow about bodies of revolution at various angles of attack is fairly well studied and understood. A pair of counterrotating vortices develop over the length of the body on the lee side caused by 3 dimensional separation and reattachment on the body. These can further roll up into secondary and tertiary vortices if the length based Reynolds number is high enough or the body is at sufficient angle of attack. These vortices then convect into the wake of the body with an asymmetric strength based on convection instabilities. Research into the far field radiated acoustics of a vortical velocity transient ingested into an open rotor has previously been limited to blade vortex/wake interactions. Limited investigations into the ingestion of vortical disturbances with larger time scales than the blade passage frequency into open rotor systems have been undertaken.

Chapter 3

Research Motivation

The proliferation of Personal/Unmanned Aerial Vehicles in urban spaces drives the need for fundamental research into the physics of turbulence ingestion noise. Understanding this allows future acousticians and design engineers to design rotor systems with noise reduction as a design constraint. The motivation for this proposal comes from consideration of real world, practical configurations. Researchers in the past such as Sevik [79], Wojno ([91], [**?**], [90]), Lynch([61], [62], [90]), Martinez ([65], [66]), and Jiang [52] to name a few, have generally confined their experimental studies to grid generated, homogenous turbulence. Furthermore the models used typically assume isotropy and homogeneity in their development. This greatly simplifies the modelling process but vastly underestimates the complexity of real world turbulent flows. As evidenced in the literature review the models developed for isotropic flows break down when applied to turbulent inflows with significant anisotropy and inhomogeneity. Research into the effect of a variety of different rotor/control surface/fluid interactions is necessary for the advancement of the science. Difficulties arise in rotor leading edge noise prediction when the rotor encounters significant anisotropy and inhomogeneity in the inflow turbulence. These can take the form of physical surfaces upstream that modify the turbulence in some manner. For example an upstream appendage will introduce vorticity shed from its trailing edge, or a turbulent boundary layer along a curved surface will experience distortion as the boundary layer is subjected to the pressure gradient. Furthermore thrust from the rotor itself induces a pressure gradient that often tends to stretch the turbulence

in the streamwise direction. This is evidenced in Hanson [43] and Majumdar and Peake [64]. Glegg et al. [39] showed that the broadband rotor noise can be predicted if the upwash correlation function $R_{ww}^{(n,m)}(R, R', \tau_0, \tau_0')$ is known. The correlation function is used to find the fluctuating force applied to the blade and then the far field noise is computed using the solution given to the Lighthill wave equation by Ffowcs-Williams Hawkings [85] and a suitable Green's function.

This dissertation improves the current knowledge base of the engineering community with respect to turbulence ingestion noise in specific rotor systems. It does this by quantitatively expanding the understanding of the mechanisms of turbulence ingestion noise in a body of revolution configuration with an aft ramp, as well as the transient noise generated by the interaction of a rotor with a disturbance. Specifically the research objectives are to:

$\Rightarrow$ demonstrate how separation and the resulting anisotropy in the mean flow and turbulence structure at the tail of a body of revolution can lead to broadband noise contributions that could not be predicted with homogeneous turbulence assumptions.

$\Rightarrow$ reveal how the circumferential non-uniformity in the body of revolution flow physics and intensity of the turbulence leads to unexpected directivity in the sound field.

$\Rightarrow$ identify whether a two dimensional embedded shear layer scaling can be applied to the three dimensional embedded shear layer developed over the body of revolution.

$\Rightarrow$ determine the extent to which the turbulence two point correlation function is stretched in the streamwise and circumferential directions and how the distortion affects the eddy structure and sound field.

$\Rightarrow$ understand the extent to which the rotor affects the turbulence statistics in the rotor near field within the embedded shear layer and on the lee side.

⇒ show how the generation of sound from transient disturbances produced by a moving control surface embedded in a boundary layer are primarily the result of unsteady behavior in the control surface.

⇒ reveal that the balance of sound generated by deterministic components of the disturbance, phase-locked to the control surface, dominate over broadband components associated with the turbulence it contains.

Thus in Chapter 4 we will examine the three dimensional flow about a body of revolution at two locations and infer an overall flow structure based on these measurements. Vortex rollup in the lee of a body of revolution at angle of attack is a well documented phenomenon and this chapter will attempt to identify whether the vortices interact with the rotor and have an impact on the turbulence ingestion noise. Chapter 5 looks to determine how the inclination of the body of revolution introduces asymmetries in the turbulence, how the upwash correlation function is distorted by the inhomogeneity, and what effect that might have on the sound radiated by the rotor. Furthermore the links between the noise and noise sources during a rotor transient turbulence interaction introduced by an upstream disturbance generator will be identified in Chapter 6. Overall this dissertation will seek to establish an experimental basis of the effects three dimensional separation, flow anisotropy, and flow transients have on the turbulence structure of the flow and therefore the radiated noise. It will form an experimental base against which further anisotropic models can be developed and validated.

Chapter 4

Turbulence Ingestion of an Axisymmetric and Non-Axisymmetric Wake Into an Open Rotor

4.1 Context

This paper examines how separation and anisotropy in the turbulence structure at the stern of a body of revolution results in noise radiation with unexpected directivity effects that could not be predicted using a homogenous turbulence assumption. It identifies the impact of three dimensional separation on the flow and sound radiated by a rotor ingesting a boundary layer developed over the length of a body of revolution at 5^o angle of attack. It identifies key flow phenomena typical of inclined slender bodies and shows that the ingestion of an embedded shear layer is a primary driver of sound generation. It also examines the effects of the flow anisotropy on the correlation function in the $x-r$ and $r-\theta$ plane and discusses the impact this has on the radiated sound.

4.2 Acknowledgement of others' work

Chapter 4 is a journal paper that is under review. It contains work from Humza Butt in the form of the acoustic spectra in Section 4.6.6 (figure 4.24) and the pressure measurements in Section 4.6.1 (figure 4.12). Comparisons to measurements taken by Balantrapu [14] and Hickling [47] of the body of revolution at 0^o angle attack are presented. All other analysis and work was done by Jarrod Banks.

Author List: Jarrod T. Banks, Humza Butt, Agastya N. Balantrapu, Nathan W. Alexander, William J. Devenport

4.3 Abstract

The turbulent inflow to a rotor at the tail of a body of revolution (BOR) was studied at 0 and 5 degrees angle of attack. The body of revolution consists of a 2:1 ellipsoidal nose, a straight midbody and a 20 degree tail ramp that narrows towards the rotor mounted on the aft of the BOR. Measurements of the mean pressure along the body, velocity in the vicinity of the rotor, and radiated noise were taken principally at a Reynolds number of 600,000 based on the body diameter. The mean velocity and turbulence within two axially oriented planes at the aft of the body of revolution on the lee and port side were examined using time resolved particle image velocimetry. A circumferential plane between the lee and starboard side was also measured. Measurements showed a significant decrease in the turbulence levels on the lee side when compared to previous measurements made by Balantrapu et al. (2021) of the same body at 0 degree angle of attack. On the port side, levels were approximately twice that of the 0 degree body and the wake profiles were comparable. The increase in the turbulence on the lee side was due to the separation and formation of a shear layer that then rolls up into a vortex near the lee side. Beamforming of the rotor response at two acoustic measurement planes showed increased sound production radiated towards the lee of the body.

4.4 Introduction

In many engineering applications, rotors interact with turbulence. This turbulence excites unsteady loading on the rotor blades that can radiate as sound to the far field, resulting in unwanted community noise. The impact of turbulence ingestion noise (TIN) is exacerbated if the turbulence is of sufficient scale to produce unsteady loads which are correlated from

blade-to-blade (i.e. if the convecting turbulent structures are cut multiples times by the rotor blades as they pass through the rotor disc plane). In this case, broadband humps or haystacks appear in the loading and consequently noise spectra at the blade passage frequency (BPF) and its harmonics. Furthermore, if standing flow structures exist within the rotor disc, coherence between blade passages can result in tone generation about the blade passage frequencies. Sevik [79] was among the first to observe this phenomenon, and significant research over several decades has resulted in many different models of the blade-to-blade correlation effects and prediction of the haystacking phenomenon for homogeneous, isotropic turbulence. Blake [20] superimposed large wavenumber and small wavenumber spectra to obtain an overall spectrum while Jiang et al. [52] proposed a modelling approach using an approximation of the turbulence correlation function, rather than assuming a turbulence spectrum. However some of the more successful analytical models use a time-domain approach. Glegg et al. [39] showed that if the full 4-dimensional space-time correlation structure is known a priori the broadband and haystacking components of the acoustic spectra can be well predicted. In practice, this is done by measuring the 4D correlation structure and calculating the upwash correlation function. The upwash correlation function is then used as an input in calculating the unsteady lift spectrum and finally the sound spectrum is determined from the unsteady force applied to the rotor blades. Of specific importance to this calculation is the shape of the correlation function, the length scales in the upwash direction, and the intensity of the turbulence. The shape of the correlation function and hence the length scales in the flow are typically positively correlated with an increase in haystacking observed around the blade passage frequencies, while the intensity of the upwash turbulence affects the broadband sound levels. The extent to which each component affects the noise will be examined in this paper. The equation governing the noise spectra developed in Glegg et al. [39] is shown below,

$$S_{pp}(\overline{x},\overline{\omega}) = \frac{1}{4\pi T}\sum_{n=1}^{B}\sum_{M=1}^{B}\int_{R_{min}}^{R_{max}}\int_{R_{min}}^{R_{max}}\int_{-T}^{T}\int_{-T}^{T}\{arg\}\,dRdR'd\tau d\tau' \tag{4.1}$$

Where the argument { arg } is given below

$$\left\{\frac{\partial}{\partial x_i}\frac{n_i^{(n)}(R,\tau)e^{i\omega r^{(n)}(\tau)/c_o}}{4\pi r^{(n)}(\tau)}\right\}\left\{\frac{\partial}{\partial x_j}\frac{n_j^{(m)}(R',\tau')e^{-i\omega r^{(m)}(\tau')/c_o}}{4\pi r^{(m)}(\tau')}\right\}R_{FF}^{(n,m)}(R,R',\tau,\tau') \tag{4.2}$$

The term in {arg} is derived from the expected value of the pressure correlations on the blade at different times while incorporating the Ffowcs-Williams and Hawkings solution of Lighthills equation (Williams and Hawkings [85]). The free field Greens function,

$$G_0 = \frac{\delta(t-\tau-r(\tau)/c_\infty)}{4\pi r(\tau)} \tag{4.3}$$

is the most appropriate Greens function and is used by Ffowcs-Williams and Hawkings in this solution. The power spectrum is then calculated by integrating the pressure correlation term from the rotor hub to the tip then summing over all blades B. However, the part of the equation driven by the results in this paper is the unsteady force term $R_{FF}^{(n,m)}(R,R',\tau,\tau')$. This is the expected value of the unsteady force on the blade correlated with itself and can be found at low mach numbers using a combination of the Kussner function (Leishman [56]) and the unsteady upwash correlation function. Now the unsteady upwash correlation function is a simple function of the turbulence correlation function R_{ij}. The streamwise component of R_{ij} is dominant in the upwash correlation function and this paper will examine this quantity in detail.

The work of Hanson [43], Majumdar and Peake [64], and Atassi and Logue [12], has emphasized the importance of flow anisotropy on haystacking and shown that haystacking can be greatly enhanced when the turbulence is distorted as it is drawn into a thrusting rotor.

Turbulence stretching at the inflow to a rotating fan was discussed in Majumdar and Peake [64] and the stretching of the turbulence and its effect on flow lengthscales and subsequently the far field radiated noise is discussed. They developed a theoretical model using the von Karman spectrum for isotropic turbulence and distorted the wavenumber to simulate turbulent eddy elongation. The distortion at the fan inflow was modeled using rapid distortion theory and the sound radiation to the far field is calculated using a Green's function approach and asymptotic theory. For takeoff conditions the turbulence within the streamtube was strongly distorted due to the quiescent air surrounding the fan, allowing the fan thrust to more strongly distort the turbulence as it is ingested. However for inflight conditions the turbulence distortion is significantly weaker and the spectral humps were less prominent in the acoustic spectra. A similar study was conducted by Hanson [43] for a rotor in static conditions and significant stretching of the streamwise eddies was found; up to lengthscale ratio of 400:1 between the streamwise and transverse directions. These resulted in highly narrowband spectral humps within the acoustic spectra. A similar, almost tonal, response to ingested turbulence was seen by Murray et al. [72] when operating a rotor in the vicinity of a flat zero pressure gradient wall. Large spectral peaks were seen at the blade passage frequency and standing vortices within the tip gap were noted. Further speculation that these standing vortices acted as a form of Blade Vortex Interaction (BVI) was made. It was posited that the standing vortices induced high velocity correlations between successive blade passages such that the energy within the sound was concentrated about the blade passage frequencies.

More recently the work of Catlett et al. [24] and Anderson et al. [9] shows the effects of inhomogeneity and non-stationarity on TIN predictions. Measurements of an anisotropic turbulence field ingested by a rotor mounted at the back of an airfoil were taken and predictions using an isotropic and an anisotropic turbulence model were compared. Distortion

of the correlation function in space to achieve an anistropic two point correlation function was achieved using a coordinate system modification. This showed improved haystacking predictions while using an isotropic correlation function failed to capture the extent of the haystacking peaks. In all flow cases, accurate prediction of TIN and the haystacking phenomenon requires detailed knowledge of the turbulent inflow seen by the rotor and the unsteady loading response of the blades to that inflow. Extending investigations of anisotropic, inhomogenous turbulence ingestion to practical configurations the turbulent inflow into a rotor mounted at the aft of a centerbody can be considered.

Investigations into the axisymmetric flow about a body of revolution with an aft ramp and a rotor mounted at the tail was undertaken by Balantrapu et al. [15]. Flow was shown to be mostly axisymmetric without the presence of the rotor due to the lack of swirl evident in the flow fields. A turbulence peak in the axial direction ($\overline{u_x^2}$) centered around 0.4δ just downstream of the start of the ramp was found as the boundary layer was traversed from the body surface to boundary layer edge. This peak was shown to weaken in intensity and shift away from the body surface moving downstream as the axially aligned pressure gradient increased. This is contrary to previous studies on flat plates and is attributed to the effects of the transverse curvature of the body. The measured peak at the body tail occurred at 0.55δ with a peak intensity reduction of around 20% when compared with the peak at the start of the ramp. The peak was associated with the inflection point of the mean velocity profiles and is shown in figure 4.1. A number of scalings were investigated including an embedded shar layer scaling (described in Schatzman and Thomas [78] and Section 4.6.3), δ_1, and δ_2 scalings given by equations 4.4 and 4.5.

$$\delta_1 = \int_0^{\delta} (1 - U_s/U_e) d(|z - z_s|) \tag{4.4}$$

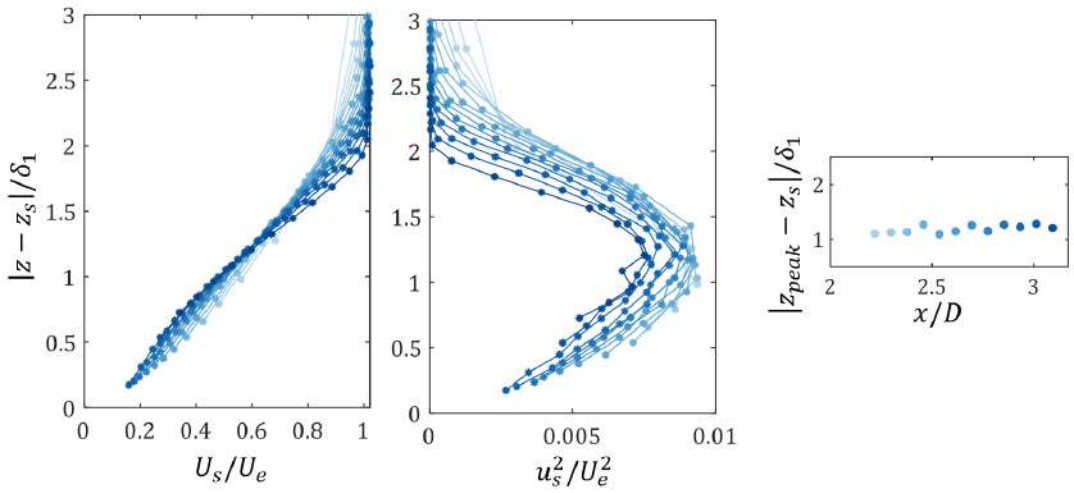

Figure 4.1: From left to right: mean velocity profiles with $U_e - \delta_1$ scaling, profiles of the axial Reynolds stress (u_s^2) with the $U_e - \delta_1$ scaling, location of the peak axial Reynolds stress scaled on δ. Balantrapu et al. [15]

$$\delta_2 = \int_0^{\delta} (U_s/U_e)(1 - U_s/U_e) d(|z - z_s|) \tag{4.5}$$

When scaled on an embedded shear layer scaling the mean velocity and turbulence profiles collapse to some extent and appear mostly self similar. This collapse is shown in figure 4.2. The error function of η defined by $\frac{2}{\sqrt{(\pi)}} \int_0^{\eta} e^{-t^2} dt$ is plotted and the mean velocity data is shown to collapse neatly onto the error function between $\eta = -1$ to 2.

The effect of the rotor in thrusting and braking conditions on the turbulence was also investigated in Balantrapu et al. [15]. It was seen that the distortion of the turbulence from the rotor thrust can be approximated by assuming the rotor applies a local mean pressure gradient on the flow. For advance ratios lower than 1.44 (i.e., when thrusting) the velocity profiles are fuller and the axial Reynolds stress weakens when measured in the vicinity of the rotor, while the opposite trends occur for advance ratios higher than 1.44 (i.e., when braking). However, the effect of the thrust only weakly varies the turbulent kinetic energy, redistributing the energy from the axial to the spanwise directions.

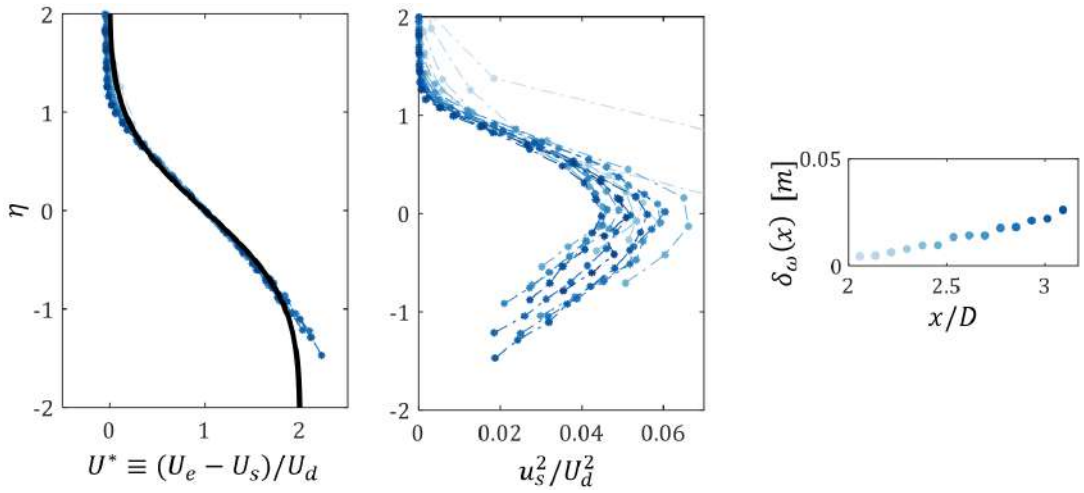

Figure 4.2: Embedded Shear Layer scaling of: (from left to right) mean velocity profiles, axial Reynolds stress (u_s^2) profiles, and boundary layer vorticity thickness as a function of x/D. Profiles taken at varying x/D positions from $x/D = 2$ to $x/D = 3.17$ and range from light to dark moving downstream. Balantrapu et al. [15]

Of course the inflow to a rotor on a vehicle is never two dimensional or axisymmetric due to vehicle maneuvers, unsteady wind/currents, and other variables. Three dimensional effects are seen when inclining a body of revolution at an angle of attack to a flow. Kumar and Prasad [54], Tinling and Clyde [83], and Rodgers [76] describe the presence of a pair of asymmetric, counter-rotating vortices that develop on the leeward side of a slender body of revolution when inclined at an angle of attack. These vortices are likely to have significant effects on the turbulence in the turbulent boundary layer.

In an effort to understand the typical structure of the subsonic, incompressible flow around a slender body of revolution at angle of attack the work of Ahn [2], Chesnakas [26], Chesnakas and Simpson [28], and Chesnakas and Simpson [27] will be examined. All of these researchers investigated the flow about a 6:1 prolate spheroid at angle of attack. A vortex sheet develops over the length of the spheroid with its initiation point, or primary separation point, depending strongly on the angle of attack, with a weak variation with Reynolds number. With sufficiently high angle of attack a secondary separation and reattachment

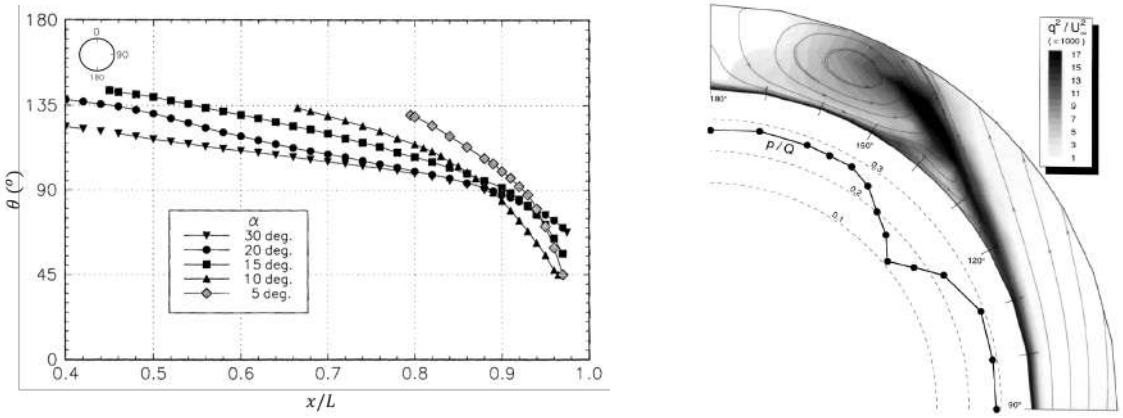

(a) (b)

Figure 4.3: a). Effect of angle of attack on the location of the primary separation line for a 6:1 prolate spheroid at $Re_l = 4.2x10^6$. Modified from [2]. b) Distribution of turbulent kinetic energy in the cross flow plane of a body of revolution inclined at 20^o angle of attack. The measurements were taken at x/L=0.600 and at $Re_l = 4.2\text{x}10^6$. Chesnakas and Simpson [29]

point was found. Ahn [2]'s research varied the Reynolds number and angle of attack and examined the effect this had on the three dimensional separation that occurs between the lee and port/starboard sides. As the angle of attack increases the separation line extends further upstream and towards the lee side of the body (see figure 4.3a). Towards the tail, the separation line shifts towards the windward side for all angles of attack but specifically for $\alpha = 5^o$ the gradient of the separation line is quite dramatic.

Examining the distribution of turbulent kinetic energy (TKE) in Figure 4.3b, separation from the body, indicated by where the sheet of high TKE fluid leaves the body surface, is seen around $\phi = 120^o$. The primary TKE sheet continues separating as the flow moves along the body and rolls up into a vortex between $\phi = 140^o$ and 170^o. The flow on the lee side of this body shows significantly depressed turbulence levels outside of a small region very close to the body. The depressed turbulence levels are due to attachment occurring near this region and bringing with it lower turbulence free stream fluid.

Little effort has been undertaken to investigate the sound radiation from the interaction of a rotor with such a three dimensional flow and this paper aims to contribute to the community's understanding of these phenomena. As a result this paper will investigate leading edge noise radiated by a rotor ingesting a three dimensional boundary layer with circumferential variation in the turbulence levels. The axial velocity and turbulence at the rotor inflow plane at two circumferential locations about the body of revolution will be examined to determine the effect of the angle of attack on the character of the turbulence. An important input to several prediction methods is the two point correlation of the blade upwash velocity and as such the distortion of the axial two point correlation function at two different locations about the body will be investigated. This paper aims to provide experimental data to inform existing models that seek to predict the noise for a practical configuration, such as a vehicle performing a turn, or a maneuver in which the flow is non-axisymmetric. The existence of an embedded shear layer that travels up the side of the body as a result of the body angle of attack will be examined in the mean velocity, turbulence, and shear stress profiles. The effect that both the embedded shear layer and the correlation function distortion might have on the acoustics of the rotor will be theorized.

The paper structure is as follows; the experimental facility, model, rotor, and measurement apparatus will be described in Section 4.5 and the reader oriented with the coordinate system. In Section 4.6.1 the mean circumferential and axial pressure will be discussed followed by a description of the mean flow and turbulence near the rotor in Section 4.6.2. The embedded shear layer analysis will be shown and discussed in Section 4.6.3 and the correlation function examined in Section 4.6.5. Section 4.7 summarizes the main findings including that the variation in the turbulence and correlation function distortion is as a result of three dimensional effects stemming from the inclined body of revolution. These act to separate a sheet of high turbulent kinetic energy from the body that travels up the side of the body

and rolls up into a pair of counterrotating vortices on the lee side. Both the highly turbulent region and vortices interact with the rotor and act to increase the broadband noise surrounding the blade passage frequencies.

4.5 Experimental Methodology

4.5.1 Experimental Facility

Experimental measurements were made in the Virginia Tech Stability Wind Tunnel (VTSWT) in anechoic configuration. The 1.85 m x 1.85 m x 7.32 m test section is enclosed by two Kevlar side walls and a floor and ceiling formed from Kevlar covered panels treated to minimize acoustic reflections. Maximum flow capability of this facility is 80 m/s with freestream turbulence levels less than 0.01% at 20 m/s and a freestream uniformity of 0.5% at 47 m/s. Devenport et al. [32] goes into further detail of the VTSWT's capabilities. Figure 4.4 shows the two orientations of the body of revolution as tested. A test section centered coordinate system is defined for use in locating the microphone array with respect to the BOR. Figure 4.4 shows the origin of the test section centered coordinate system, X is positive downstream, Y is positive towards the test section ceiling, and Z is positive towards the port wall. The origin is located in the center of the test section, on the test section floor, aligned with the leading edge of the body of revolution when in the pitch down configuration. This global origin is not changed between configurations and Table 4.1 shows the locations of the body of revolution nose and rotor disc center for both configurations. The location of the nose in the yaw starboard configuration is slightly downstream and above the nose location in the pitch down configuration. The axial consistency between the nose and rotor is shown in the consistency between the Z values for the pitch down configuration and the Y values for the

Configuration	Feature	X [m]	Y [m]	Z [m]
Pitch Down	BOR Nose	0.00	0.69	0.00
	Rotor Disc Center	1.45	0.83	0.00
Yaw Starboard	BOR Nose	0.01	0.89	-0.23
	Rotor Disc Center	1.42	0.90	-0.10

Table 4.1: Location of significant physical features of the BOR in test section coordinates.

yaw starboard configuration. In both cases the difference between these values indicates the extent to which the body is physically aligned within its intended plane of rotation (X-Y for pitch down and X-Z for yaw starboard). For the pitch down configuration the Z location of the nose is the same as the Z location of the rotor, while in the yaw starboard configuration the Y location of the nose is within 10 mm of the Y location of the rotor.

4.5.2 Model

The non-axisymmetric flow was produced by the BOR pitched at a 5^o angle of attack. Details of the BOR construction can be found in Balantrapu et al. [15]. It was tested in two configurations; pitch down and yaw starboard. The BOR in both configurations is shown in figure 4.4. It has a diameter (D) of 432 mm and consists of three separate sections. The nose is a 2:1 ellipsoid that produces a favorable pressure gradient. The mid-body is a 432 mm diameter cylinder, and the aft section is a 1.17 diameter long section with a 20°ramp to induce an adverse pressure gradient. The aft ramp narrows to a 50 mm diameter drive shaft on which the 216 mm diameter rotor is mounted. The BOR is made from polyurethane foam and supported internally by 6061 aluminium bulkheads. To allow for instrumentation it is machined out as a hollow piece with a carbon fiber tube running from the drive system to the body. The shell was smoothed and painted to reduce reflections. To ensure a turbulent boundary layer is grown over the length of the midbody, a 0.81 mm trip ring was placed

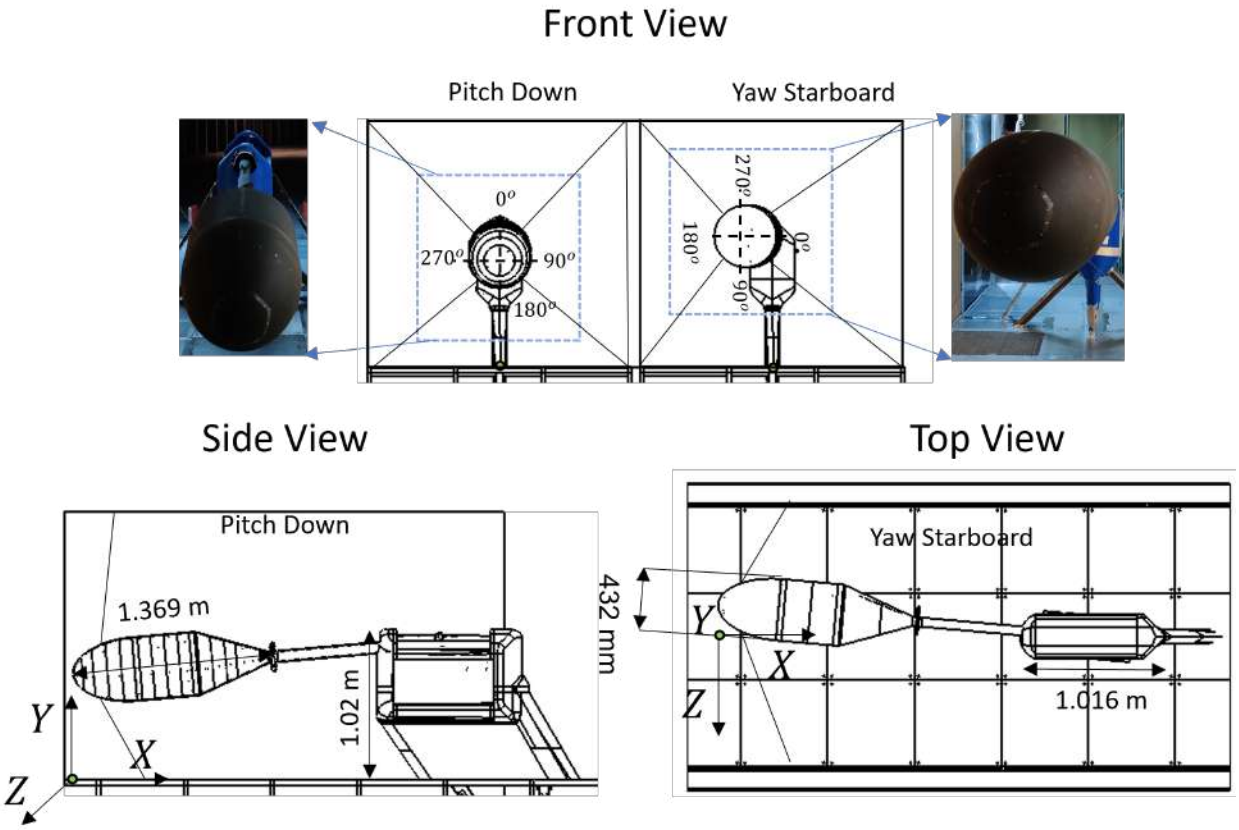

Figure 4.4: Schematic of the experimental setups used to measure different sections of the flow about the body. The top row shows the front view of the pitch down and yaw starboard configurations. The bottom row shows the side of the pitch down configuration and the top view of the yaw starboard configuration. Principal dimensions of the body and structure are shown as well as the approximate location of the tethers.

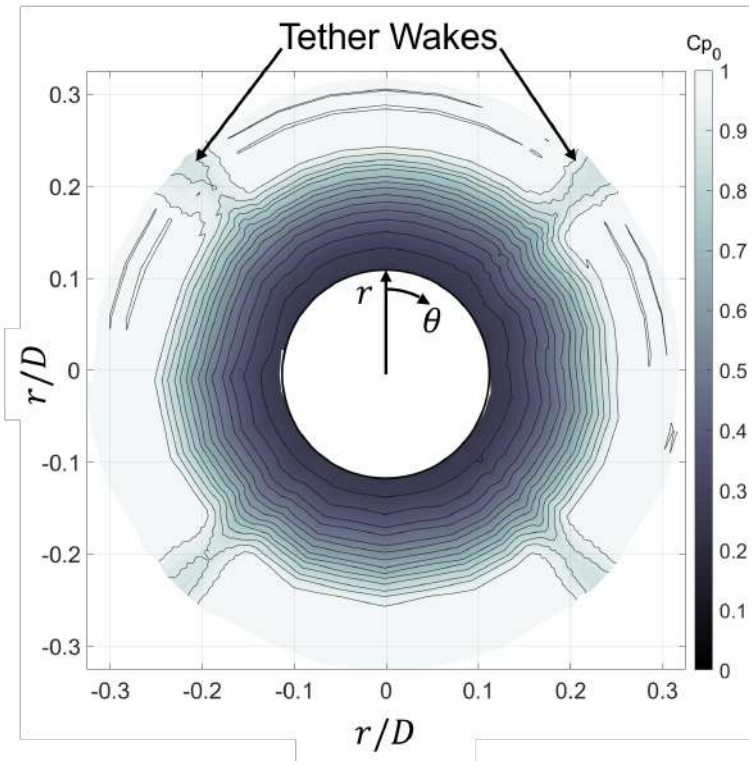

Figure 4.5: Measurements of the stagnation pressure at the rotor inlet ($x/D = 3.17$) showing the effect of the tethers on the flow for the 0°angle of attack. The tethers are located at $\theta = 45°$, 135°, 225°, and 315°.

at $x/D = 0.98$. A tether system consisting of four 1.58mm diameter wires were used to anchor the cantilevered body of revolution in place. The tethers are attached at $x/D = 1$ and extend to the corners of the test section. The effect of the tethers on the flow was examined in [48] and [15] and shown to have a non-negligible effect on the mean velocity and turbulence levels within the wake of the tether, however no effect was noted outside of the tether wake. The effect of the tethers on the cross-sectional mean flow structure at the rotor plane for zero angle of attack is shown in figure 4.5. The positioning of the body of revolution was measured using an inclinometer to be within 0.2°of the targeted 5^o angle of attack shown in figure 4.4. Further confirmation of the angle of attack is done in Section 4.6.1 by measuring the circumferential pressure at $x/D = 0.5$ in both configurations and comparing the results between both configurations as well as to RANS calculations done by

Figure 4.6: CAD of the Zero-Thrust Rotor

research collaborators at the University of Notre Dame (Wang and Zhou [84]). The blockage area of the body of revolution within the test section is 4.3%.

4.5.3 Rotor

The rotor being used in this study is a custom 5-bladed rotor shown in figure 4.6. It has a diameter of half the body diameter (216 mm) and is wake adapted for the axisymmetric wake produced by the body of revolution at 0^o angle of attack. This was done by designing the blade twist to match the mean velocity profile of the body of revolution at 0^o angle of attack for a zero thrust advance ratio of 1.44. Blade sections are a modified NACA 66 airfoil with no camber and the rotor is machined from 6061 aluminium. At 75% radius the blades have a maximum thickness of 6 mm, a pitch of 168 mm and a chord of 57 mm. The rotor has no rake but has a 35.5^o max sectional skew near the blade tip. Rotor scans were completed and determined that the rotor is axisymmetric to within 0.2 mm ([47]).

4.5.4 Drive System

The rotor is mounted by a keyway onto a 50 mm shaft and driven by a Kollmorgen AKM54L-ACCNDA00 servo-motor with a 2.73 gear ratio. The shaft and rotor have a maximum rotation speed of 5000 rpm which limits the advance ratio to a minimum of about 1.27

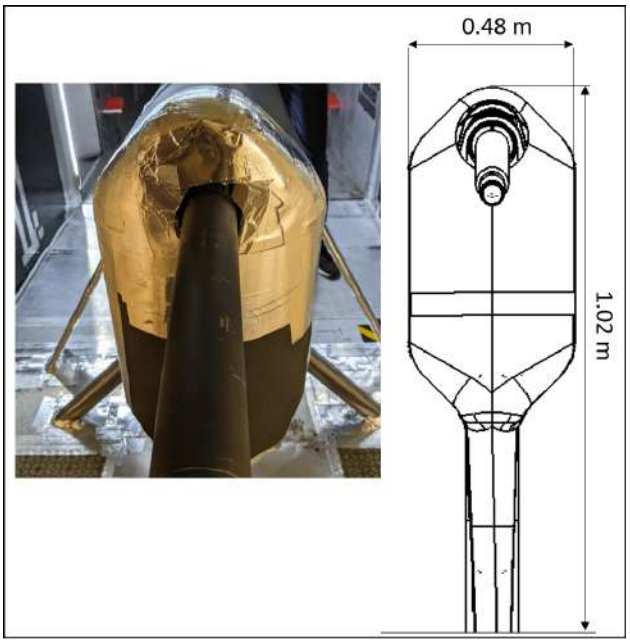

Figure 4.7: Experimental photo showing the acoustic treatment applied to the drive system structure as well as principal dimensions.

at reference conditions ($Re_D = 600,000$). The drive system was faired with a 3D printed aerodynamic structure and acoustically treated with lead vinyl to reduce acoustic radiation from the motor and associated drive components. Figure 4.7 shows an image of the rotor structure with the acoustic treatment installed. The upper structural components used to stiffen the rotor structure and reduce vibrations were faired with 3D printed NACA 0012 section airfoils and the lower structural components were faired with airfoil shaped fairings made with mylar. The overall blockage area of the drive system is about 7%. The front of the drive system fairings were positioned $1.6D$ downstream of the rotor to minimize upstream effects of the drive system blockage area.

4.5.5 Body Centered Coordinate System

The local coordinate system used for the BOR in the experimental test is a right-handed, body oriented cylindrical system shown in figure 4.8a. The origin is centered on the BOR nose and the principal coordinates are described looking at the BOR nose from upstream. x is positive downstream along the body axis, r is always positive and radiates outward orthogonal to the x coordinate, and θ is referenced orthogonal to the x coordinate and in the same plane as the radial component. θ is positive clockwise when viewing the nose from upstream. The flow in the x direction, along the body axis, is referred to as the axial velocity and the associated turbulent fluctuations in that direction as the axial Reynolds stress or turbulence. To aid in discussion of the various parts of the flow the location of each measurement plane will be defined in the context of figure 4.8. The body centered coordinates are oriented such that $\theta = 180^o$ corresponds to the lee side. Conversely, the windward side occurs at $\theta = 0^o$ and the port and starboard sides of the body are at $\theta = 90^o$ and 270^o respectively.

4.5.6 Particle Image Velocimetry

Particle Image Velocimetry (PIV) was used to examine the velocity field at the aft end of the BOR. This setup gave three component velocity fields over a 160 x 160 mm^2 area with a 4.2 mm spatial resolution. The VTSWT was seeded by an MDG seeder that produces atomized Propylene Glycol particles on the order of one micron. The cameras used were Phantom v2512 high speed cameras with Nikon 200 mm lenses. The laser was a Photonics Industries DM laser with a maximum dual pulse rate of 12.848 kHz and a light sheet thickness of 2 mm. The PIV was taken at the maximum sampling rate of 12.848 kHz in dual frame mode to most accurately time resolve the flow. Timing and synchronization of the lasers, cameras,

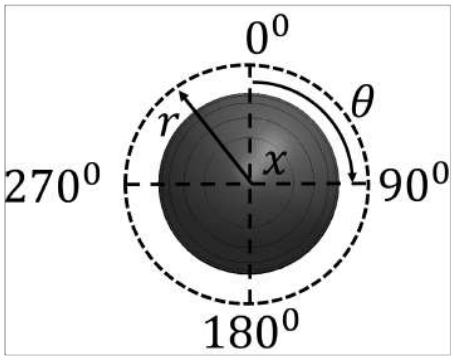

(a)

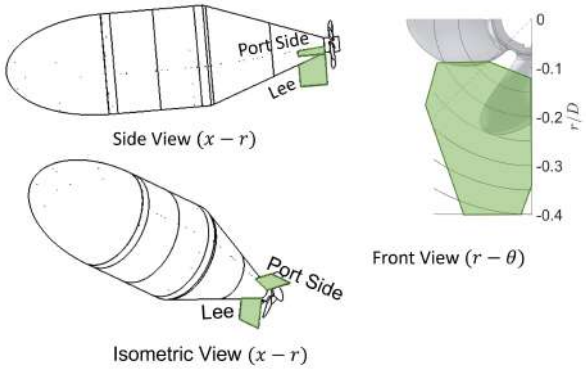

(b)

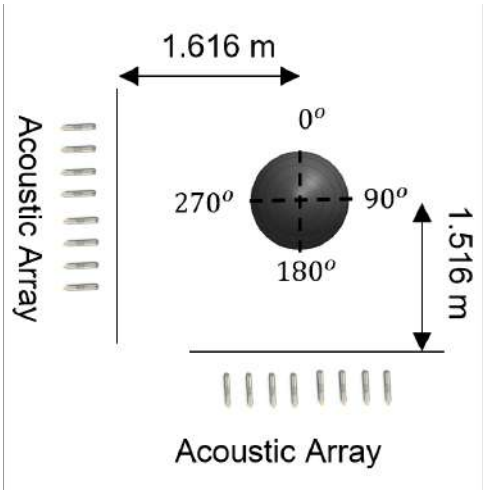

(c)

Figure 4.8: a) Body centered cylindrical coordinate system with the x coordinate positive axially downstream, r-coordinate positive normal to the body surface, and θ coordinate positive clockwise when viewed upstream of the nose. The axial coordinate x is perpendicular to the r-θ plane and the rotor rotates anti-clockwise in this frame of reference. b) Schematic showing the front, side, and isometric views of the location of the PIV measurements in the $x-r$ and r-θ plane. c) Schematic showing the relative location of the acoustic array for the two measurements.

and rotor trigger was coordinated using a Davis PTU X high speed timing unit. The PIV acquisition was triggered using an optical sensor. A mark was made on the shaft and once per rotation the optical sensor sent a signal to the timing unit and recording was done for that rotation at a sampling frequency of 12.848 kHz. This block of data is referred to as a cycle (1 cycle contains $f_s/\frac{N}{60}$ images) and yields a rotor phase discretization of between $\theta = 2.06^o$ and $\theta = 2.12^o$. The length of each measurement is determined by the memory capability of the Phantom v2512 cameras. Their maximum storage capacity was just over 24 000 images giving a measurement length of 1.87 s. This corresponds to between 144 and 168 rotations of the rotor depending on the advance ratio measured. Figure 4.9 shows the location of the laser light sheet, the camera viewing angles and the measurement plane on the port side of the body for the $x - r$ measurement on the port side. The laser light sheet is oriented parallel to the centerline axis of the body for the x-r plane measurements and orthogonal to the centerline axis for the r-θ plane measurements. The camera's locations are offset from the laser sheet orientation and a scheimpflug is used to adjust the focus plane of each camera. Three planes were measured; two in the $x - r$ plane and one in the r-θ plane. The first $x - r$ plane was taken in the lee of the body at $\theta = 180^o$ and the second on the port side of the body at $\theta = 90^o$. The r-θ plane was taken in the lee of the body and the data extended clockwise from $\theta = 180^o$ to $\theta = 250^o$. The view angle (α_c) between the cameras was approximately 80^o for all measurements. The lee side $x - r$ measurement has the same PIV setup as shown in figure 4.9 except the camera angles and laser sheet have been adjusted slightly to account for the change in location of the body when changing configurations. The r-θ measurement has the laser sheet parallel to the rotor rotation plane and located at the exit of the tail ramp ($x/D = 3.17$ in body oriented coordinates), the cameras are moved forward and face downstream. The locations of the $x - r$ and r-θ planes are illustrated in detail in figure 4.8b.

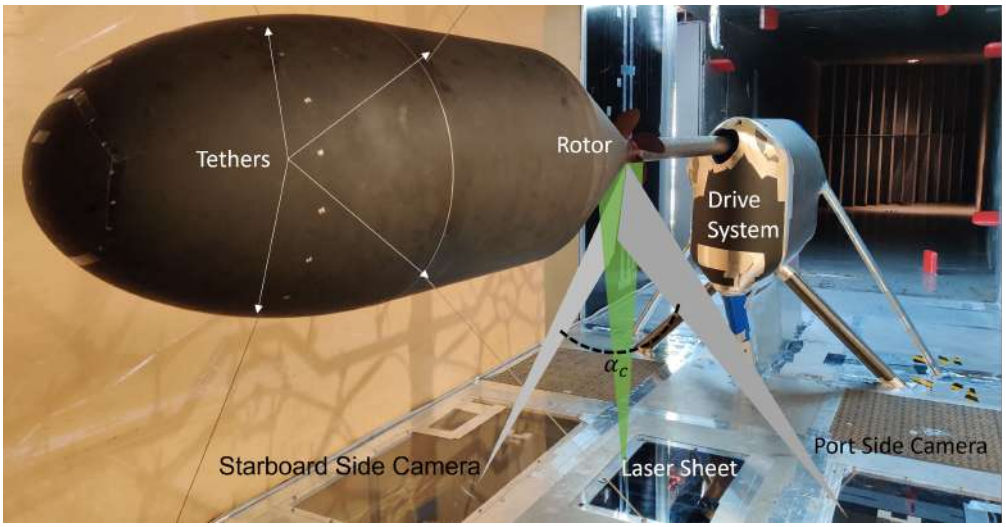

Figure 4.9: Experimental photo showing the location of the PIV measurement plane, the laser, and camera location setup for the port side PIV measurement. The view angle between cameras α_c is illustrated here.

Processing was done using LaVision Davis 10 and a multipass cross-correlation calculation. An initial pass was done on a 64×64 pixel^2 rectangular window with 75% overlap, four final passes were done using 32×32 pixel^2 rectangular window with 75% overlap. This yields a spatial resolution of 4 mm with a vector resolution of 1 mm. Examination of the velocity time history histograms in figure 4.10 revealed a number of outliers with sample sizes of between 1 and 10 velocity samples. To reduce the effect of spurious outliers such as these, Matlab post processing examined the velocity histograms of each point and defined a minimum band cutoff of 20 samples to remove significant outliers. The function divides the data into evenly spaced bins and groups the velocity distribution into each bin. For bins with values less than the minimum cutoff all points within the bin are removed from the data set. An example before and after of the histogram is shown in Figure 4.10.

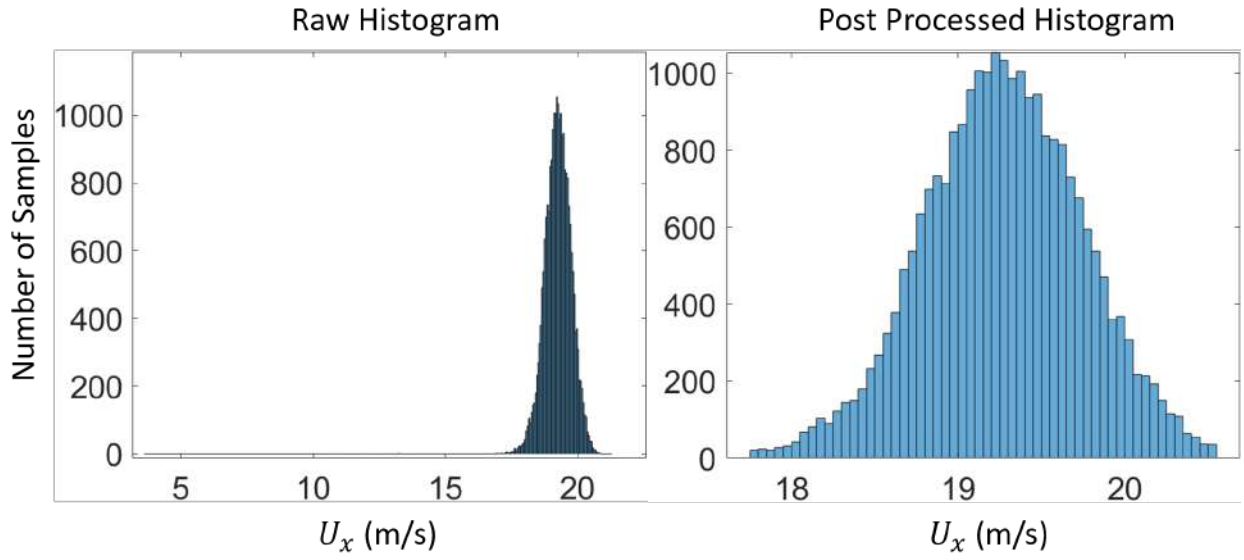

Figure 4.10: Histograms of the raw and post processed velocity data at $x/D = 3.17$ and $r/D = -0.25$ for the port side PIV measurement.The band cutoff value used was 20 samples.

4.5.7 Acoustic Measurements

A 251-channel microphone array located in the starboard chamber was used for all acoustic measurements. This array was designed by AVEC, Inc and contains 251 GRAS 40PH-S5 1/4" microphones in four interlocking spirals shown in Figure. 4.11b. They have a dynamic range of 32-135 dB(A) and a sensitivity of 50 mV/Pa. This array allows for beamforming of sources within the test section and provides single-point measurements of the far field sound radiated by the model for cases with sufficient signal-to-noise ratios. The acoustic data shown in this paper was beamformed using a sub-array of the second most downstream spiral, denoted Spiral 2 (highlighted in blue in figure 4.11b) and then integrated over the rotor to determine the acoustic spectra. All beamformed data use diagonal removal and were corrected for convection and refraction. An image of the array is shown in figure 4.11a. The center of the array given in the test section coordinates was measured to be $(X, Y, Z) = (0.555, 0.866, 1.616)$ m. From this location and the information in Table 4.1 the

(a)

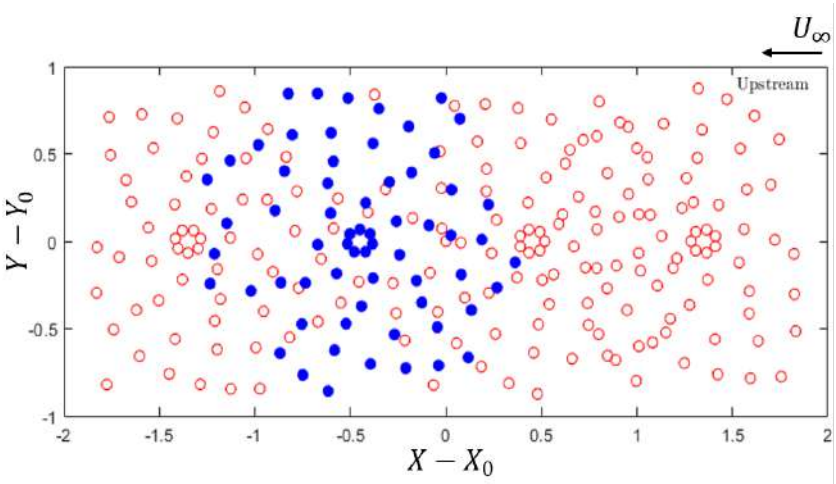

(b)

Figure 4.11: a) Image of the AVEC array from the starboard Kevlar chamber, b) 251 microphone array local coordinates, blue circles show Spiral 2. The center of the array in test section coordinates was measured to be $(X, Y, Z) = (0.555, 0.866, 1.616)$.

location of any of the microphones or individual spiral centers can be determined relative to the rotor location. Based on the two experimental configurations the array measured the sound radiated by the rotor on two planes, the first is on the lee side of the body at $\theta = 180^o$ and the second is on the starboard side at $\theta = 270^o$. These array locations are illustrated in figure 4.8c.

4.6 Results and Discussion

4.6.1 Mean Pressure

The mean pressure coefficient distribution over the body was measured along the length of the body at $\theta = 0^o$, and $\theta = 270^o$ as well as circumferentially on the nose of the body at $x/D = 0.5$. The axial distribution yields insight into the development of the flow over the length of the body and the circumferential distribution informs a consistent angle of attack was achieved for the inclined body measurements. The coefficient of pressure at $x/D = 0.5$ is negative on the body so the magnitude of the pressure coefficient was plotted in the circumferential data.

Figure 4.12a shows the axial pressure along the length of the body. The squares show the experimental measurements for the starboard side ($\theta = 270^o$), and the circles show the windward side ($\theta = 0^o$). Overlaid on top of each of the experimental measurements are RANS calculations performed by Drs. Meng Wang and Di Zhou at the University of Notre Dame (private communication Wang and Zhou [84]). The RANS results were used solely to provide some verification of the aerodynamic angle of attack of the BOR, based on pressure distribution comparisons. The dotted line shows the pressure coefficient distribution for the starboard side and the solid line shows it for the windward. At the nose ($x/D = 0$), the pressure coefficient nears one as this is close to the forward stagnation point. Due to the angle of attack this stagnation point is shifted away from the nose pressure probe and towards the windward side of the body. The flow then undergoes a favourable pressure gradient as it develops over the length of the nose cone. The favorable pressure gradient is greater for the starboard side of the body while the pressure appears to be similar between the two locations over the midbody. The boundary layer trip is evident in the discontinuity in the RANS solution but is not captured in the experimental measurements. A sharp decrease in

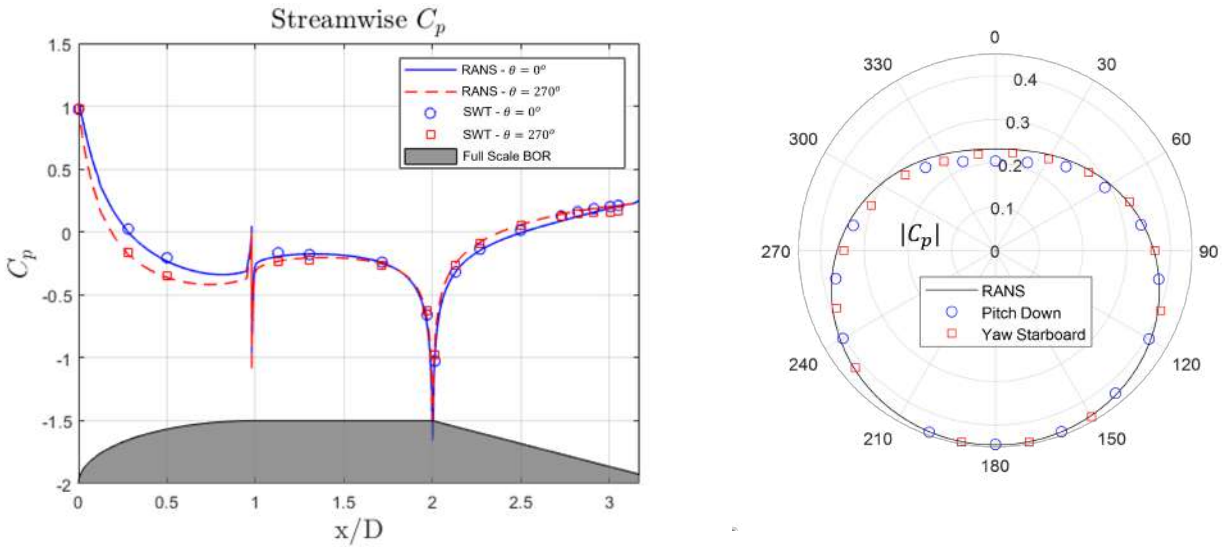

(a) (b)

Figure 4.12: Pressure coefficient distribution on the body of revolution with the rotor turned off a) shows the axial distribution with C_p on the y-axis, and axial distance on the x-axis, b) shows the magnitude of the circumferential distribution of the pressure for the body at angle of attack.

pressure occurs over the ramp edge at $x/D = 2.0$ before an adverse pressure gradient is seen over the length of the ramp. This adverse pressure gradient is stronger for the starboard side of the body ($\theta = 270^o$) than it is for the windward however the coefficient of pressure appears to be approximately the same as the flow approaches the rotor. Figure 4.12b shows the circumferential pressure distribution around the body at $x/D = 0.5$. This data was taken to confirm the consistency in the aerodynamic angle of attack between each experimental configuration. Therefore, to allow comparison between the two experimental configurations the yaw starboard case is rotated 90^o anticlockwise. The squares show the experimental measurements for the 5^o yaw starboard case, and the circles show the 5^o pitch down case. The RANS results are overlaid as a solid line.

For both cases on the leeward side of the body the C_p reaches a maximum of 0.44 before decaying monotonically to a minimum of 0.23 on the windward side. The close agreement

between the RANS results as well as both the 5^o pitch down and 5^o yaw starboard case indicates that the aerodynamic angle of attack matches $5^o \pm 0.2^o$ in both configurations.

With the confirmation of the body of revolution angle of attack in the two configurations, the following section will examine the three plane measurements of the flow in the context of the flow about the body.

4.6.2 Mean Flow About the Body of Revolution

Axial Planes on the Lee and Port Side

The particle image velocimetry data were used to compute and examine contours of the mean velocity and turbulence quantities for the 0^o and 5^o BOR. All plots are presented in body oriented coordinates with the body of revolution and rotor shown to scale. The contours presented in figure 4.13 show the mean velocity in the axial direction ($\overline{U_x}$), as defined in Section 4.5.2, for the nominally zero thrust condition corresponding to an advance ratio of $J = 1.44$. Figure 4.13a presents the mean axial velocity in the vicinity of the rotor for the 0^o angle of attack configuration, while figures 4.13b and 4.13c show the mean axial velocity for the lee side and port side of the body of revolution at 5^o angle of attack respectively.

Examining these three mean contour maps it can be seen that the gradient of $\overline{U_x}$ with r varies for each case. The velocity gradient variation is demonstrated in the figures by grouping of the contour lines, contour lines spaced further apart indicate a lower velocity gradient, whereas lines closer together indicate a higher velocity gradient. The results for the 0^o angle of attack at the rotor tail exit ($x/D = 3.17$) show a fairly monotonic gradient in r with a slight increase at 75% blade radius before reaching the freestream at $0.27D$. Figure 4.13b demonstrates a significantly lower initial velocity gradient than that seen in figures 4.13a and 4.13c however, away from the body the gradient increases before decreasing again near

the boundary layer edge. In comparison figure 4.13c reaches $0.1U_\infty$ at approximately $0.14D$ from the body surface at the rotor inlet plane. The variation in the velocity gradient in figure 4.13c shows a low variation with r near the surface, growing to a high velocity gradient at 0.15D, the velocity then rapidly approaches $0.8U_\infty$ at $0.24D$ before reaching the freestream below $r/D = 0.3D$. The significant variations in the velocity gradients evident in figures. 4.13b and 4.13c indicate the three dimensionality within the flow surrounding the body at angle of attack.

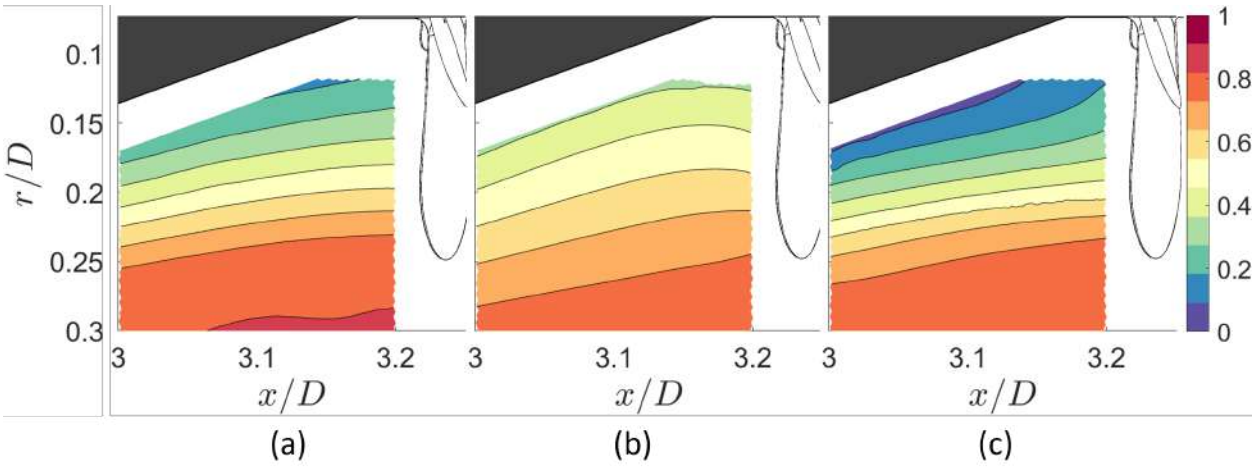

Figure 4.13: Contours of the mean velocity in the axial direction for the 0^o body of revolution configuration and at two locations for the 5^o angle of attack configuration at $J = 1.44$. a) 0^o angle of attack, b) 5^o angle of attack on the lee side ($\theta = 180^o$), c) 5^o angle of attack on the port side ($\theta = 90^o$).

Comparisons of the mean axial normal stress for the 0^o case and the 5^o case in figure 4.14 shows further evidence of the three dimensionality of the 5^o flow. The axial stress $\overline{u_x^2}/U_\infty^2$ is plotted for the 0^o case in figure 4.14a and for the 5^o case in figure 4.14b, and c. Some pixellation is noted in figure 4.14a due to some processing parameters in the PIV calculation. The normal stress is plotted as a contour with the levels determined by the turbulence levels. Balantrapu [14] showed the turbulence peaking around 0.4δ just downstream of the aft ramp corner before moving away from the body to 0.55δ at the rotor inlet plane as shown in

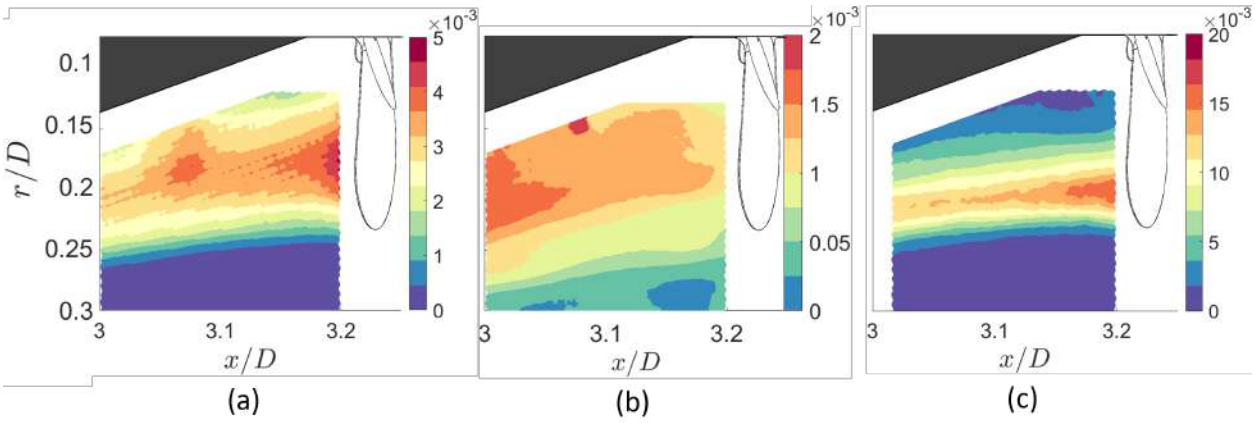

Figure 4.14: Contours of the average Reynolds normal stress in the axial direction normalized on the square of the freestream velocity($\overline{u_x^2}/U_\infty^2$) for a) 0^o angle of attack configuration, b) 5^o angle of attack on the lee side and c) 5^o angle of attack on the port side with the rotor inlet plane shown as dotted line.

figure 4.14a. The data presented in figure 4.14 shows that the turbulence form and intensity varies significantly when pitching the body to an angle of attack. The overall turbulence levels on the lee side, shown in figure 4.14b, are greatly diminished relative to the 0^o angle of attack case. Contrasting this the turbulence on the port side of the body, seen in figure 4.14c, is shown to have a peak that is approximately twice that of the 0^o case and more than quadruple that seen on the lee side. To understand the reasons for this turbulence variation recall the work of Ahn [2] described in Section 4.4 which demonstrated the three dimensional flow separation about a body of revolution at 5^o angle of attack. They showed that the flow begins separation on the windward side at a fairly high percentage of the overall length (0.8L at $Re_l = 4.2\text{x}10^6$) and this separation line sweeps up the side of the body until it reaches approximately 0.9L. The separation then rolls up into a pair of counter rotating axially aligned vortices on the lee side of the body. Admittedly this measurement was taken over a body with a slightly different shape and at a significantly higher length based Reynolds number than the flow shown in this paper, however, it seems probable that the separation mechanism and axial vortex formation is quite similar. Studies by Ashok and Smits [10] and

Ashok et al. [11] have further shown that the vortices are better defined at low angles of attack and low Reynolds number. With that in mind the turbulence along the port side is likely due to a three dimensional separation forming a shear layer that travels up the side of the body, from windward to leeward, and rolls up into a vortex before reattaching on the lee side. This would pull high momentum fluid off the body at the separation location and this is seen in the very high turbulence levels on the port side PIV measurement in figure 4.14c. The low turbulence levels seen on the lee side measurement can also be explained by this structure. The reattachment on the lee side brings with it high momentum, low turbulence freestream fluid that depresses the turbulent fluctuations in the outer portions of the boundary layer. To determine the existence and validity of this theory PIV results taken in the r-θ plane will be examined in the following section. The mean axial, circumferential, and radial components of the velocity will be discussed along with the in-plane streamlines and axial vorticity.

r-θ Plane on the Body Lee Side

The description of the flow from the previous section can be validated by examining the flow in an r-θ cut at the rotor inlet plane, $x/D = 3.17$. Figure 4.15 show the contours of the axial, radial, and circumferential velocities respectively. The rotor is shown to scale and the color scale of each component is shown to the left of the contours. In figure 4.15a, the axial ($\overline{U_x}$) velocity on the lee of the body ($\theta = 180^o$) shows evidence of the boundary layer close to the hub at around 10% of the free stream and growing in magnitude until it reaches the freestream velocity at an r/D of approximately 0.32. The gradient of the $\overline{U_x}$ velocity with r shows the non-axisymmetry of the flow. Were the flow axisymmetric, the contour lines should follow the radius lines drawn on the plots in black. However, the contour lines shown in this view of the flow trace a varying radius circle about the body

centerline. This is further evidenced when examining the radial component $\overline{U_r}$ in Figure 4.15b. It shows a strong velocity towards the rotor hub on the lee side, around $\theta = 180^o$. This velocity grows in strength as it moves closer to the body. Conversely, between $\theta = 225^o$ and $\theta = 250^o$ a radial velocity moving away from the body is evident. It should be noted before examination of the θ component of the velocity that in this coordinate system θ is positive clockwise. Examining figure 4.15b the $\overline{U_\theta}$ component is shown to have a minimum of around -10% of the freestream near the rotor tip at $\theta = 225^o$ and $r/D = 0.27$. The circumferential component is shown to increase closer to the body along the 225^o radial line where it reaches a maximum around 0.15D. To further understand the distribution of the radial and circumferential velocity components figure 4.15d should be examined. Figure 4.15d shows the contours of the magnitude of the axial vorticity with the in plane velocity vectors overlaid. There is a strong region of vorticity at $(r/D, \theta)$=$(0.17, 232^o)$ and the mean velocity vectors show an axially oriented vortex. The trends seen in the mean velocities can be explained by the existence of this vortex. It has a negative axial vorticity meaning it rotates anti-clockwise when viewing the rotor from upstream and this rotation is the source of the trends seen in the radial and circumferential velocity components. On the lee side the flow is rotated such that it is moving towards the hub, while further towards the starboard side the flow is moving away from the hub. In the same manner the maximum and minimum of the circumferential velocity components correspond to the portions of the vortex that are most tangent to the circumferential direction.

As theorized and discussed in Section 4.6.2 the vortex forms as a result of a separation region occurring on the port and starboard sides of the body and is likely mirrored on the port side. Furthermore this vortex is an important feature of the rotor near field as it is within the radius of the rotor and will therefore contribute to the sound produced. As each blade passes through $\theta = 232^o$ and $\theta = 128^o$ (the port side mirrored vortex) it will also cut the

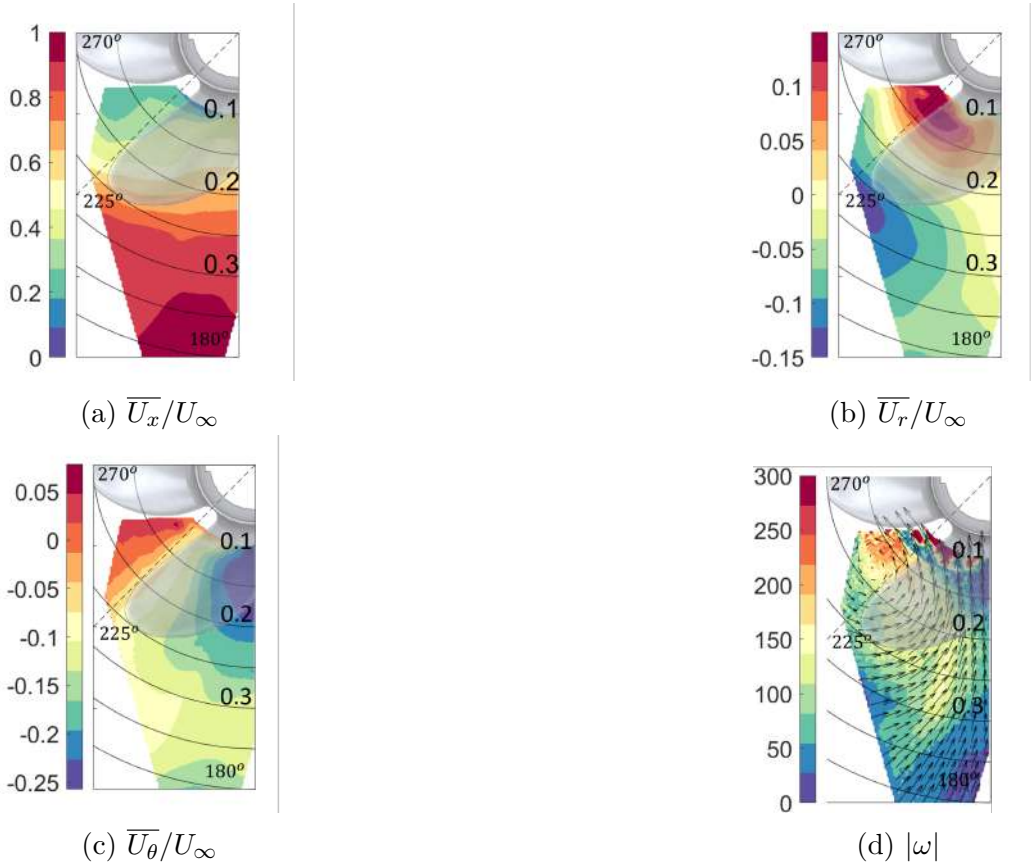

(a) $\overline{U_x}/U_\infty$ (b) $\overline{U_r}/U_\infty$

(c) $\overline{U_\theta}/U_\infty$ (d) $|\omega|$

Figure 4.15: Contours of the a) axial, b) radial, c) circumferential mean velocities, and d) the axial vorticity on the lee side of the rotor between $\theta = 180^o$ and $\theta = 250^o$. The rotor is shown to scale and the contour scales vary based on the value of each quantity.

counter rotating vortices. The blade passage through each vortex produces a periodically varying mean velocity that will radiate as tonal noise. There is also likely to be asymmetry in the production of sound from each vortex. The starboard side vortex vectors align with the rotation of the rotor near the tip while the port side vortex oppose it. This implies the lift variation near the tip as the rotor cuts the starboard vortex will be lower when compared to that of the port side vortex. The effects this will have on the acoustics is tonal, while the impact of the increased turbulence on the sides of the body will increase the broadband component of the sound. In other words, one significant result from inclining the body at an angle of attack is to increase the BPF peaks and haystacking intensity seen

in the sound spectra at low BPF multiples due to the formation of a separating shear layer and consequently the interaction of the vortices and turbulent regions with the rotor blades. Furthermore, as a result of the standing flow inhomogeneities there are likely to be directivity patterns associated with the interaction of the rotor with the vortices as well as the varying Reynolds stress levels.

The formation of the shear layer as well as the vortices seen in Figure 4.15d motivate the application of an embedded shear layer scaling (Schatzman and Thomas [78]) to charactarize the progression of the boundary layer profiles from upstream to downstream. This analysis is presented in the following section.

4.6.3 Embedded Shear Layer Scaling

Schatzman and Thomas [78] introduced a scaling for two dimensional shear layer flows under significant adverse pressure gradient. They posited that a significant inflectional instability near the peak streamwise Reynolds stress produced an embedded shear layer (ESL), and that by applying scaling associated with the instability the profiles should show similarity. The length and velocity scales used in this scaling are the vorticity thickness and local velocity defect. Balantrapu et al. [15] applied the embedded shear layer scaling to profiles along the body of revolution tail at 0^o angle of attack. In their analysis Balantrapu et al. [15] found excellent collapse of the mean profiles, however the streamwise turbulence profiles only showed collapse within 0.02 u_s^2/U_d^2 up to about one diameter upstream of the tail. While there some evidence that ESL scaling was successful, most notably that the shear layer length and velocity scales were proportional to the boundary layer thickness and edge velocity respectively, Balantrapu et al. [15] questioned the effectiveness of the ESL scaling in collapsing the turbulence profiles. In fact Balantrapu et al. [15] concluded that a

more successful turbulence profile collapse came through a $U_e - \delta_1$ scaling where δ_1 is the displacement thickness defined as the integral over the boundary layer of the velocity defect with respect to distance from the wall.

The usefulness of the embedded shear layer scaling is that it places the mean velocity profiles in context with the gradient at the inflection point. Turbulence generation within a boundary layer under significant adverse pressure gradient can be due to inflectional instabilities and normalizing with respect to inflection point variables allows examination of the profiles with that framing in mind. The vorticity thickness is defined as the ratio of the velocity defect at the inflection point to the velocity gradient with respect to distance from the wall, evaluated at the inflection point. This is represented by the following,

$$\delta_\omega(x,t) = \frac{U_d}{(d\overline{U}/dr)_{IP}} \tag{4.6}$$

The velocity defect is defined as the difference between the edge velocity and the mean velocity at the inflection point,

$$U_d = U_e - \overline{U_{IP}} \tag{4.7}$$

The distance from the surface is centered on the inflection point and given the term η such that $\eta = 0$ corresponds to the location of the inflection point within the profile. The similarity variables are defined as,

$$\eta = \frac{r - r_{IP}}{\delta_\omega}, U^* = \frac{U_e - \overline{U}}{U_d} \tag{4.8}$$

The profiles analyzed lay within the overlap of the available PIV (5^o case) and hotwire anemometer measurements (0^o case). This corresponded to three locations ($x/D = 3.01, 3.09,$ and 3.17) and three profiles are presented for each quantity in the following data.

Determining the Location of the Inflection Point

The inflection point was defined using two methodologies. For the 0^o case, the inflection point was located within a few percent of the peak axial Reynolds normal stress so the location of the inflection point was selected to be the maximum value of the axial Reynolds stress. For the 5^o case the peak Reynolds normal stress was not aligned with the inflection point so a 7th order polynomial function was fit to the experimental data using a least squares fit. The first and second derivatives were then taken numerically and the zero crossing of the second derivative was selected as the location of the inflection point in the mean velocity profile.

Mean Velocity and Turbulence Profiles

To begin the mean velocity and turbulence profiles at two circumferential locations about the body at 5^o angle of attack are described. These planes are located at $\theta = 90^o$ corresponding to the port side of the body and $\theta = 180^o$ corresponding to the lee of the body. The profiles for these two planes as well as a plane taken for the 0^o angle of attack case at three axial locations are shown in figure 4.16. The mean velocity profiles on the port side and for the 0^o angle of attack body show readily distinguishable boundary layer inflection points while the profiles on the lee side of the body appear more linear. Comparisons of the turbulence profiles show a significant decrease in turbulence levels in the lee of the body with increased levels for both the 0^o angle of attack profiles and the profiles on the port side. While the turbulence on the port side of the body at angle of attack is similar to the 0^o body in terms of turbulence levels and peak turbulence location, it is elevated and more peaky in nature.

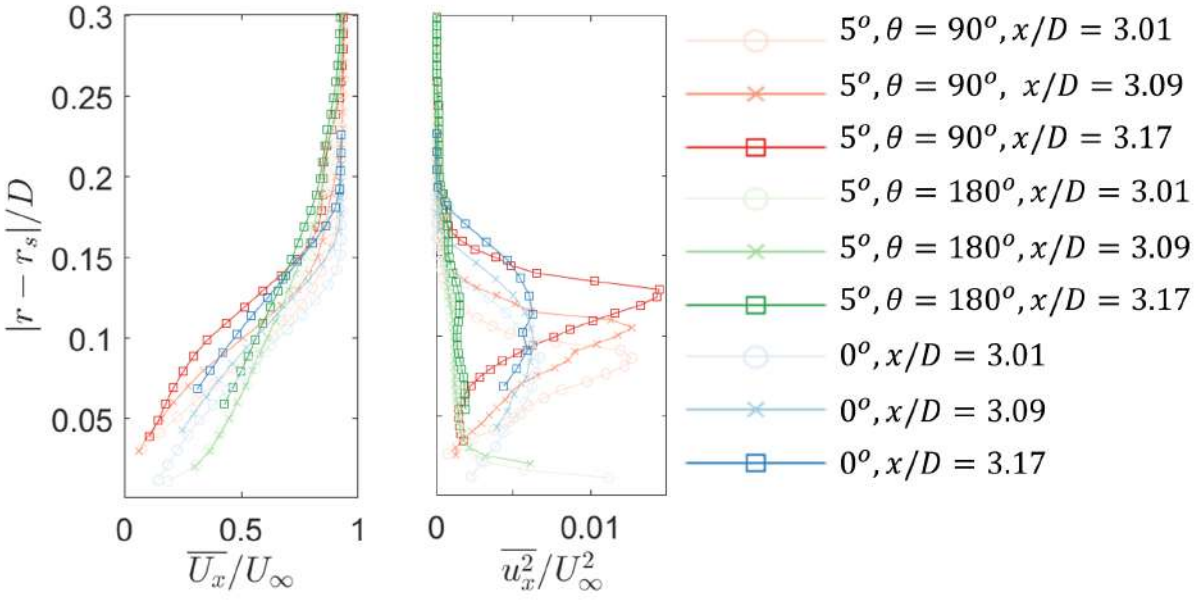

Figure 4.16: An axially aligned downstream progression of the mean velocity (left) and axial turbulence (right) profiles of the 0^o angle of attack (blue) and the 5^o angle of attack at $\theta = 270^o$ (red) and at $\theta = 180^o$ (green) planes are shown here. The most upstream profiles ($x/D = 3.01$) for each body location are shown with circles, followed by x's ($x/D = 3.09$), with the most downstream location shown with squares ($x/D = 3.17$).

Applying the Embedded Shear Layer Scaling

The embedded shear layer scaling has been applied to the mean velocity, axial turbulence, and shear stress in figure 4.17. Beginning with the mean velocity it is clear that this scaling collapses the mean profiles to the error function with deviations from the error function beginning one vorticity thickness beneath the inflection point. The axial turbulence for the body at angle of attack show some dependencies on axial position. As the flow moves downstream, the turbulence levels relative to the velocity defect are seen to increase for both the lee and port sides. This dependency is exaggerated for the port side. For the 0^o body there is no axial dependency and the profiles are arbitrarily distributed in terms of turbulence intensity. This suggests that there is no relationship between increasing pressure

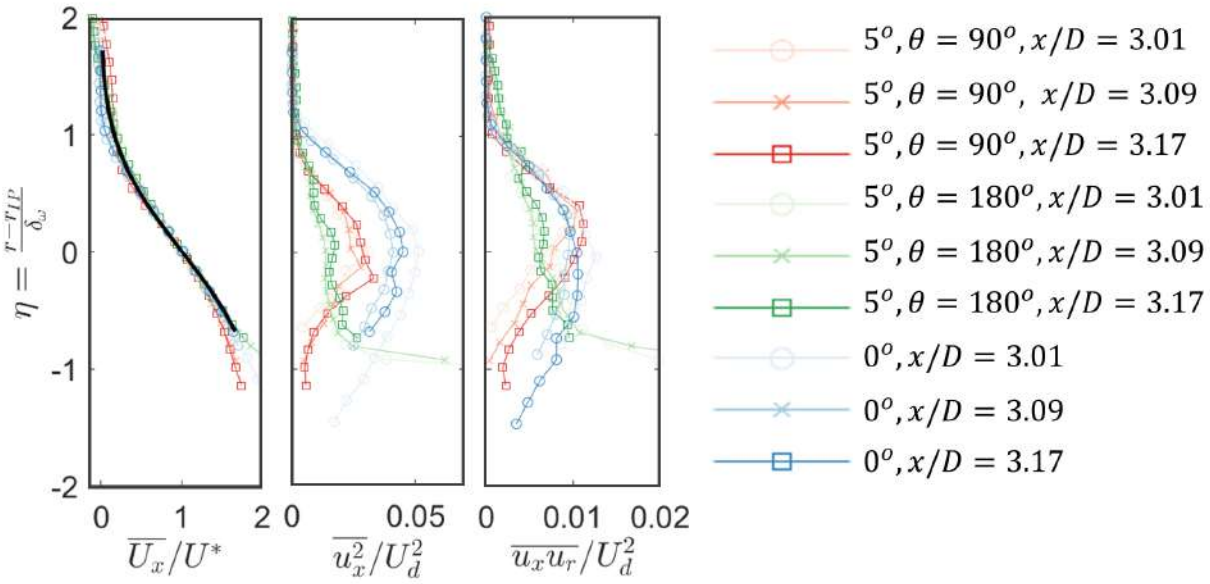

Figure 4.17: An axially aligned downstream progression of the mean velocity (left), axial turbulence (center), and shear stress (right) profiles scaled on the vorticity thickness and velocity defect at the inflection point. The 0^o angle of attack (blue) and the 5^o angle of attack at $\theta = 90^o$ (red) and at $\theta = 180^o$ (green) planes are shown here. The most upstream profiles ($x/D = 3.01$) for each body location are shown with circles, followed by x's ($x/D = 3.09$), with the most downstream location shown with squares ($x/D = 3.17$). The error function 1-erf(η) is plotted in black.

gradient and the ratio of the turbulence to the velocity defect for the 0^o body. Similarly for the shear stress of the 0^o body there is no axially aligned dependence on the turbulence levels. These profiles also exhibit less collapse beneath the boundary layer inflection point than that seen above it.

Interestingly, when scaled on the velocity defect rather than the freestream velocity, the profiles for the lee side of the body look more similar to the 0^o and port side profiles. This suggests that, while the overall turbulence is significantly depressed on the lee side of the body, its ratio to the velocity defect is of similar magnitude to the other profiles. Furthermore, beneath the inflection point, while the port side profiles decay to zero in much the same way as the 0^o body, the lee side profiles surpass that of the port side profiles.

Extending the analysis of the velocity profiles, the following section will now take the conditionally averaged profiles at the rotor inlet plane and examine the phase dependent effects of the rotor on the axial velocity and turbulence.

4.6.4 Phase Averaged Profiles

Phase averaged statistics can be computed from the PIV data sets by averaging over all cycles at each image. The PIV for the lee side $J = 1.44$ measurement consisted of 172 images at different blade phases repeated 131 times. This gives 172 positions, or phases, of the rotor with 131 samples of each phase. These samples were averaged to find a phase average that was a function of the blade position for one blade passage. For the lee side plane, there are 35 images between each blade passage indicating each phase corresponds to a rotation angle of $\phi = 2.06°$. For the port side plane $J = 1.44$ measurement, the data set consisted of 168 images repeated 147 times. There are 34 images between each blade passage indicating each phase corresponds to a rotation angle of $\phi = 2.12°$. Radial profiles at $x/D = 3.17$ of the mean velocity and Reynolds normal stress as a function of the blade position ϕ, or phase, were extracted from the time resolved PIV for the lee and port side planes. Figures. 4.18a and 4.18c show the average fluid velocity seen by each phase of the rotor blade as it moves past the PIV measurement plane. Any structures or variation within the flow occur at the same blade position in every image and will appear as phase correlated features. The effect of the rotor is seen in the bulging of the mean profiles at $\phi = 18^o$ in figure 4.18a and 4.18c. The rotor blade accelerates the flow at each blade passage so a local acceleration of the flow is seen as the blade passes, this corresponds to the flat sections within the radial profile plots. The bulging lobes in the blade phase averaged velocity profiles are phases with relatively slower velocities when compared to the flat sections. They occur between blade passages and show the absence of the rotor blade at that position of the rotation. The rotor

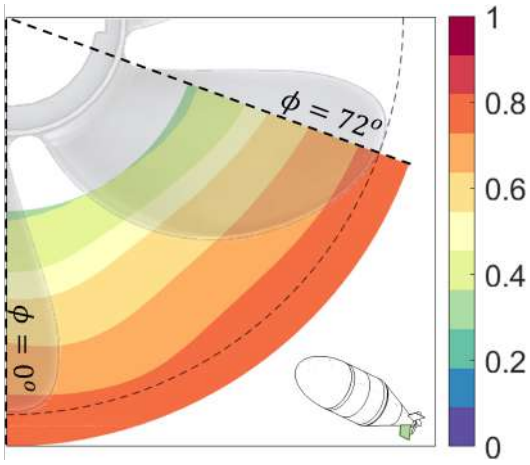

(a) $\langle U_x \rangle / U_\infty$ in the lee of the body ($\theta = 180^o$)

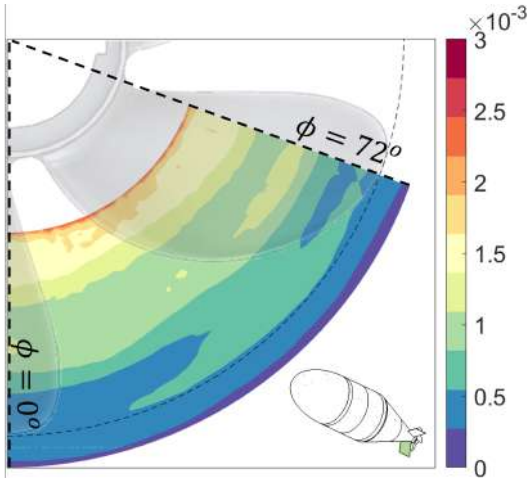

(b) $\langle u_x^2 \rangle / U_\infty$ in the lee of the body ($\theta = 180^o$)

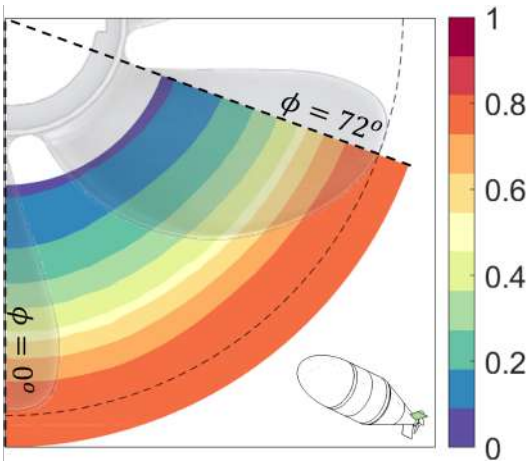

(c) $\langle U_x \rangle / U_\infty$ on the body port side ($\theta = 90^o$)

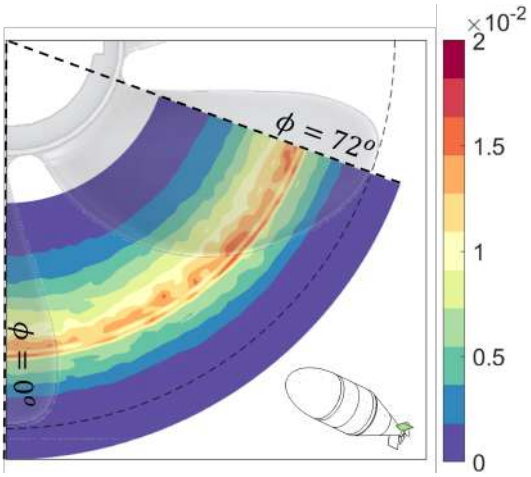

(d) $\langle u_x^2 \rangle / U_\infty$ on the body port side ($\theta = 90^o$)

Figure 4.18: Contours of the blade phase averaged radial profiles of the mean velocity in the axial direction and the axial Reynolds normal stress at the rotor inlet ($x/D = 3.17$) for two locations about the body at an advance ratio of $J = 1.44$. The figure on the bottom right shows the location of the measurement profile for each plot. a) lee side mean velocity, b) lee side Reynolds normal stress, c) port side mean velocity, d) port side Reynolds normal stress. The rotor blade position is shown overlaid over the data and the dotted line shows the rotor diameter.

passage effect is more prominent in the mean velocities lee side when compared to the port side. This can be explained by examining the overall turbulent energy within the flow at the rotor inlet for the two circumferential locations. The maximum $\overline{u_x^2}/U_\infty^2$ within the flow for the lee side is on the order of $2\text{x}10^{-3}$, whereas for the port side it is on the order of $1.5\text{x}10^{-2}$, almost an order of magnitude difference. The rotor is designed to have zero thrust at $J = 1.44$ so we should expect minimal flow acceleration effects at this condition. However the low energy plane on the lee side ($\theta = 180^o$) results in a piece of the flow in which the rotor has a non-zero thrust and we see significant rotor effects in both the mean flow and the turbulence.

The phase averaged turbulence stress contours show both expected and unexpected features. For the port side plane, figure 4.18d, the contour map reveals what appears to be a shear layer with features that appear statistically almost identical regardless of blade phase. Surprisingly this is not true for the measurements made on the lee side (figure 4.18b) the contours show the much thicker, weaker, turbulent region revealed in the mean profiles, but we see that the thickness of this region varies with blade phase, resulting in the same bulging seen in the phase averaged mean velocities (see the red region within figure 4.18b). There is further variation with blade phase near the tip of the rotor that shows a higher Reynolds normal stress for a portion of the blade phase between $\phi = 33^o$ and $\phi = 55^o$. While the phase averaged structure of the turbulence has certain rotor noise implications, the greater impact on the form of the acoustic spectra as well as on the noise prediction schemes comes from the correlation structure of the flow. In an effort to understand how the correlation structure within this flow is altered by the three dimensionality of the body of revolution at angle of attack the two point correlation function at various points in the rotor plane and upstream were investigated.

4.6.5 Two Point Correlations at Various Points in the Boundary Layer

As discussed in Section 4.4 the form of the two point correlation function is an important piece necessary for accurate time-domain sound predictions. Thus examining how the correlation function is distorted as it convects towards the rotor as well as what it looks like as it is ingested is critical to understand. To that end the correlation function at $\theta = 180^o$ and 90^o for the three profiles analysed in Section 4.6.3 was plotted for three body normal locations. The correlation function was calculated by taking the time averaged value of the correlation between the axial velocity at one point, referred to as the anchor point, and every other point in the two dimensional measurement plane. This mathematical procedure is given by equation 4.9 below

$$\rho_{u_x u_x}(x, r) = \frac{\langle u_x(x, r) u_x(x', r') \rangle}{\sqrt{\langle u_x^2(x, r) \rangle \langle u_x^2(x', r') \rangle}} \tag{4.9}$$

where (x, r) is the anchor point, and (x', r') is the reference point. Figures 4.19 and 4.20 plot this quantity at a number of anchor points. Figure 4.19 is organized with the lee side data shown in 4.19a and the port side data shown in 4.19b. Each plot in 4.19 shows the correlation coefficient function for an anchor point at three streamwise locations, x/D =3.01, 3.09, and 3.17 for three distances from the body surface. The first corresponded to the rotor tip located at $r/D = 0.25$, the second was located at the inflection point for each profile, and the third was located 0.02D above the inflection point. Figure 4.20 shows the same correlation coefficient function in r-θ space for 14 anchor points. Equation 4.1 shows the impact the shape of the correlation function has on the noise spectra, a stretched correlation function will result in larger length scales and greater blade to blade force correlations which acts to narrow and increase the peak level of the haystacking evident in the sound spectra. The maximum

turbulence intensity within the boundary layer impacts the overall broadband levels of the spectra. Examining figures 4.19a and 4.19b some conclusions of the effects of the different correlation functions may be drawn. Firstly from figure 4.19a the correlation function is significantly stretched in the axial direction. The angle of the major axis to the body surface becomes greater as the anchor points approach the rotor and the pressure gradient increases. This rotation also appears to be function of the distance from the body surface and as the anchor moves away from the surface the clockwise rotation of the correlation function increases. The effect that the stretched correlation function will likely have on the sound is to increase the height and narrow the width of the haystacks. In contrast to this the correlation function seen in figure 4.19b shows less rotation and less elongation in both the axial and body normal directions. The correlation function is more isotropic, or less stretched, and has a narrower peak than the turbulence within the $\theta = 180^o$ plane. The shape of the correlation function alone should dictate that the sound produced as the rotor passes through the lee side of the body will act to increase the haystacking effect. However there is another factor at play here, namely the upwash turbulence intensity. In this data this is approximated by the $\overline{u_x^2}$ turbulence component (seen in figure 4.19a and 4.19b as a black line). As discussed previously it is this peak intensity that is the primary driver of the overall broadband level of the data. The correlation function dependence on circumferential location adds further insight into the shape of the three dimensional correlation function. Figure 4.20 shows the correlation function at a number of r-θ anchor points and illustrates the shape of the correlation function in r-θ space, just upstream of the rotor. It is apparent from this figure that the correlation function is isotropic in r-θ for much of the rotor blade positions.

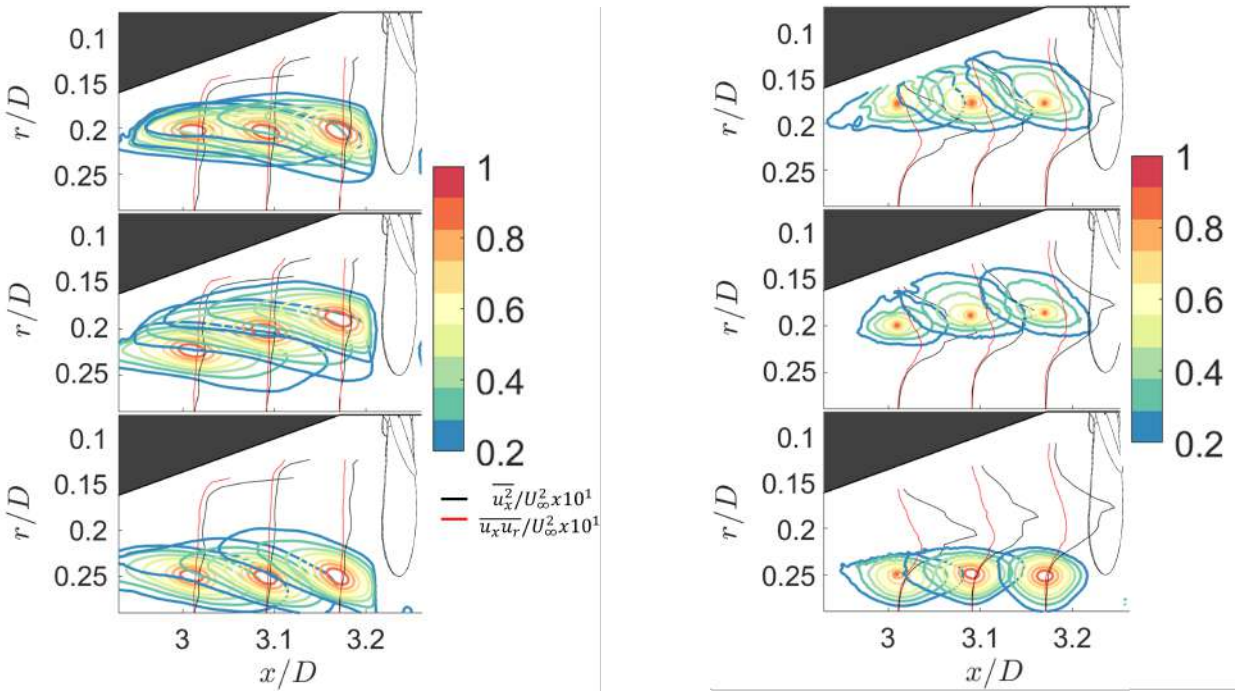

(a) (b)

Figure 4.19: Contours of the two point correlation coefficient function for the axial fluctuating component of the turbulence. The turbulence profiles for the axial fluctuating component ($\overline{u_x^2}$) is shown in black while the shear stress ($\overline{u_x u_r}$) is shown in red. The turbulence profile data are normalized on U_∞^2 and scaled by 10^1 to be clearly visible on the plot. The correlation function is normalized on the variance such that a maximum correlation value of 1 occurs at the anchor point. These data are shown for 2 plane locations;a) $\theta = 180^o$,b) $\theta = 90^o$.

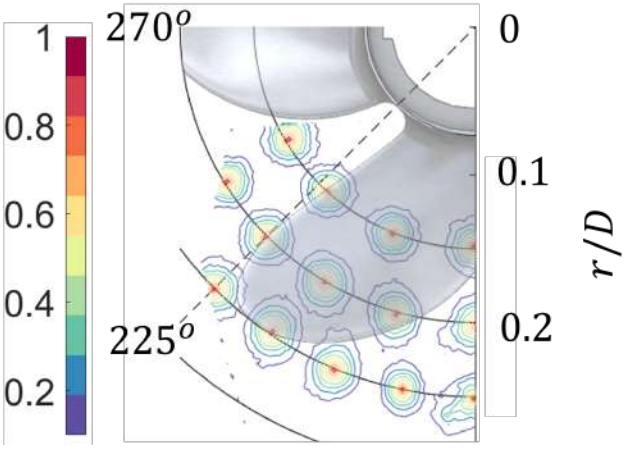

Figure 4.20: Contours of the two point correlation coefficient function for the axial fluctuating component of the turbulence. The correlation function is normalized on the variance such that a maximum correlation value of 1 occurs at the anchor point. These data are shown for the r-θ plane.

4.6.6 Noise Impacts

Much of the data presented in the previous sections are different ways of viewing the correlation function of the turbulence, R_{ij}, which is the main driver of the noise radiated by the rotor. As a means of confirming the impact of the flow on the acoustics, integrated acoustic spectra for the zero thrust advance ratio of $J = 1.44$ are taken at Spiral 2 of the acoustic array.

For the two array locations tested there are interesting effects on the radiated noise resulting from the changes in array measurement directivity. Recall figure 4.8c in which the array is shown to be in two directivity planes. The first images the acoustics on the lee side of the body and the second on the starboard side. This change in directivity has a significant effect on the radiated acoustics. The data presented here is an integration of beamformed maps calculated using conventional delay and sum beamforming and the integration region is shown in figure 4.21. All microphone data used diagonal removal and were corrected for convection and refraction. The acoustic spectra shown in figure 4.24 on the vertical axis are

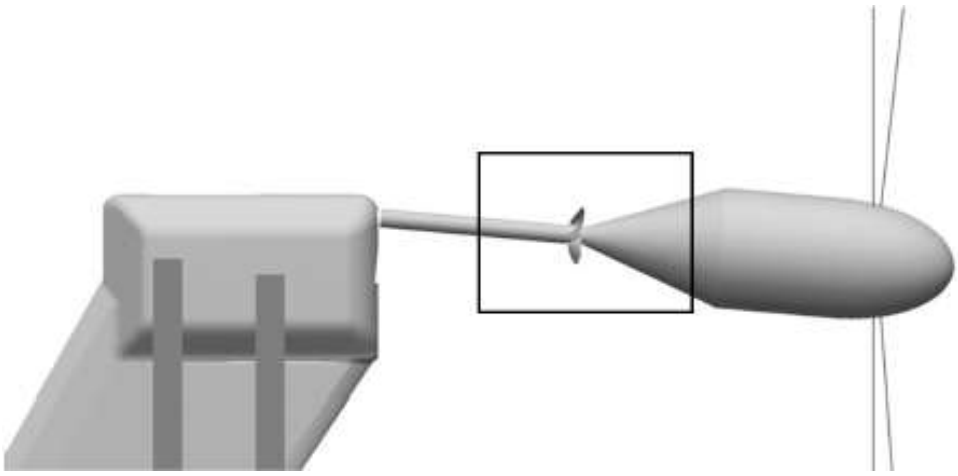

Figure 4.21: CAD of the BOR assembly showing the location of the integrated region for the integrated acoustic spectra.

corrected for freestream and rotor rotation using the following correction factor,

$$SPL = 20log_{10}\left(\frac{p_{rms}}{p_{ref}}\right) + 10log_{10}\left(\frac{c^5}{U_\infty^2\left(\sqrt{U_\infty^2 + (\omega r)^2}\right)^3}\right) \tag{4.10}$$

Keeping the Reynolds number constant means increasing the flow speed for higher temperatures because the air viscosity is dependent on the temperature in the air flow. So, in order to maintain the same advance ratios, the rotor speed was increased when the temperature increased. In order to make comparisons between measurements taken at the same advance ratio and different temperatures, a small adjustment in dB is required. Noise from airfoils scales approximately on U^3, where U is the chord parallel inflow velocity. A rotor blade is effectively a rotating airfoil so normalizing the SPL on the cube of the blade inflow velocity is done. Accounting for the rotation of the blade and normalizing on the speed of sound the resultant magnitude of the velocity is given by, $\sqrt{U_\infty^2 + (r\omega)^2}$. Accounting for the freestream is done by adding an additional U^2 scaling normalized on the speed of sound. The horizontal axis is normalized on the rotor blade passage frequency. The solid curve shows data from

the 0^o angle of attack case (see further results in Hickling et al. [48]), the dotted curve shows results from the starboard side array, and the dash dotted line shows results from the lee side array. In previous sections it was suggested that the impact of the increased turbulence on the side of the body and the vortices in the lee of the body would be to increase the OASPL as well as increase the peak of the haystacking and introduce tonal components in the spectra. Comparing the 0^o angle of attack to the starboard measurements it is evident that the noise is generally within 1 dB for both cases. However, examining the lee side measurement shows about a 5 dB elevation over those measured at both 0^o and on the starboard side. There is no evidence of tones in the acoustic spectra suggesting two things; firstly that the vortices are not strong enough for the rotor to radiate tonal noise during its interaction with them, and secondly that the turbulence ingestion noise is dominant for this case. Furthermore there is an increase in the haystack peak about the first and second harmonic for the lee side measurement. This can be understood by examining figure 4.23; the different array location results in the rotor being physically closer to the array as well as changing the location of the highest turbulence region with respect to the measurement plane. Radiated noise decays approximately on the order of r^2, where r is the distance from the source to the observer. The change in r from the centre of array Spiral 2 to the rotor disc centre is $1.91 - 1.84 = 0.07$ m and the resultant noise decay is around 0.33 dB. This obviously does little to explain the difference of 5 dB seen in the spectra, so now the change in the turbulence and rotor directivity should be examined. The flat of the rotor blade is most acoustically visible when the blade is moving away from the array in each view so the primary contribution to the noise will come from the turbulence encountered by the rotor blade at that location. For the starboard array that corresponds to the lee of the body which is a region of low turbulence flow drawn in by the vortex. Whereas for the lee array that corresponds to the location of the highly turbulent shear layer and separation vortex. As discussed in Section 4.6.2 the separation vortex sheet sweeps up the side of the body and it

is the interaction of the rotor with this high turbulence and vorticity structure on the port and starboard sides of the body that leads to an increase in the noise radiated towards the lee side array.

Furthermore there is a tangential lift component at the tip of the blade resulting from the blade drag that has its own associated dipole distribution. This force vector is illustrated in figure 4.22 where v_r is the relative velocity the blade section sees as it rotates, α is the angle of attack of the blade, β is the blade pitch, F_l is the chord normal force (lift), and F_t is the chord parallel tangential force (drag). As the blade cuts through the embedded shear layer on the port and starboard sides of the body the tangential force vector is pointing towards and away from the array. The large fluctuations in the embedded shear layer then cause a fluctuation in the force radiated towards the array at these locations. This serves to further increase the sound radiated towards the lee side of the body.

To demonstrate the impact of the radial forces of the rotor on the noise increase observed at this microphone location the direction of the force vector should be considered. Anderson et al. [8] demonstrated that at low blade passage frequencies (between 1 and 3 multiples of the BPF) the uncorrelated radial force on the blades had a significant effect on the noise at similar directivity angles to those measured in this experiment. Figure 4.23a and 4.23b show the direction of the radial force vector for each point in the rotation of the rotor from the point of view of the microphone spiral at which the spectra were computed from. It is clear that the point at which the radial force vector is pointing towards and away from the array on the lee side is coincident with the interaction of the rotor blade with the embedded shear layer. Figure 4.16 shows the increase in u_x^2 between the 0^0 angle of attack case and the port side 5^0 angle of attack case to be approximately 3x at the center of the shear layer. If it is assumed the sound increase is mostly due to the turbulent fluctuation increase then in dB this corresponds to $10\log_{10}(u_{x_5}^2/u_{x_0}^2) = 10\log_{10}(3) = 4.7dB$.

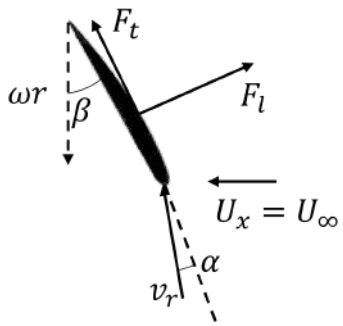

Figure 4.22: Blade force diagram showing the resultant angle of attack, lift, and tangential forces. Rotor rotation is down the page and flow is from right to left.

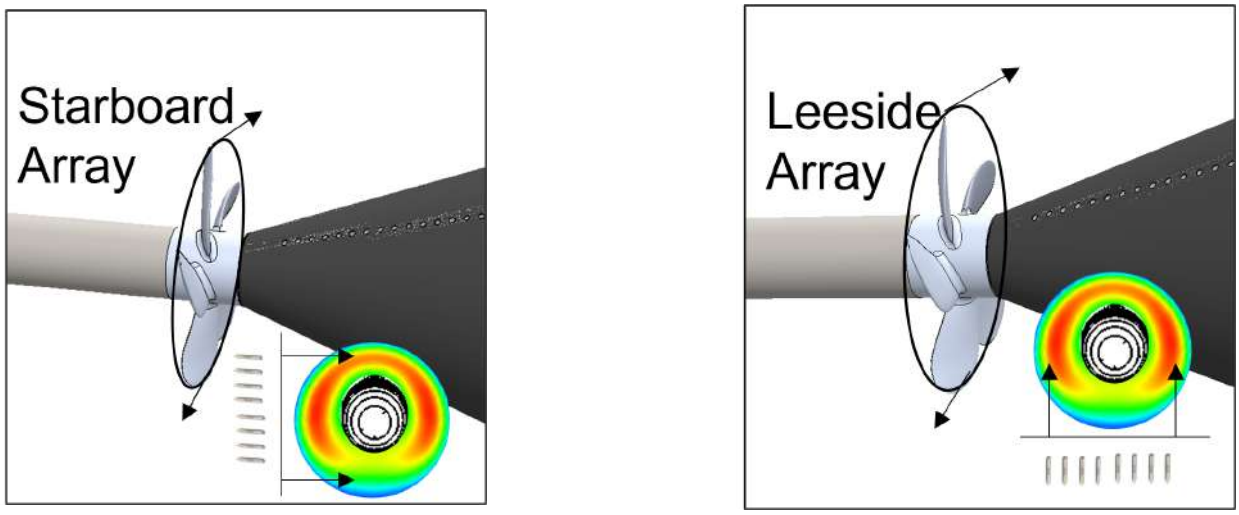

(a) (b)

Figure 4.23: Acoustic view of the rotor in the 2 configurations a) shows the view of the rotor from the starboard array as seen from the center of microphone spiral 2. b) shows the view of the rotor from the lee array as seen from the center of microphone spiral 2. RANS results of the Reynolds normal stress from private communication with UND (Wang and Zhou [84]) are shown to illustrate the distribution of the Reynolds stress intensity around the body.

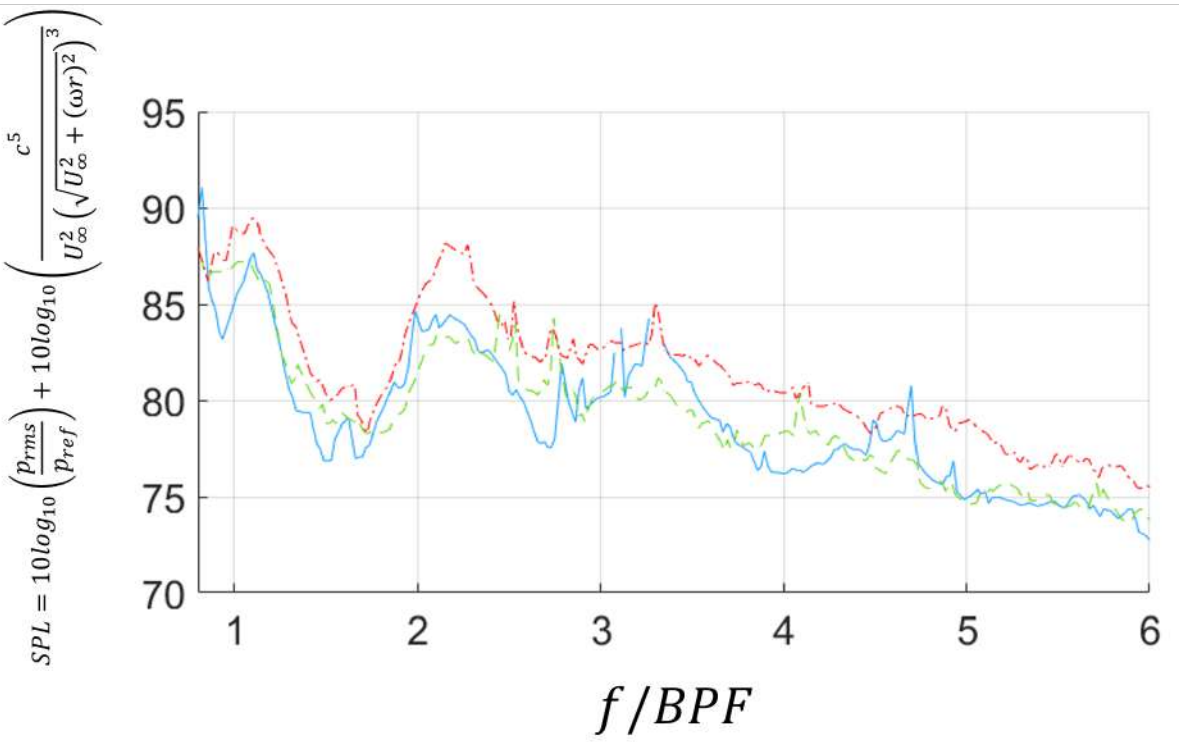

Figure 4.24: Acoustic spectra for J=1.44. The solid (blue) line is the 0°angle of attack case, the dotted (green) line is the starboard side measurement, and the dash-dotted (red) line is the lee side measurement.

4.7 Conclusion

Measurements of a rotor ingesting the wake of a body of revolution inclined at 0^o and 5^o angles of attack were made. The axial and circumferential mean pressure distribution was shown to match the RANS calculations of the inclined body, indicating the aerodynamic angle of attack was within 0.2^o of 5^o. Significant differences in the mean flow on the lee and port side were noted. Most significantly there was evidence of an embedded shear layer on the port side that significantly increased the turbulence levels seen relative to those on the lee side. Circumferential flow measurements at the rotor inlet then showed the existence of a vortical structure between the lee and starboard side of the body. The effect of pitching the body at an angle of attack was therefore determined to cause the formation of a three dimensional separation shear layer that rolls up into a pair of counter rotating vortices near the lee of the body. The interaction between the rotor and these vortices introduces significant blade to blade correlation as the vortex is both within the rotor disc, and near the tip. As such the blade velocity as it moves through each vortex is significant for sound production and is correlated between blade passages. Both of these observations imply an increase in magnitude and narrowing of the haystacking peaks. The spectra of the radiated sound at two directivity planes confirmed this and also introduced directivity effects as a result of the varying turbulence and flow structures encountered by each blade. An embedded shear layer scaling was applied to the mean velocity, axial turbulence, and shear stress profiles at various points on the body. Notably, while a physical embedded shear layer is noted in the u_x^2 contours for the port side PIV, the embedded shear layer scaling did not effectively collapse the axial turbulence and shear stress profiles in the axial direction. However it did provide insight into the boundary layer characteristics. There appeared to be an axial dependence on the axial turbulence and shear stress where the ratio of the turbulence to the velocity defect increased with downstream position below the boundary layer inflection point.

Phase averaged radial profiles for the pitched body on the port and lee side at $x/D = 3.17$ were shown for the zero thrust condition and evidence of rotor effects were seen in the mean velocity in both cases. The turbulence in the lee of the body also exhibited rotor effects in the turbulence however no phase variation was noted on the port side measurements. Examining the two point correlation function shows significant modification of the turbulence as it is convected along the pressure gradient on both sides of the pitched body. Stretching in the axial direction is noted for the lee side turbulence while the port side remains fairly isotropic. The shape of the correlation function is also far more peaked on the port side than on the lee side meaning the correlations decay more rapidly in this region. The effect this will likely have on the acoustics is to narrow and sharpen the haystacks surrounding the blade passage frequency as well as increase the overall broadband levels of the sound due to the increased turbulence on the sides of the body. Measurements of the correlation function within the rotor plane show it is isotropic in r-θ space for a significant portion of the circumference.

Chapter 5

Compact Eddy Structure of Turbulence Aft of an Inclined Slender Body

5.1 Context

Turbulence anisotropy results in distortion of the streamwise and transverse length scales and affects the effectiveness of the homogeneous turbulence assumption. This paper seeks to quantify the extent to which the upwash correlation function is distorted and how that affects the most probable eddies that the rotor encounters. This paper introduces further investigation into the structure of the turbulent kinetic energy at the stern of a body of revolution. It provides insight into the distortion and asymmetry of the upwash correlation function at two circumferential locations around the tail exit using compact eddy structure (CES) representation. Comparisons of the CES to a zero pressure gradient, equilibrium boundary layer are made to highlight the anisotropy introduced by the BOR inclination.

5.2 Acknowledgement of others' work

Chapter 5 is a journal paper that is under review. All work in this chapter was done by Jarrod Banks. Data presented is from two experimental tests, the first examining a zero pressure gradient, equilibrium boundary layer measured by Michael Morton and documented in [69]. The second is from the BOR test described in Chapter 4.

Author List: Jarrod T. Banks, Humza Butt, Nathan W. Alexander, William J. Devenport

5.3 Abstract

The compact eddy structure and the correlation structure of three distinct turbulent boundary layers were investigated, with a view to understanding the turbulent inflow seen by an aft-mounted propulsion rotor. The first is of a zero pressure gradient, equilibrium, flate plate boundary layer, the second and third on the lee and port side of a body of revolution (BOR) inclined at five degrees angle of attack. Measurements on the BOR were taken at a body diameter based Reynolds number of 600,000 and a rotor advance ratio of J=1.27. Particle image velocimetry was taken at two principal locations at the aft of the BOR. Distortion of the correlation function was evident in the compact eddy structure of the BOR boundary layer on both the lee and port side. On the port side the turbulent modes were dominated by the embedded shear layer whereas the lee side showed more significant pressure gradient effects in the eddy structure.

Nomenclature

a	=	random time coefficient
D	=	body of revolution diameter
f_s	=	sampling frequency
Hz	=	unit of frequency
m	=	meters
mm	=	millimeters
m/s	=	meters per second
n	=	Mode number
R_{ij}	=	correlation function

$\overline{U}$	=	mean velocity (m/s)
u_i	=	fluctuating velocity (m/s)
^{o}	=	degrees
λ	=	eigenvalue
τ	=	time delay (s)
ϕ	=	eigenvector
Subscripts		
i, j, k	=	direction subscripts
x, r, θ	=	body defined coordinate system
x, y, z	=	flat plate coordinate system

5.4 Introduction

In many flows of interest rotors interact with turbulence producing sound. While turbulence is inherently stochastic or random in nature there are often coherent eddies that can be identified in many turbulent flows. These eddies can vary both in time and space and many reduced order analyses depict the eddies as a spatial distribution. However, using Taylor's frozen flow hypothesis, the time correlations can be stretched into the spatial domain using a convection velocity. Ultimately, in the application of rotor turbulence ingestion noise, the rotor is a time varying sampler of the flow and thus sees the temporal evolution of an eddy rather than what it strictly appears as in the spatial domain. Devenport et al. [31] and Glegg and Devenport [38] demonstrated a compact method to represent instantaneous eddies responsible for the production of sound from the wake of an airfoil. This method is referred to as Compact Eddy Structures (CES) and takes the Proper Orthogonal Decomposition (POD) of the turbulence in the inhomogenous directions and extends each mode in the homogenous

directions using a linear multiplication between the mode and the correlation function. This can be especially useful as it reduces the order of the data required to calculate the noise radiated by a rotor. Rather than considering the full streamwise plane of data, the analysis is restricted to a one dimensional time series of a profile.

5.5 Literature Review

Some work into the energy containing eddies and acoustic source terms in turbulent boundary layers have been investigated by Morton. Morton [69] documented the space-time correlation function of a high Reynolds number, equilibrium turbulent boundary layer as a function of time delay, wall normal position and spanwise separation. He then went on to examine the compact eddy structure at the first 4 POD modes and identified a large scale structure that dominated the first mode as well as smaller traditional eddy structures at 0.3δ in the second mode and 0.5δ in the fourth mode.

The ingestion of three dimensional boundary layers within the context of rotor ingestion at the aft of a slender body of revolution has been discussed in some detail by Muench [70], Huyer and Snarski [51], and Huyer and Beal [50]. Huyer and Snarski [51] provided detailed measurements of the mean flow and turbulent inflow of velocity profiles normal to the surface of a body of revolution. The model used for all three studies ([70], [51], and [50]) consisted of a narrowing tail with 8 stators 3.9 cm upstream of a 6-bladed SISUP propellor. Tests were undertaken at the Naval Undersea Warfare Center, Division Newport in its open jet wind tunnel facility. Huyer and Snarski [51] reported stator wake deficits on the order of 30% of the freestream and the turbulence intensity in the stator wake was shown to be greater than that of the boundary layer. No vortex shedding by the stators was noted and this was attributed to the turbulent nature of the boundary layer the stators

were immersed in. An extension of this investigation was carried out by Huyer and Beal [50] where they presented a turbulent propulsor inflow model for use in time-domain rotor noise predictions. This was then applied to their propulsor unsteady flow code and an unsteady force spectrum calculated. From there the method of Goldstein [41] was used to compute the far field noise. The noise predictions were compared to the data acquired by Muench [70]. Overall this method was successful at recovering the tonal and broadband components of the radiated noise below the first three blade harmonics. Above that frequency tones appear in Muench's experimental data that the noise prediction does not capture. Instead it shows the broadband levels dominating the remainder of the spectrum. Above the 11th blade rate, the broadband levels of the prediction decrease and blade rate tones reassert themselves. Huyer and Beal make the assertion that this may be a result of the turbulent model development being non-physical.

While three dimensional flow separation is found in many flows of interest, detailed measurements in the context of its interaction with rotors at the aft of a slender body of revolution has been little studied. Details of the turbulent cross flow separation generated by a 6:1 prolate spheroid at inclination were conducted by Ahn [2], Chesnakas [26], and Chesnakas and Simpson [28], [27], [29]. Ahn [2] quantified the effects of increasing Reynolds number and angle of attack on the separation incipience. He determined that the Reynolds number is only weakly related to separation incipience and the variation in the location of the separation depends more on the angle of attack. Surface oil flow results demonstrated that increasing the angle of attack serves to move the separation line upstream and towards the lee side. Chesnakas and Simpson [29] documented the turbulent kinetic energy distribution as a result of the three dimensional separation and found that the separation pulls highly turbulent flow off the wall and into the boundary layer forming an embedded shear layer that evolves with location about the prolate spheroid. Banks et al. [17] showed that this

separation was present in a plane on the port side of a body of revolution with an ellipsoidal nose and conical tail inclined at 5^o angle off attack. Further investigation of a circumferential plane showed the existence of a vortex between the lee and starboard side, confirming a similar flow structure between Chesnakas and Simpson [29] findings and Banks et al. [17] findings.

This paper aims to extend the analysis of Banks et al. [17] by decomposing and examining the strongest turbulent fluctuations responsible for the energy within a non-equilibrium, three dimensional boundary layer approaching an idealized propulsion rotor at the stern of a body of revolution. The flow will be visualized using proper orthogonal decomposition and compact eddy structures. These reduced order data techniques allow the preferred form of eddies contained in a turbulent boundary layer to be visualized. Comparisons between the CES of an equilibrium turbulent boundary layer is provided and the impact of the three dimensionality and adverse pressure gradient along the tail of the BOR on the eddies in the flow is investigated. The following section 5.6 is a description of the experimental facility and methods, following this a discussion of the data reduction methods of POD and CES in section 5.7. Finally the instantaneous and mean velocities in the PIV plane are presented along with slices of the correlation function, the POD mode profiles and energy distribution, and concluding with the form of each CES mode in Section 5.8. Section 5.9 summarizes the impact of the BOR on the boundary layer and concludes that the shear layer on the port side concentrates the eddy structures within a small portion of the boundary layer. The adverse pressure gradient over the tail of the BOR skews the correlation structure on the lee side and a comparison of the port side embedded shear layer and the equilibrium boundary layer found similarities between certain modes.

5.6 Experimental Methods

The data presented in this paper consists of two different experimental campaigns. The focus of the paper is on the three dimensional boundary layer examined by the data collected for the body of revolution experiment. However, to provide context, data from a significantly earlier test conducted by Michael Morton and documented in [69] is also shown. The experimental details of this test can be found in Mortons thesis [69] and published works [68] and only the minimum required to interpret the data are discussed in this paper.

5.6.1 Experimental Facility

Experimental measurements of the body of revolution (BOR) were made in the Virginia Tech Stability Wind Tunnel (VTSWT) in its anechoic configuration. The test section consists of two Kevlar side walls and a floor and ceiling formed from Kevlar covered panels treated to minimize acoustic reflection. It has dimensions of 1.85 m x 1.85 m x 7.32 m. Maximum flow capability of this facility is 80 m/s with freestream turbulence levels less than 0.01% at 20 m/s and a freestream uniformity of 0.5% at 47 m/s (Devenport et al. [32]) .

5.6.2 Body Centered Coordinate System

The local coordinate system used for the BOR in the experimental test is a right-handed, body oriented cylindrical system shown in figure 5.1a. The origin is centered on the BOR nose and the principal coordinates are described looking at the BOR nose from upstream. x is positive downstream along the body axis, r is always positive and radiates outward orthogonal to the x coordinate, and θ is referenced orthogonal to the x coordinate and in the same plane as the radial component. θ is positive clockwise when viewing the nose

from upstream. To aid in discussion of the various parts of the flow the location of each measurement plane will be defined in the context of figure 5.1. The body centered coordinates are oriented such that $\theta = 180^o$ corresponds to the lee side. Conversely, the windward side occurs at $\theta = 0^o$ and the port and starboard sides of the body are at $\theta = 90^o$ and 270^o respectively. The body diameter is used in normalization of the radial and axial components and given by $D = 432$ mm. The coordinate system used in the equilibrium boundary

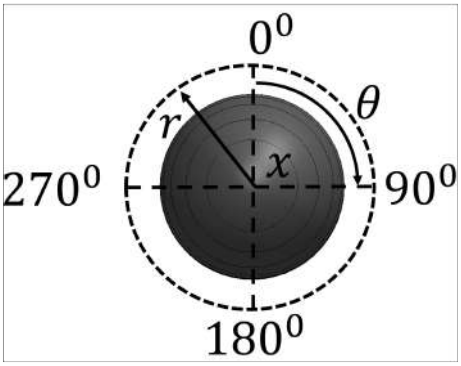

(a)

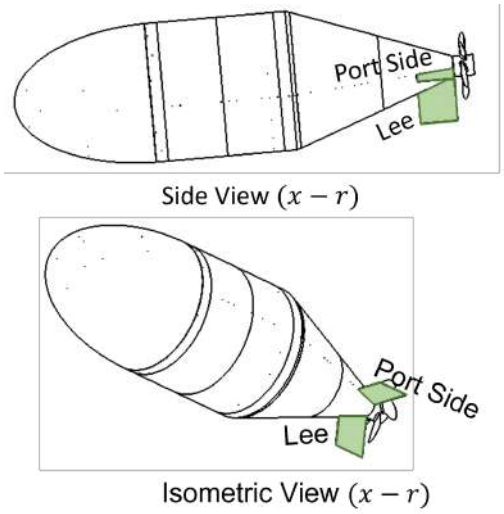

(b)

Figure 5.1: Coordinate systems for each measurement. a) Body centered cylindrical coordinate system with the x coordinate positive axially downstream, r coordinate positive normal to the body surface, and θ coordinate positive clockwise. The streamwise coordinate x is perpendicular to the $r-\theta$ plane and the rotor rotates anti-clockwise in this frame of reference. b) Schematic showing the side and isometric views of the location of the PIV measurements in the $x-r$ plane.

layer is slightly different but completely analogous. Similar to the BOR coordinate system it uses a right-handed, surface oriented coordinate system with x positive downstream, y normal to the wall and positive away from the wall and z parallel to the wall completing the right-handed system. To allow for comparisons between the velocities in the two coordinate systems the analogous velocities are simply; $U_x = U_x$, $U_y = U_r$, and $U_z = U_\theta$.

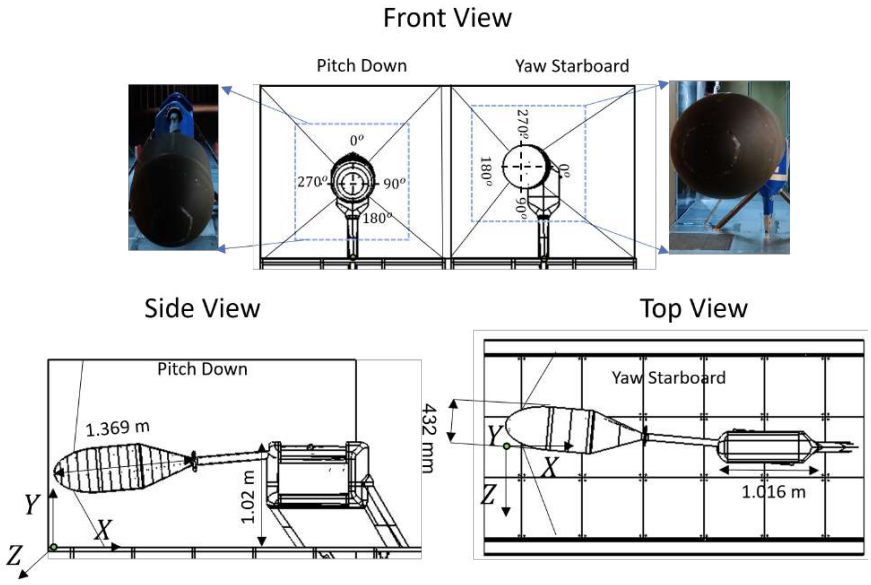

Figure 5.2: Schematic of the experimental setups used to measure different sections of the flow about the body. The top row shows the front view of the pitch down and yaw starboard configurations. The bottom row shows the side of the pitch down configuration and the top view of the yaw starboard configuration. Principal dimensions of the body and structure are shown as well as the approximate location of the tethers.

5.6.3 Model

The BOR was tested in two configurations, pitch down and yaw starboard, illustrated in figure 5.2. The nose is a 2:1 ellipsoid and the mid-body is a 432 mm diameter cylinder, and the aft section is a 1.17D long section with a 20^o ramp that produces an adverse pressure gradient. Trip rings at $x/D = 0.98$ produce a turbulent boundary layer which is grown over the length of the midbody. A tether system consisting of four 1.58mm diameter wires were used to anchor the cantilevered body of revolution in place. The tethers are attached at $x/D = 1$ and extend to the corners of the test section. The rotor blades are a modified NACA 66 airfoil made from 6061 aluminum and wake adapted for the boundary layer profile measured at the aft of the BOR. The rotor has a 216 mm diameter and is mounted on a 50 mm diameter drive shaft.

5.6.4 Particle Image Velocimetry

The velocity and turbulence at the aft of the BOR was measured using particle image velocimetry (PIV). The imaged region extended over a 160 x 160 mm^2 area with a 4.2 mm spatial resolution. A Photonics Industries DM laser combined with two Phantom v2512 cameras equipped with Nikon 200 mm lenses and a Davis Programmable Timing Unit (PTU X) were used to acquire the PIV. The sampling rate used was 12.848 kHz and the cameras acquired data in dual frame/dual pulse mode. The PIV was recorded in blocks, referred to as cycles, that begin at the same point of the shaft rotation for each block of data. This was achieved using an optical sensor and a mark on the shaft that sent a trigger signal to the PTU once per rotation. This method of data acquisition allowed phase averaging of the velocity field and hence phase averaged subtraction of the mean velocities to give a truly zero mean velocity time series.

5.7 Flow Decomposition

5.7.1 Proper Orthogonal Decomposition

Proper Orthogonal Decomposition is a form of reduced order analysis and derives its use from a Principal Component Analysis known as a Karhunen-Loeve decomposition. This decomposition, like so many of the techniques used when examining turbulent velocity fields, finds its roots in statistics. It was first used in the context of turbulence and coherent eddy identification by Lumley [19]. It aims to find an orthogonal basis for a modal decomposition from a space or time based signal ensemble by solving the Fredholm equation and is simply the eigenvalue or singular value decomposition of the zero time-delay correlation function of the radial profile. In the BOR cylindrical coordinates this equation becomes,

$$\int R_{ij}(r, r', 0)\phi_j^{(n)}(r')dr' = \lambda^{(n)}\phi_i^{(n)}(r) \tag{5.1}$$

This allows the flow to be described by a certain number of orthonormal modes, ordered by energy contribution to the overall mean square of the velocity fluctuations. The eigenvalues, represented by $\lambda^{(n)}$ in equation 5.1, give the modal energy, while the eigenvectors, represented by $\phi_i^{(n)}(r)$, give the velocity distribution at a point r. The velocity field or profile can then be reconstructed at each time instant using the time coefficients in the following manner,

$$u_i(r, t) = \sum_n a_n(t)\phi_i^{(n)}(r) \tag{5.2}$$

In homogenous turbulence POD reduces to the more familiar Fourier decomposition in wavenumber space and is less useful in the reconstruction of flow eddies. In an effort to recreate the most probable instantaneous eddies a combination of POD and a statistical method known as Linear Stochastic Estimation (LSE) will be used. The details of LSE and a mathematical extension termed Compact Eddy Structures (CES) will be described in the next section.

5.7.2 Linear Stochastic Estimation and Compact Eddy Structures

Linear Stochastic Estimation (Adrian [1]) is a method of producing eddy like structures within a flow. Given some stated condition, such as a starting velocity fluctuation, the best linear estimate of the instantaneous velocity in either time or space for a single point can be readily determined through a linear multiplication of the starting condition with the correlation function of the flow.

$$u_j(r',\tau)|_{LSE} = R_{ij}(r,r',\tau)\left[u_i(r)/\overline{u_i(r)^2}\right] \tag{5.3}$$

This is most applicable to homogenous turbulence, while POD is most efficient in application to inhomogenous turbulence. Thus we can apply POD in the inhomogenous directions of a turbulent flow to obtain the most energetic modes while using the simpler linear stochastic estimation in the homogenous directions and obtain eddy like structures. In the case examined in this paper POD is applied to profiles in the radial direction while linear stochastic estimation is applied in the direction in which the flow is changing comparatively slowly and is approximately homogenous. This method is referred to as Compact Eddy Structures and will be applied in the following section. The CES associated with a given vector proper orthogonal mode $\phi_i^{(n)}(r)$ flow can be given by summing up all contributions to each flow from the correlation function at each point in the following manner,

$$u_j^{(n)}(r',\tau)|_{CES} = \frac{1}{\lambda^{(n)}}\int \phi_i^{(n)}(r)R_{ij}(r,r',\tau)dr \tag{5.4}$$

This method is useful as it only requires a small fraction of the data as an input to compute much of the turbulent flow the rotor experiences. However, it does require a sufficiently long time series for the statistics to be converged but it is still relatively memory compact as it only requires a profile just upstream of the rotor inflow to describe much of the features of the flow field the rotor interacts with.

5.7.3 Flow Application

We will begin by writing the fluctuating velocity time series for a one dimensional profile $u_i(r,t)$ and then decompose the flow using POD in the inhomogenous direction, given by r, for a single profile at the tail exit, $x/D = 3.17$. This is done by solving equation 5.1 and

obtaining the eigenvalues and eigenvectors of the zero time delay correlation function of the profiles given by equation 5.5 below,

$$R_{ij}(r, r') = E[u_i(r, t)u_j(r, t)] \tag{5.5}$$

Practically, obtaining $R_{ij}(r, r')$ is computationally easier than calculating the full time delay correlation function as it is simply the inner product of the profile matrix with its transpose, normalized on the number of samples in the time series in the following way,

$$R_{ij}(r, r') = \frac{1}{n-1} \begin{bmatrix} u_x(r,t) \\ u_r(r,t) \\ u_\theta(r,t) \end{bmatrix} \begin{bmatrix} u_x(r,t) & u_r(r,t) & u_\theta(r,t) \end{bmatrix} \tag{5.6}$$

The full time-delay correlation function, $R_{ij}(r, r', \tau)$, that will be used to extend the POD profiles into the time domain is calculated by taking the Fourier transform of the time series of each point in the profile, obtaining the cross-spectral density matrix and then inverse Fourier transforming it to obtain the correlation function.

5.8 Results and Discussion

All data presented for the three dimensional boundary layer were taken at a body diameter based Reynolds number of 600 000, and a rotor advance ratio of $J = 1.27$. For comparison data from Morton [69], [68] for a zero pressure, equilibrium turbulent boundary layer are also presented. A brief summary of the flow acquisition details extracted from [69] is given here.

These data were taken at a momentum based Reynolds number of 16 607 and a reference freestream velocity of 30 m/s. The flow was also measured in the VTSWT, however, the configuration of the tunnel in 2012 was slightly different. The test section was modified with a modular false wall that allowed the pressure gradient to be carefully controlled such that the turbulent boundary was subjected to a zero pressure gradient over the length of the measurement. The false wall panels were manufactured from Lexan and reduced the test section width from 1.85m to 1.73m. The boundary layer was tripped to turbulence 1.2 m upstream of the test section by an aluminium right angle and the measurements were taken in a wall normal plane 4.72 m downstream of the turbulence trip. Two point measurements of the turbulent boundary layer were taken by Auspex AVOP-4-100 four-sensor hotwires calibrated using King's Law. A grid of 31 points for each fixed probe location were taken yielding 1 781 measurement points.

Boundary layer parameters for each measurement are shown below in table 5.1.

Measurement	$U_{ref}[m/s]$	$\delta[mm]$	Re_θ	Re_δ
Equilibrium boundary layer	30.01	102	16 607	194 306
Lee Side	23.3	114	39 870	160 000
Port Side	22.75	107	33 900	146 000

Table 5.1: Boundary layer parameters for each measurement.

5.8.1 Mean and Instantaneous Velocity Distribution

To gain an understanding of the type of flow examined on the BOR we will start with a look at the instantaneous and mean velocities for the two planes in the three dimensional, non-equilibrium boundary layer. Figure 5.3a and b show the contours of the instantaneous velocity for two planes taken in the rotor near field. The rotor leading edge is located 17.2 mm downstream of the tail exit at x/D=3.21. Quite clearly the flow in figure 5.3b

displays higher spatial variation while that in figure 5.3a is significantly smoother. Evidence of rotating eddies are seen throughout the plane on the lee side however the port side flow appears more chaotic. While both 5.3a and b show the axial velocity decreasing as the flow gets closer to the body surface, the port side measurement shows a significant drop off to nearly 3 m/s below an x/D of 0.2 while the lowest velocity on the lee side is around 8 m/s. The turbulent character of the port side is manifested further in figure 5.4a and b where a band of high $\overline{U_x}$ variation with r/D is seen between $r/D = 0.25$ and $r/D = 0.18$. Figure 5.5 presents the Reynolds stress within the measurement plane. This component of the data was computed slightly differently than typical Reynolds stress calculations due to some noise in the measurement. Rather than taking the mean square of the fluctuating velocities the time delay correlation function is calculated and the first three time separations are linearly interpolated to zero time delay to get the Reynolds stress. This served to remove significant amounts of measurement noise, especially just upstream of the rotor in figure 5.5a. The contour levels of figure 5.5a are 1/10th those of 5.5b due to a band of highly turbulent flow evident between $r/D = 0.25$ and $r/D = 0.18$. Banks et al. [17] investigated and identified the source of this high turbulence region to be three dimensional separation as a result of a highly adverse pressure gradient on the lee side pulling near wall turbulence away from the wall. This separation then rolls up into a pair of vortices between the lee and port/starboard sides. The intensity of the turbulent fluctuations in this shear layer imply that there should be strong correlations between velocity components within the region of the embedded shear layer. A profile at $x/D = 3.17$ for the lee and port side data will now be investigated and the correlation function, POD modes, and compact eddy structures examined.

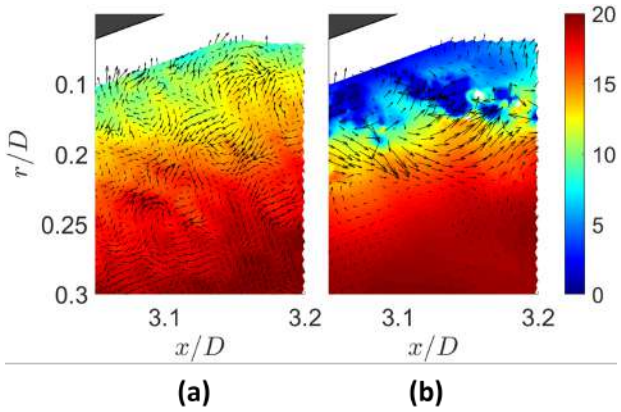

Figure 5.3: Contours of the instantaneous axial velocity U_x (m/s) on (a) the lee ($\theta = 180^o$) and (b) the port ($\theta = 90^o$) side of the body of revolution. Vectors of the phase mean subtracted data are shown overlaid on the contours.

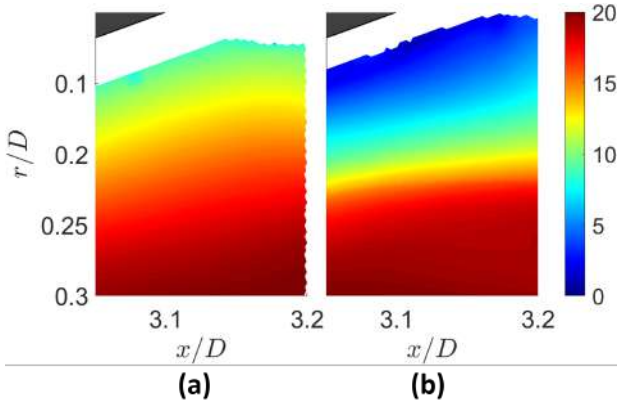

Figure 5.4: Contours of the mean axial velocity $\overline{U_x}$ (m/s) on (a) the lee ($\theta = 180^o$) and (b) the port ($\theta = 90^o$) side of the body of revolution.

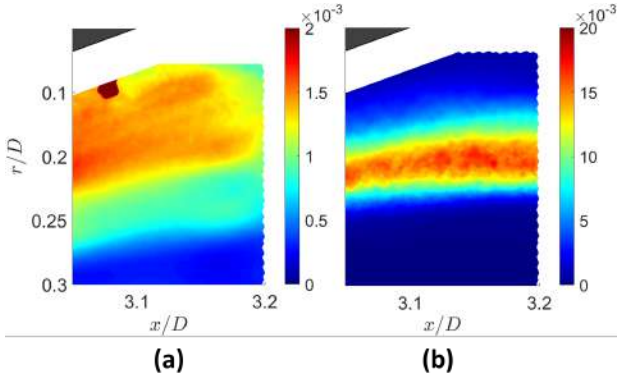

Figure 5.5: Contours of the mean Reynolds normal stress normalized on the square of the free stream velocity $\overline{u_x^2}/U_\infty^2$ on (a) the lee ($\theta = 180^o$) and (b) the port ($\theta = 90^o$) side of the body of revolution. The lee side color scale is set to 1/10th that of the port side.

5.8.2 Zero Time Delay Correlation Function of Surface Normal Profiles

The correlation functions presented here are those used to extend the POD modal profiles into the homogenous directions and are presented for the lee and port side PIV planes as well as the ZPG boundary layer. Figure 5.6a, 5.6b, and 5.6c shows the zero time delay correlation function for the profile at $x/D = 3.17$ represented by $R_{ij}(y, y', \tau = 0)$ and $R_{ij}(r, r', \tau = 0)$. This is the correlation between each point in the profile and every other point. The profiles are normalized on the boundary layer thickness δ. The corresponding i and j index of each part of the correlation function is shown on the plots where the indices 1, 2, 3 are x, r, θ and, x, y, z for the BOR and equilibrium boundary layer data respectively. The diagonal of each plot shows the auto-correlations of each velocity component while the off diagonals show the cross-correlations. Clearly there will be a maximum auto-correlation when $r/\delta = r/\delta'$ as the correlation between the same point and the same velocity component is perfect by definition. This is represented in the contours by the maximum for each profile occurring along the diagonal of the plot. Figure 5.6a shows the correlation function for the ZPG equilibrium boundary layer of Morton [69]. The auto-correlation terms (R_{11}, R_{22}, R_{33}) have symmetric

correlation lobes that are strongest along the diagonal and increase in strength as the probes move closer to the wall. The lack of cross-correlation between the third component (u_z, parallel to the wall) and either of the first or second components serves to confirm the two dimensionality of the boundary layer for these measurements. Seeing non-negligible cross-correlations between the third component and the first and second component is evidence of three dimensional structures within the profile. There is a strong negative correlation between the u_x and u_y, or R_{12}/R_{21}, components. This is consistent with most boundary layer measurements in which the shear stress in a ZPG equilibrium boundary layer is negative. Negative lobes surrounding the main correlation ridge are evident in R_{33} and these decay with distance away from the wall.

Figure 5.6b shows features that are similar to figure 5.6a with some subtle differences, specifically in the cross-correlation plots. Unlike the R_{12} and R_{23} correlations in the equilibrium boundary layer there are clearly three dimensional structures on the lee and port side of the body of revolution. These are evident in the strength of the cross-correlation terms. Arguably the most interesting information is found in figure 5.6c. The embedded shear layer discussed in Banks et al. [17] is clearly evident in the correlation function in all 9 tensor components. The auto-correlations peak between 0.4δ and 0.7δ with the strongest component being R_{11} and the weakest being R_{13}. All three auto-correlation components show negative correlation wings on either side of the main correlation ridge with the strongest wings evident in the R_{22} component. Overall the correlation values for the embedded shear layer on the port side show significant elevation over both the equilibrium boundary layer and the flow on the lee side of the body. Not only is this indicative of a highly turbulent flow, the magnitudes of the cross-correlation terms on the port side of the body imply that the flow within the embedded shear layer also consists of correlated rotational eddies in the $u_x - u_r$, $u_x - u_\theta$, and $u_r - u_\theta$ planes.

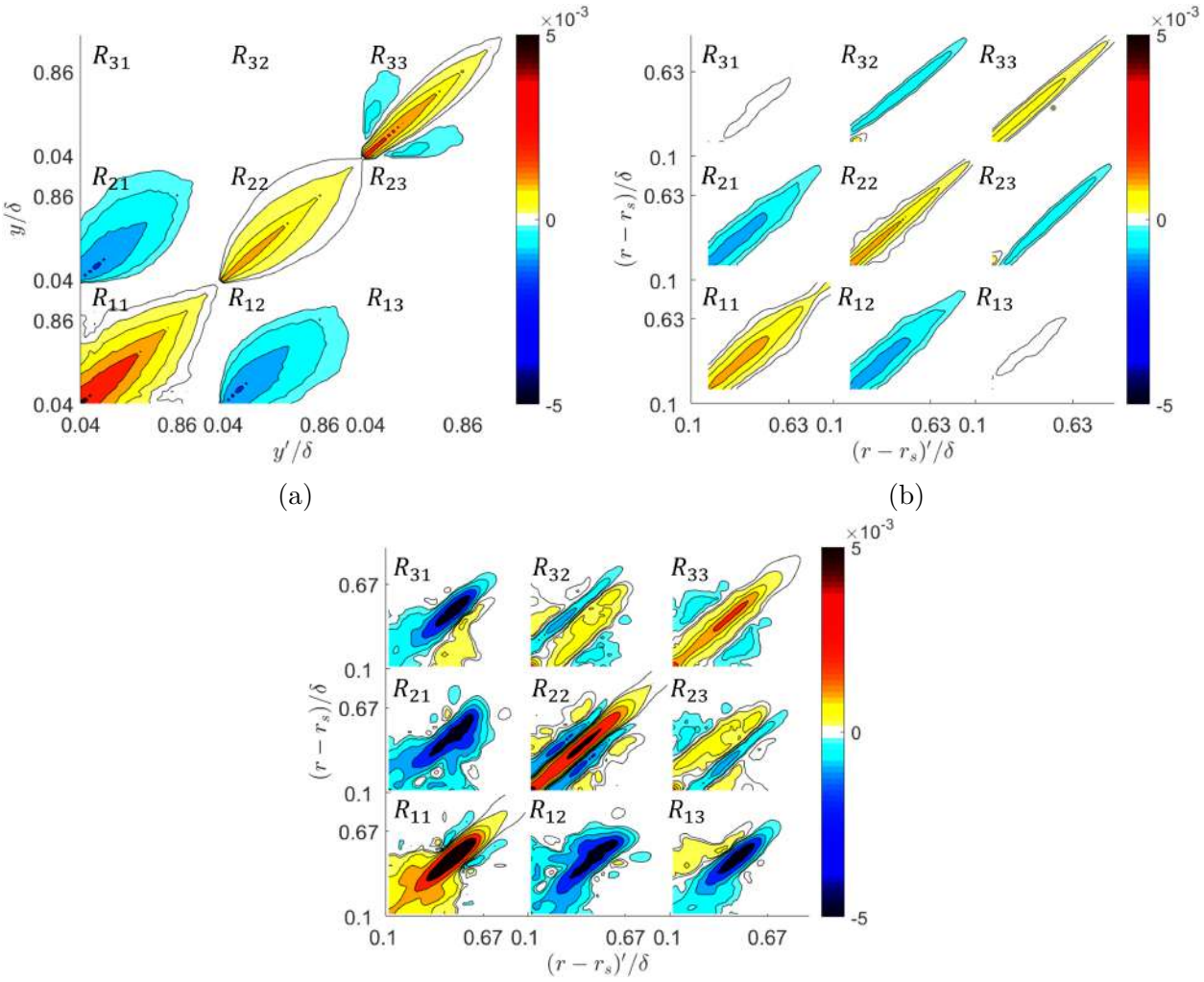

(a) (b)

(c)

Figure 5.6: The zero time delay correlation function for boundary layer profiles normalized on the square of the boundary layer edge velocity ($R_{ij}(r, r', \tau = 0)/U_e^2$) with select contour levels plotted. a) Equilibrium boundary layer profile. b) Lee side boundary layer profile at the tailcone exit. c) Port side boundary layer profile at the tail cone exit.

5.8.3 Proper Orthogonal Decomposition of Surface Normal Profiles

The dominant modes of the proper orthogonal decomposition were computed using the eigenvector decomposition and are shown in figure 5.7. The first four modes are computed as they comprise between 40 and 50% of the total energy in each flow. This is illustrated in figure 5.8. It should be further noted that most of the energy, about 70%, can be represented by just 15 modes for each boundary layer. Figure 5.7a shows the modes for the equilibrium boundary layer while figures 5.7b and 5.7c show the modes for the lee and port sides of the BOR respectively. Both the equilibrium and lee side modes appear to have shapes that are distributed throughout the boundary layer. In contrast, figure 5.7c clearly shows the primary energy focused around the embedded shear layer (0.4δ to 0.7δ) for all four modes.

5.8.4 Compact Eddy Structures

The modes shown in figure 5.7 can be visualized in the spatial domain by integrating the product of each point in the modal profile with its space and time delay correlation function $R_{ij}(r, r', \tau)$. Mathematically this process is given in equation 5.4 and is repeated below,

$$u_j^{(n)}(r', \tau)|_{CES} = \frac{1}{\lambda^{(n)}} \int \phi_i^{(n)} R_{ij}(r, r', \tau) dr \tag{5.7}$$

The fluctuations are normalized on the corresponding modal energy given by the corresponding eigenvalue $\lambda^{(n)}$. Figure 5.9 shows the compact eddy structures for the first four modes for the equilibrium boundary layer (5.9a), the lee side of the BOR (5.9b), and the port side of the BOR (5.9c). In all cases the first mode is dominated by the streamwise fluctuations with the compact eddy structure having a fairly simple form. The first mode of the equilibrium

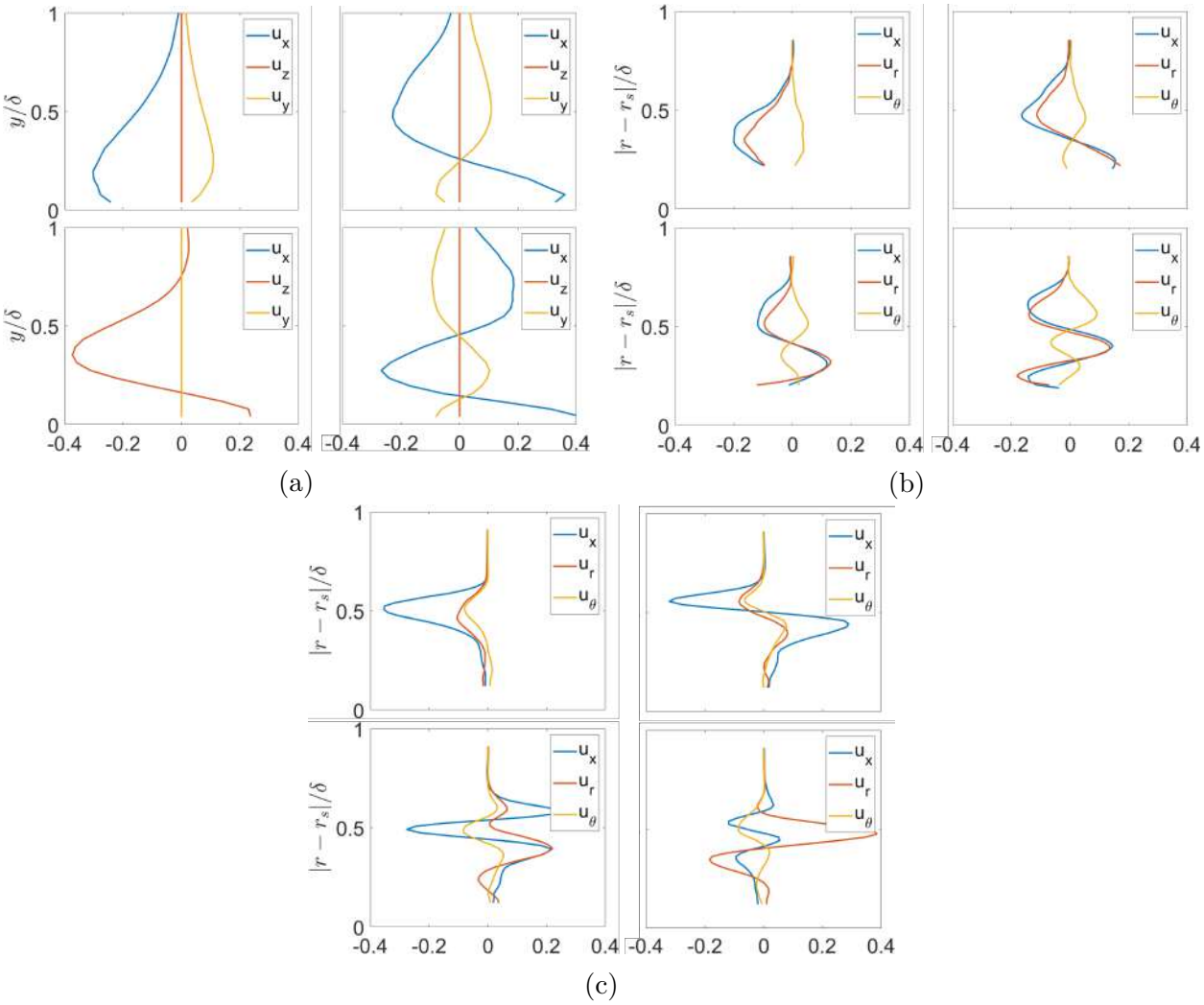

Figure 5.7: Proper orthogonal decompositions for wall normal profiles. a) Equilibrium boundary layer b) lee side of the body of revolution at $x/D = 3.17$ c) port side of the body of revolution at $x/D = 3.17$. Profiles are shown for the first four modes. The mode order is 1. top left, 2. top right, 3. bottom left, and 4. bottom right.

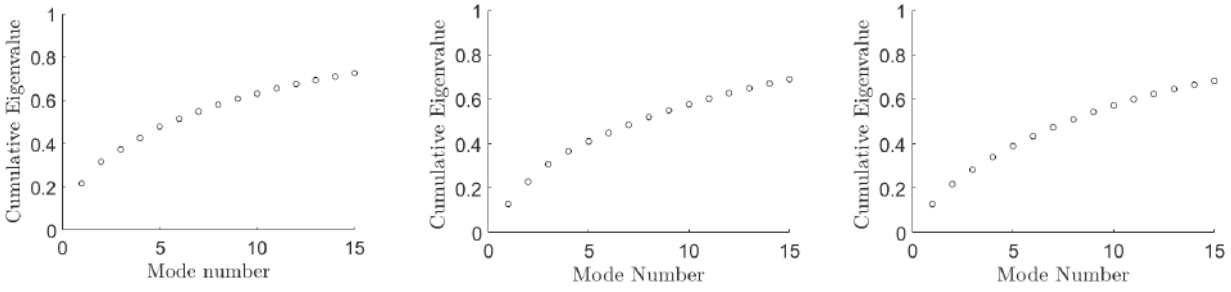

(a) (b) (c)

Figure 5.8: The cumulative eigenvalue distribution between modes representing the overall contribution to the turbulent energy for each mode number in a) equilibrium boundary layer b) lee side of the body of revolution at $x/D = 3.17$ c) port side of the body of revolution at $x/D = 3.17$.

boundary layer shows a structure that spans approximately 60% of the boundary layer and grows in strength towards the surface. The first mode on the lee and port side are similarly simple in form however the lee side shows a skewed structure that appears to move away from the wall with increased time delay. On the port side a narrow, intense set of streamwise fluctuations focused within the embedded shear layer are present. Roller type structures focused around zero time delay appear in the second and fourth mode in the equilibrium boundary layer while elongated rotational eddies are seen on the port side second and third mode. The third mode of the equilibrium boundary layer shows very little, but recall figure 5.7a where it becomes clear that the third mode is dominated by the fluctuations in the transverse/wall parallel (u_z) component. The u_x and u_y modes are near zero so there is very little energy when examining the u_x, u_y mode shown in figure 5.9a. Examining figure 5.9b an interesting inclination is evident in all modes on the lee side compact eddy structure. The formation of this is most likely due to the 3 dimensional skewing of the turbulence that the body introduces. In fact, it was noted in Glegg et al. [37] that the apparent length scale necessary to produce the sound generated by a rotor ingesting this turbulence is twice that of the measured axial length scale. This led him to hypothesize that a large scale turbulent

structure is skewed in such a way that the rotor sees it as if it is several times longer. The skewing of this structure is related to the two point correlation function examined in Banks et al. [16]. The zero time delay, two point correlation function for the axial fluctuations on the lee side are shown to be stretched in the streamwise direction with a 17^o inclination away from the surface as the flow moves downstream. The inclination of the structure shown in figure 5.9b matches the rotation direction and magnitude closely.

In fact the angle of inclination of the structure using the temporal correlation function is within a degree of the spatial correlation function. This suggests a close relationship between the spatial correlation function for the entire measurement plane and the temporal correlation function of the profile used to obtain these compact eddy structures which is consistent with Taylor's hypothesis.

In general the modes in the BOR boundary layer showed greater correlation values over greater time separations than the two dimensional, equilibrium boundary layer. Modes two and three of the port side boundary layer appear to be stretched copies of modes two and four of the equlibrium boundary layer. This observation implies that the sound produced when the rotor interacts with the longer time scale eddies on the port side is likely to be more strongly correlated along the blade span and between blade passages than the equilibrium boundary layer. Additionally, the first CES mode of each boundary layer is a strong streamwise fluctuation. In the equilibrium boundary layer this is concentrated beneath 50% of the boundary layer edge, on the lee side this structure extends out to 70% of the boundary layer and on the port side this fluctuation is concentrated between 40% and 60% of the boundary layer. In general the closer fluctuations are to the tip of the blade the more impact they will have on the radiated sound as the blade velocity increases from hub to tip. Therefore the fluctuations on the lee and port side, which are also mostly normal to the blade surface, are more efficient sound producing eddies.

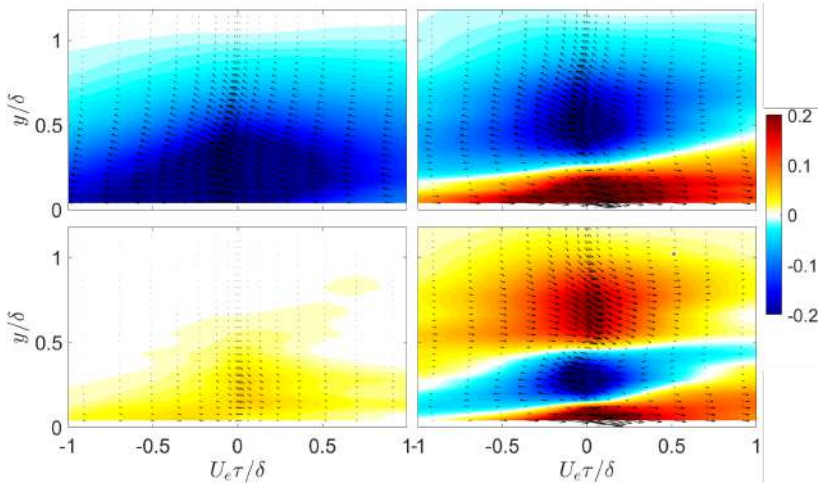

(a)

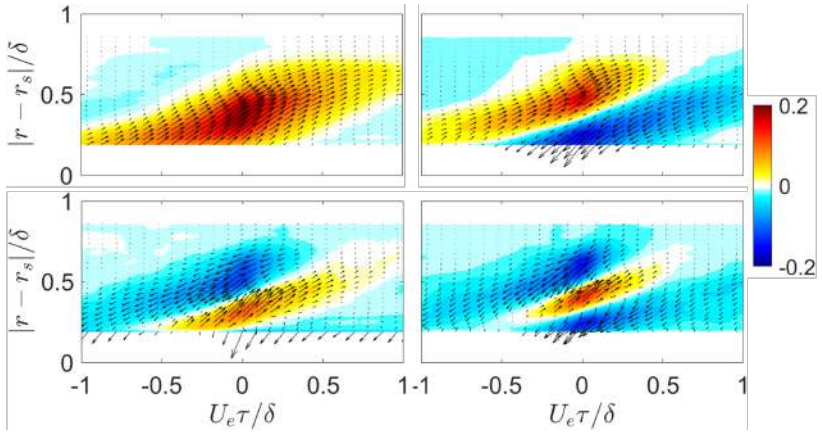

(b)

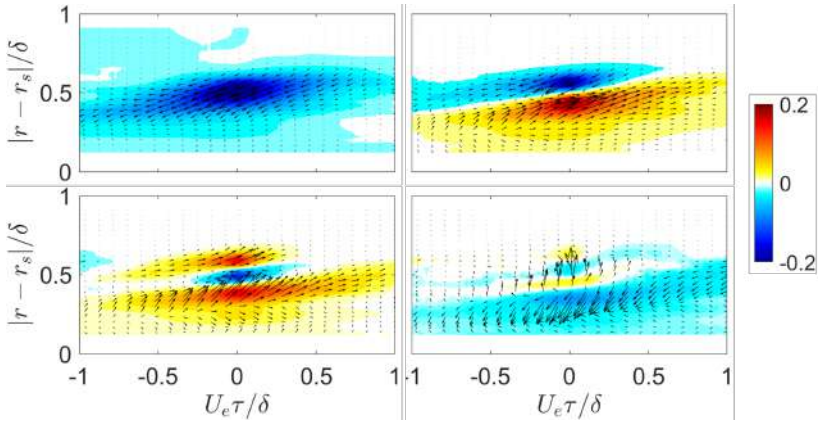

(c)

Figure 5.9: Compact eddy structures for wall normal profiles. The first four modes are plotted for a) the equilibrium boundary layer b) the lee side of the body of revolution at $x/D = 3.17$, and c) the port side of the body of revolution at $x/D = 3.17$. The mode order is 1. top left, 2. top right, 3. bottom left, and 4. bottom right. Contours of the u_x mode are overlaid on the plots.

5.9 Conclusion

The decomposition of three turbulent profiles; the first in a zero pressure gradient, equilibrium boundary layer, the second on the lee side of a body of revolution, and the third on the port side of a body of revolution, was done using proper orthogonal decomposition. The compact eddy structure of each flow was examined and key insights into the energy containing eddies within each flow were given. In the equilibrium boundary layer compact roller type eddies were revealed at 0.3δ in the second mode and at 0.5δ in the fourth mode. Similar, more elongated motions, were noted in the portside second and third mode. The impact of a high turbulence shear layer on the port side of the BOR was revealed in the dominant fluctuating velocity modes. The first three CES modes on the port side are highly concentrated within the embedded shear layer. The modes of the lee side were inclined anticlockwise, moving away from the surface with increasing time delay. The effect of the CES on the sound as they interact with the rotor is theorized and it is thought that the first mode for the three dimensional boundary layer will be a more efficient producer of sound than that of the equilibrium boundary layer. The elongation of the CES modes on the port side is also thought to increase blade span and blade to blade correlation.

Acknowledgments

The authors would like to thank the Office of Naval Research for sponsoring this work under grant N00014-20-1-2650, and specifically Drs. Yin Lu Young, Ki-Han Kim and John Muench. Further acknowledgements go to Humza Butt, Vidya Vishwanathan, Shishir Damani, Rachel Andrews, Aayush Salot, and Shivam Khullar amongst others for their assistance during the wind tunnel experiments. The author would also like to thank Mr. Michael Marcolini for

his ever present advice.

Chapter 6

Open Rotor Immersed in a Turbulent Boundary Layer Ingesting Turbulent Gusts

6.1 Context

Existing turbulence correlation based prediction methods are not capable of predictions when the flow is transient. As a result experimental work into the sources of deterministic and stochastic sound sources within the ingestion of a transient into a rotor is necessary. An understanding of the coupling of the disturbance and rotor interaction is also necessary. This paper attempts to identify flow synchronized sources of sound as a result of the ingestion of a turbulent transient. It shows that the generation of sound during the ingestion of the transient is due to unsteady behaviour of the disturbance generator. The unsteady nature of the disturbance is investigated and the character of the sound is shown to be tonal during the first half of the transient and shift to broadband in the latter half of the transient.

6.2 Acknowledgement of others' work

Chapter 5 is a journal paper that is to be submitted. Some work from other students and professors is included as part of the paper. Dr Nathan Alexander assisted in the writing of Section 6.4.2. Shaheen Thimmiah Palanganda contributed greatly to the design of the deterministic disturbance generator described in Section 6.5.7. He was responsible for figures 6.9, and 6.10 as well as Tables 6.1 and 6.3. Szu-fu Huang produced all acoustic figures and was responsible for the microphone experimental descriptions in Section 6.5.5 and 6.5.7. He provided figures 6.5, 6.6, 6.14, and 6.15. His work is also seen in figures 6.17 and 6.20a in the acoustic spectra contour maps. All other figures as well as all analysis and discussion was done by Jarrod Banks.

Author List: Jarrod T. Banks, Szu-Fu Huang, Shaheen T. Palanganda, Daji Chen, Nathan W. Alexander, William J. Devenport

6.3 Abstract

The acoustics and flow characteristics of a rotor ingesting a planar boundary layer and periodic transient disturbances were measured. The motion was determined to be truly unsteady using a quasi-steady reconstruction of the flow and sound. The dominant sound produced during the transient was a result of a deterministic change in the blade angle of attack that produced an unsteady loading on the rotor. The probabilistic component of the sound was found to be dominant towards the end of the transient and during the post-transient steady state due to the increased turbulence levels ingested by the rotor.

6.4 Introduction

The proliferation of small, light haul rotorcraft in urban spaces has led to significant research and development into the practical challenges of making these rotorcraft feasible on larger scales. This has focused primarily on rotor systems designed to produce sufficient lift and range in an affordable package. As such the human factors and influence of these designs have been neglected until recently. A focus on noise control in the design process is necessary to avoid public backlash as their use in urban spaces increase.

Consider figure 6.1 which shows the Joby Aircraft eVTOL concept taxi. Joby Aircraft has made significant efforts in reducing the aeroacoustic footprint in their concept eVTOL vehicle. They achieve this by increasing the number of rotors, reducing the rotor tip speed and reducing the coherent wake interaction common to helicopters (BVI). This makes significant strides in reducing the loading and thickness noise produced by this aircraft however there is still the interaction of the aft rotors with the wake generated by the forward rotors as well as transient effects when the aircraft changes configuration between vertical liftoff and forward

Figure 6.1: Joby Aircraft's eVTOL taxi delivered to Edwards Air Force Base [13]

flight. The most serious challenge here is the noise generated by the aircraft during transient maneuvers. Not only is this subjectively the most important source, it will dominate vehicle operations close to the ground where the vehicle is closest to people. Prior studies of transient, or maneuvering, vehicle flows have been limited to narrow applications where the range of phenomena encountered is small compared to that which will be produced by a configuration as complex as that shown in figure 6.1.

6.4.1 Transient Rotor Noise Predictions

Significant work on the development of sound prediction models for transient interactions in rotor systems has been undertaken by authors such as Brentner and Jones [22], Chen et al [25], and Hennes et al. [46] amongst others. These studies have mostly focused on transient helicopter maneuvers and attempt to extend the capability of existing noise prediction codes such as WOPWOP [21]. The main deficiency noted is that the existing prediction methods assume either steady flight or a very simple constant acceleration in one direction, referred to as rectilinear motion. Brentner and Jones [22] presented a first principles noise prediction method for maneuvering helicopters. They address very specific aspects of the transient

noise radiation problem including trimmed flight, in which the helicopter makes a rectilinear acceleration, and the more complex transient maneuver flight, in which the helicopter makes a non-rectilinear acceleration and so the rotor interactions are no longer strictly periodic and have a more complex time dependence. Bres et al [23] attempted a similar modification to WOPWOP and developed a more robust version they named PSU-WOPWOP. This uses a source time implementation of Farassat's formulation 1A [34]. Further modification of the PSU-WOPWOP code came from Chen et al [25] and was termed GENHEL-PSU-WOPWOP. This incorporates a flight dynamics simulator maintained by NASA for a generic utility helicopter and incorporates it into the PSU-WOPWOP noise prediction code. Chen et al. [25] shows excellent real-time dynamic sound predictions however their prediction method focuses on loading and thickness noise from the blade passage and neglects any time-dependant interactions between turbulence generating events and the rotor blade such as Blade Vortex/Wake Interactions (BVI/BWI's). Thus this code is limited to flight conditions in which there is no significant atmospheric turbulence and the maneuvers are not dominated by BVI's.

The above prediction methods fail to capture the physics of some of the more fundamental interactions between rotors and turbulence. The aim of this paper is to present results for a far more scientifically fundamental case in which a wall mounted rotor immersed in a turbulent boundary layer ingests a stochastic, non-stationary gust/transient disturbance. Investigations of these interactions becomes important when developing models for the transient sound prediction and a robust experimental database is necessary to inform these models. This paper will identify types of noise radiated by a rotor at different points during a transient and attempt to make links between the rotor noise and the ingested flow. It will aim to show that the noise generated by the unsteady transient disturbance is a result of unsteady behaviour in the disturbance generator and that the balance of the noise response from the rotor is related to the phase-locked deterministic components.

6.4.2 Experimental Investigations of Turbulence Ingestion Noise

Experiments were performed using the simplified rotor design of Sevik [79], designed for high acoustic signal to noise ratio. This design was first used by Sevik in his 1973 paper to examine the far field noise generated by the ingestion of grid generated turbulence. The results showed significant humps in the broadband sound centered on the blade passage frequency and its multiples. These humps occur as coherent turbulent structures are ingested into the rotor. The correlation between each blade cutting the same structure produces a coherent rotor response and an increase in the spectral energy close to the blade passage frequency. Alexander et al ([4], [3]), Murray et al. [71], and Wisda et al. [86] investigated a number of flow permutations for ingestion into the Sevik rotor. They measured the sound radiated by the Sevik rotor ingesting a thick turbulent boundary layer as well as taking hotwire anemometry measurements in the blade frame of reference [4]. Observations of the turbulent inflow coherence between consecutive blade tips showed that the turbulence distortion did not undergo significant lateral contraction as it was ingested, agreeing with the previous conclusions from [3]. Below an advance ratio of 0.79 a flow reversal phenomena was identified. The thrust of the rotor was sufficient to cause flow separation from the wall and standing arch vortices were identified in instantaneous PIV images of the flow in the tip gap. This flow reversal is thought to be the same phenomena identified by Huse [49] as a propeller hull vortex generated by a rotor operating at high thrust near a ship hull. Predictions for the radiated noise using both rapid distortion theory in [3] and Glegg's time-domain approach (detailed in [39]) were performed. Both breakdown below this advance ratio as turbulence ingestion's influence on the radiated sound diminishes in favour of the highly coherent propeller hull vortex. Murray built on the foundation set by Morton and Alexander by examining the dependence of the radiated sound on rotor yaw angle. They noted in [71] that there is significant asymmetry in the rotor inflow when the rotor disk is

yawed as well as there being significant effects on the radiated sound at different yaw angles. The trailing edge noise was more prominent in the case where the rotor was yawed. Murray measured the flow field in the tip gap using PIV for two advance ratios and identified the existence of two contra-rotating arch vortices[86]. Instantaneous images show that, even though the flow reversal is unsteady, the arch vortices are almost always present.

This paper extends the studies of Alexander et al. [3] and Murray et al. [71] and document the development, distortion, and interaction noise produced by the Sevik rotor ingesting a series of large-scale transient disturbances generated within a thick turbulent boundary layer. Our objective is to identify non-stationary phenomena in the sound field produced when an intense disturbance is encountered, and then to identify the precise turbulent motions that are responsible, and to reveal these effects as a function of the time-scale of the disturbance. Our aim is to quantify the relationship between the disturbance, its turbulence structure, and the sound produced through simultaneous measurements that are suitable for validating analytical predictions.

As discussed below, experiments were performed in the Virginia Tech Stability Wind Tunnel using a 457 mm diameter Sevik rotor ingesting a 98 mm thick planar turbulent boundary layer. Transient disturbances were generated using an airfoil placed 2.19 diameters upstream of the rotor extending from the wall to the rotor axis. Simultaneous time-resolved PIV at the rotor, in planes parallel to the boundary layer wall, and far-field sound measurements were used to reveal the flow structure and the sound produced. This paper will start with a description of the experimental setup, followed by a description of the coordinate system and details of the measurement procedures and equipment. The disturbance generator design and construction details as well as the characterization of the motions examined will be discussed. In the results section the sound signature of a disturbance ingested by the rotor will be investigated, mechanisms for the production of the sound signatures specific to the

flow field and rotor geometry will be proposed.

6.5 Experimental Methods

6.5.1 Experimental Wind Tunnel

The Virginia Tech Stability Wind Tunnel (VTSWT) in its semi-anechoic configuration is shown in plan view in figure 6.2. It consists of a test section enclosed by 0.6 m x 0.6 m Kevlar covered panels on the floor and ceiling, smooth 0.6 m x 0.6 m aluminum panels on its port wall and Kevlar on the starboard wall. The test section is 1.85 x 1.85m x 7.32m in size. The kevlar covered panels are placed on the floor and ceiling and foam wedges placed between the Kevlar covered panels and the test section exterior to reduce noise reflections. An anechoic chamber located on the starboard side of the test section with dimensions 6 m x 2.8 m x 4.2 contains a 251 microphone phased array. To ensure a turbulent flow along the test section walls a trip strip is located 3.58 m upstream of the entrance of the test section. The free stream velocity was kept constant at 20.6 $\pm$0.2 m/s. This corresponds to a freestream Reynolds number of 576 300 $\pm$48000, based on the rotor diameter with a reference length of 457.2 mm. The free stream turbulence levels associated with the tunnel are less than 0.01% at 20 m/s and the mean flow has a freestream uniformity of 0.5% at 47 m/s [30].

6.5.2 Coordinate System and Measurement Locations

The co-ordinate system used for the VTSWT experiments is a right handed system shown in figure 6.2 with the origin on the port wall at the furthest upstream wall panel. Figure 6.2 is a top view of the test section. x is the streamwise co-ordinate and positive downstream

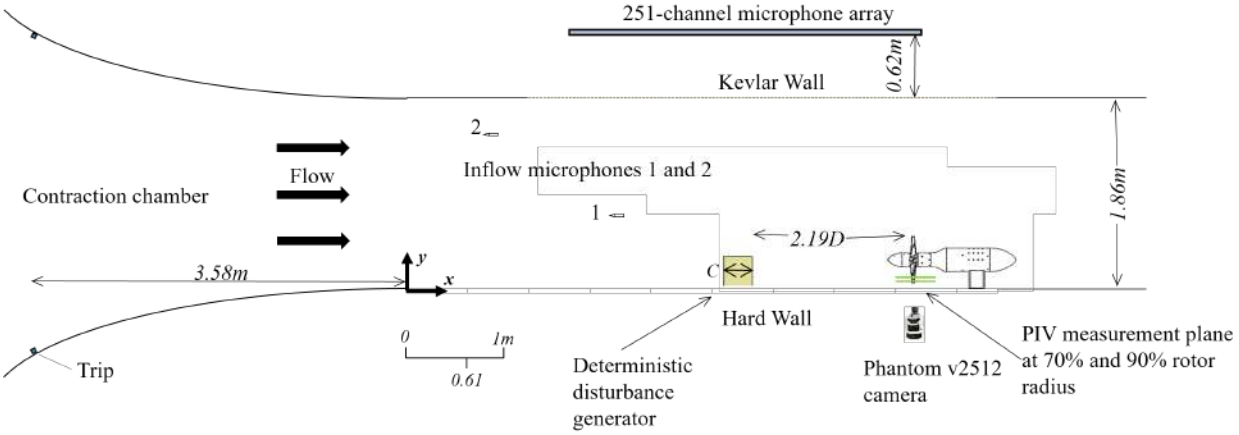

Figure 6.2: Schematic of the VTSWT test section showing the physical locations of the measurements made. The 251-channel AVEC array is shown in the starboard chamber. The particle image velocimetry measurement planes at 70% and 90% rotor radius is shown. Inflow microphones are denoted by 1, and 2.

(to the right in figure 6.2), y is the spanwise component perpendicular to the port wall and away from the wall, and z is the component parallel to the port wall to complete the right-handed coordinate system. The various instrumentation and models used in this experiment are described in further sections and what follows is a summary of figure 6.2. A rotor is placed on the port wall of the test section at mid-span ($y = 0$ m) 5.08 m downstream of the test section entrance ($x = 5.08$ m). The rotor is positioned such that the rotor blade tips are 20 mm from the wall at bottom dead center and the mid chord line is at y=0. The blades are immersed in the boundary layer up to 34% of the rotor radius. The disturbance generator quarter chord is located 2.19 rotor diameters upstream of the rotor midplane at (x,y,z)=(4,0,0) m and has a chord length of 152.4 mm. A 251 microphone phased array located $z = 2.22$ m from the rotor centerline in the starboard anechoic chamber is used to measure far field acoustics and beam form noise sources. Additional inflow microphones are located as identified in figure 6.2 and their precise locations are given in Section 6.5.5. Time resolved planar particle image velocimetry is taken parallel to the port wall at $y = 43$ mm and $y = 89$ mm. This corresponds to 90% and 70% of the rotor radius respectively when the

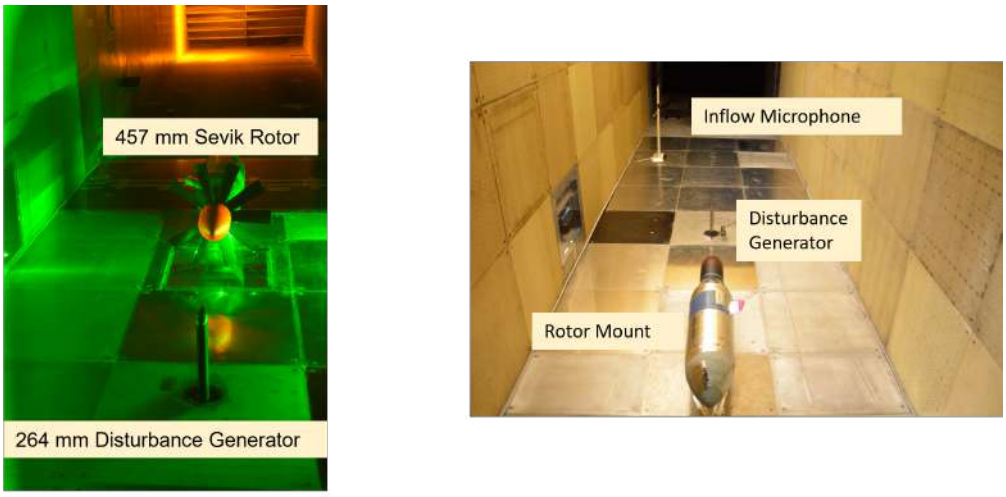

Figure 6.3: Experimental photos taken looking a) downstream (port hard wall on the right) showing the location of the 264 mm Disturbance Generator (DG), the optical PIV panels, and the 457.2 mm Sevik Rotor, and b) upstream (port hard wall on the left) showing the Sevik Rotor Mount (without the rotor mounted), DG, and Inflow Microphone.

rotor blade is in the bottom dead center position. The mean surface pressure distribution along the port wall panels is taken at intervals of approximately 100 mm to quantify the boundary conditions and pressure gradient of the flow. Boundary layer profiles are taken using a pitot tube rake at mid-span at 3 streamwise locations (x=1.48 m, 2.69 m, and 4.52 m) with no disturbance generator or rotor installed.

6.5.3 Rotor

The Sevik rotor is a scaled model (2.25) of the original Sevik rotor used in [79]. It has 10 constant chord blades with a chord length of 57.2 mm and a rotor diameter of 457.2 mm. figure 6.4 shows CAD of the rotor. The rotor consists of a 127 mm hub and the blades have a pitch angle that varies from 55.6°at the root to 21.2°at the tip. The rotor is driven by a Kollmorgen AKM-64P-ACCNDA00 servo-motor powered by an S61200 servo-drive. The

minimum advance ratio, defined as the ratio of the freestream fluid velocity to the tip speed ($J = U_\infty/nD$), is 0.58 at 20 m/s based on the maximum shaft design speed of 5000 RPM. The zero thrust advance ratio is 1.44 and the design advance ratio is 1.17. The rotor was setup mid-span ($z = 0$) with the rotor center line at $y = 0.248$ m, resulting in a tip gap of 20 mm when the blades are in the bottom dead center position. The rotor was located towards the aft end of the test section at $x = 5.08$ m. Data was taken for a variety of advance ratios but only data taken at the design advance ratio (J=1.17) is presented in this paper.

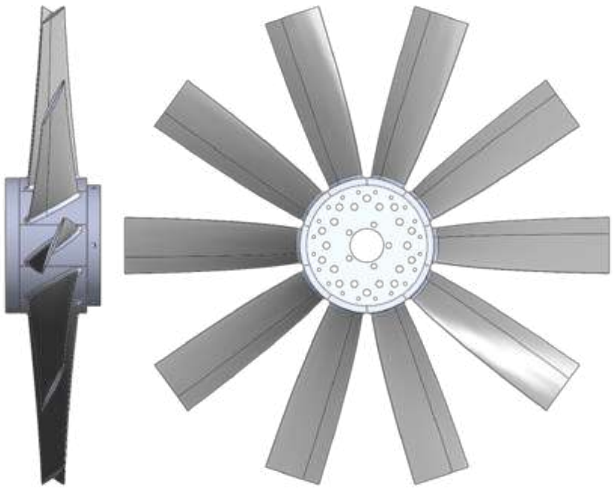

Figure 6.4: 457.2 mm 10-bladed Sevik rotor

The motor is located within a cylinder structure and the rotor is cantilever mounted to a shaft supported by two journal bearings. A nose cone of 216.4 mm length is attached to the front face of the rotor. The cylinder structure has a diameter of 219 mm at its widest point and 127 mm at its narrowest. It is welded to a 152.4 mm x 76.2 mm box beam that is in turn bolted to a structure mounted to the outside tunnel structure. The interface between the two cylinder sections and the box beam are faired to reduce aerodynamic noise however they both still contribute to an overall flow blockage of 1.5%. The rotor mid-chord is 512 mm upstream of the strut.

6.5.4 Pressure Measurements

To characterize the boundary layer a Vectoflow Pitot-probe rake was connected by 1.6 mm Tygon tubing to a DTC Initium ESP-32HD 32-channel 20" pressure scanner with a measurement uncertainty of 0.03%. The rake consisted of 30 pitot static probes arranged logarithmically with distance from the wall. The distance measured by the probes extends from $y = 0.5$ mm to 152.6 mm normal to the wall. Measurements for the boundary layer were taken at three streamwise locations along the centerline of the hardwall at $x = 1.48$ m, 2.69 m and 4.52 m.

In order to measure the pressure gradient experienced by the boundary layer along the test section wall 22 static pressure taps along the port wall center line were used. These pressure taps were connected to a pressure scanner in the same manner as the boundary layer rake. An Esterline 9816/98RK pressure scanner with a 2.5 psi range and 0.05% uncertainty was used to record the mean wall pressure data.

6.5.5 Acoustic Measurements

The far field sound was measured in this test using two arrangements of microphones. The VTSWT is outfitted with a 251 microphone phased array in the starboard anechoic chamber used for beamforming. An additional two inflow microphones were installed in the flow to record the inflow acoustics. The phased microphone array consists of four interlocking spirals of 251 GRAS 40PH-S5 1/4" microphones with a sensitivity of 50 mv/Pa and a 32-135 dB (A) dynamic range. The microphones acquired data at 51 200 Hz. The center of the array is located 3.46 m downstream of the origin, 0.054 m beneath the mid-plane of the test section and 2.53 m away from the port wall.

The inflow microphones are 1/2" Bruel & Kjaer 4190 located as shown in figure 6.2. Inflow

microphone 1 is mounted on the port wall, 1.53 m above the floor. It is 3.13 m away from the rotor with a directivity angle of 15°. Inflow microphone 2 is mounted on the floor upstream of the rotor towards the starboard side of the tunnel. It is 4.5 m away from the rotor with a directivity angle of 17°. Both microphones were fitted with UA0386 bullet nose caps and mounted using specially manufactured stands that are aerodynamically faired to reduce noise. The microphones acquired data at 65 536 Hz. Figure 6.5 shows the beamforming array and figure 6.6 shows the wall mounted in-flow microphone.

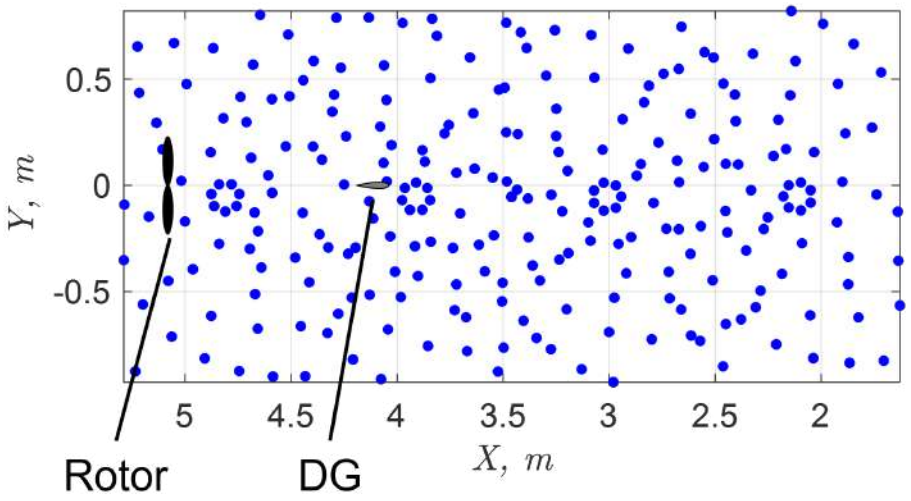

Figure 6.5: Schematic of key components seen from the starboard side. Microphones are labeled in blue markers.

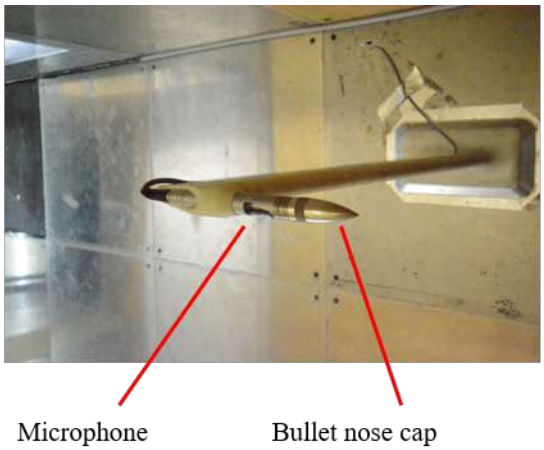

Figure 6.6: Bruel & Kjaer 4190 half-inch microphones with Bruel & Kjaer UA 0386 bullet nose cone.

6.5.6 Particle Image Velocimetry Measurements

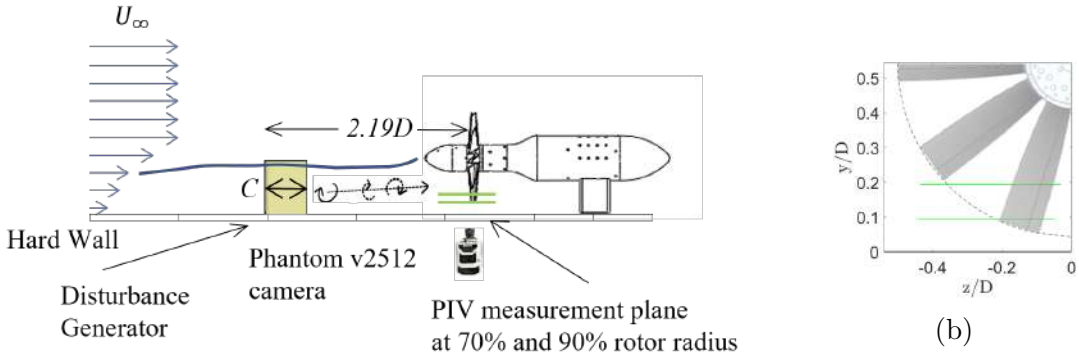

(a) (b)

Figure 6.7: A schematic of the experimental configuration for PIV acquisition is shown in a). Measurements were taken at 70% and 90% of the rotor radius parallel to the test section walls. b) shows the extent and location of the measurement planes relative to the rotor blade position.

Time resolved planar particle image velocimetry (PIV) was taken at two wall parallel planes located at the rotor 90% radius (43 mm from the port wall) and the rotor 70% radius (89 mm from the wall). The experimental setup is shown schematically in figure 6.7. The plane was imaged below the rotor in order to capture the disturbance as it passes through the rotor

plane. The measured field of view is 258 x 141 mm with a spatial resolution of 3.76 mm and the measurement was taken at a sampling rate of 4 kHz. In order to capture the phase averaged nature of the transient generated by the disturbance generator, multiple realizations of the flow were taken with the PIV recording triggered a square wave signal given when the actuator begins motion. This allowed multiple realizations of the flow, acoustics, and pressure to be recorded in a synchronized manner. The light sheet is illuminated using a Photonics Industries Nd:YAG dual cavity laser emitting 532 nm light and is approximately 2 mm thick. The laser sheet is shown in figure 6.8a and is shone in the direction of positive z parallel to the port wall while the camera is directed normal to the laser sheet looking from the port chamber. The camera used to image the flow was a Phantom v2512 recording in double frame mode with a Canon 200 mm lens. Figure 6.8 shows the PIV setup in the test section. Camera calibration and laser sheet alignment were completed using a Lavision 106-10 3-dimensional calibration plate.

6.5.7 Disturbance Generator

Disturbance Generator Design

The Disturbance Generator (DG) utilized in the study comprises a NACA 0021 airfoil with a 148 mm chord. The airfoil span of 255.65 mm was chosen to place its tip directly upstream of the rotor axis and minimize any noise generated by the tip vortex and associated flow structure. The DG was mounted with its span perpendicular to the wall. The side of the airfoil exposed to the flow was covered with an airfoil wing tip to minimize any effects caused by aerodynamic drag. The wing tip was created using the half-body revolution of the NACA 0021 profile along its chord and had a half-thickness of 15.24 mm.

With reference to the tunnel coordinate system, the quarter chord of the DG is positioned

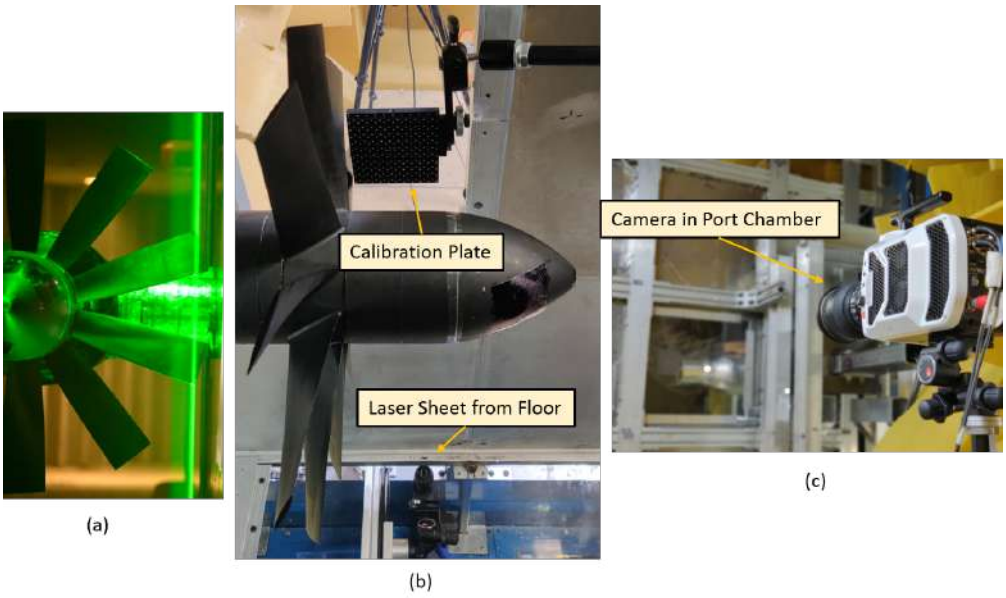

Figure 6.8: Experimental pictures illustrating the PIV setup in the VTSWT. a) looking downstream showing the Sevik rotor with the laser sheet at 90% radius b) looking towards the port wall from inside the test section showing the location of the calibration plate and laser sheet c) looking towards the port wall from inside the port chamber showing the position of the camera.

at (x,y,z)=(4, 0, 0) m. Additionally, the DG is placed 1.08 m upstream with respect to the rotor plane, which translates to approximately seven chord lengths of the DG. At 0^o angle of attack, the trailing edge of the DG is located at z=0 m and is aligned with the center of the rotor face.

Details of the disturbance generator design and motion calibration are given in Palanganda [74].

Mean Disturbance Generator Motions

Table 6.1 presents the statistics, non-dimensionalized time, and pitch rates associated with all motions where C is the chord length for the disturbance generator and D is the rotor diameter. The freestream velocity for all measurements was kept constant at $U_\infty = 20.6 \pm 0.2$

m/s. The airfoil displacement was measured by an externally mounted laser displacement sensor. Each actuation was measured and the resultant mean angular displacement and standard deviation are shown in figure 6.9. Actuation time (AT) represents the time the DG takes to complete its prescribed motion. For the flap motion, the DG was actuated from its steady state of 0° to its maximum angular displacement of 20° and back with the same pitch rate. For the ramp motion, the DG was actuated from 0° to 20° while holding its peak position for a dwell time of 2s before decelerating slowly back to its mean position.

Table 6.1: Calculated statistics and non dimensional pitch rates for the motions.

Motion	Notation	Number of Actuations	Mean AT	ND Pitch Rate	ND Time		Nominal Length-scale
			(M_{AT}, s)	$\dot{\alpha}C/2U_\infty(^o)$	$U_\infty T_{act}/C$	$U_\infty T_{act}/D$	$U_\infty T_{act}$
Flap	63 ms	282	0.063	2.35	8.5	2.8	1.3
	151 ms	292	0.151	0.98	20.4	6.8	3.11
Ramp	37 ms	198	0.037	2	5	1.7	0.76
	79 ms	276	0.079	0.94	1.7	3.6	1.63

Phase Alignment

To minimize the effect of uncertainty in the trigger setup on acoustic pressure, the pressure time history corresponding to each actuation was phase aligned on the rotor phase and the actuation phase. The motor encoder signal is a saw-tooth signal that repeats once per revolution, and the actuator outputs a square wave signal at the start of each actuation. The time reference of zero was defined as the mean of the time difference between the mid-point of the voltage rise in the actuator signal and the mid-point of the rising slope of the saw-tooth signal. By aligning the saw-tooth signals, it was obvious that the actuation timing has a certain degree of variation with the rotor phase. Therefore, the individual actuations that deviated from this zero reference by more than ±2.5% of the period of rotor rotation

were eliminated from acoustic data processing. The PIV data was aligned with the position of the actuator and no data points were excluded. While every effort was made to have the actuation begin at the same blade phase there was still a 5% uncertainty in the position of the blades.

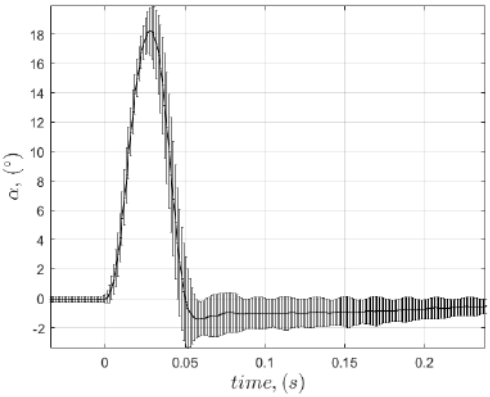

(a) 63 ms flap

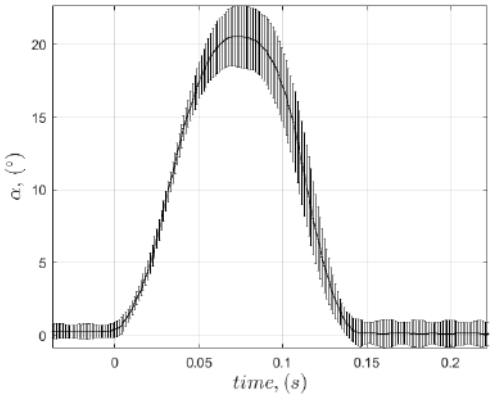

(b) 151 ms flap

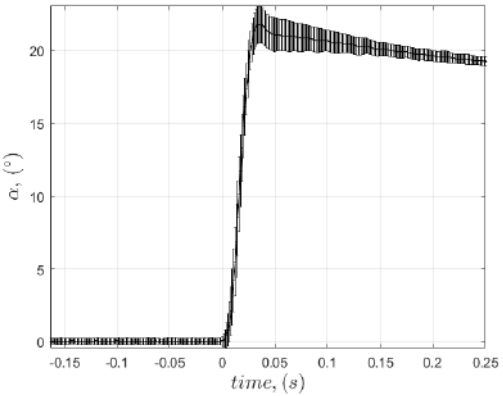

(c) 37 ms ramp

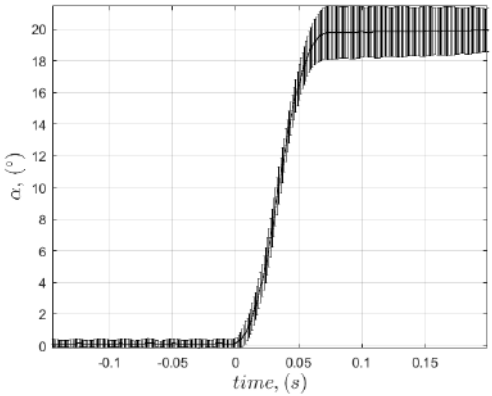

(d) 79 ms ramp

Figure 6.9: Mean angular displacement measurements for four DG motions.

6.6 Results

All measurements were taken at a constant free stream velocity of 20.6 ±0.2 m/s. This corresponds to a rotor diameter based freestream Reynolds number of 576 300 ±48000. The Reynolds number based on three different lengths, the rotor diameter, rotor blade chord and the disturbance generator chord are presented in Table 6.2.

Table 6.2: Various length based Reynolds numbers

Quantity	Re_D	Re_{BC}	Re_{DC}
Length Base	Rotor Diameter	Blade Chord	DG Chord
U_∞	20.6 m/s	20.6 m/s	20.6 m/s
ν	1.83e-5 m^2/s	1.83e-5 m^2/s	1.83e-5 m^2/s
Re	576 300 ±48000	72 100 ±6000	192 100 ±16000

While ten different motions were measured this paper will restrict its scope to the examination of only a few. The aim is to ensure that the motion investigated is fully unsteady while also being a realistic motion experienced by in service rotors. Thus the rationale for the investigated motion is to take the fastest motion available with acceptable acoustic results. Based on a preliminary examination of the results in the initial stages of the experiment it was determined that the motions of interest should be the 63 and 151 ms flap and the 37 and 79 ms ramp. However the fastest flap and ramp motions (63, and 37 ms respectively) had considerable mechanical noise contamination from the actuator assembly. To ensure a lightly thrusting rotor the advance ratio of interest is the design advance ratio of J=1.17. Therefore the focus of this paper will be on the 79 ms ramp and 151 ms flap's interaction with the rotor at an advance ratio of 1.17.

This section will begin with an examination of the pressure gradient and boundary layer properties of the ingested flow. It will then examine the quiescent flow with no rotor actuations before analyzing the flow and acoustics seen during the transient. A sound source mechanism is proposed for the sound measured during the transient as well as once the

flow has settled to a steady state. Finally a reconstruction of the flow and sound is done using quasi-steady measurements that serve to determine the extent to which the motion is unsteady.

6.6.1 Pressure Gradient and Boundary Layer Growth

Measurements of the wall mean pressure at $z = 0$ along the length of the test section were taken for advance ratios between zero thrust (J=1.44) and highly thrusting (J=0.58) and are shown in figure 6.10a. These data were taken without the disturbance generator installed and show a near zero pressure gradient along the length of the test section with a strong decrease in the C_p near the rotor plane that increases with increasing thrust. Boundary layer profiles were taken at varying points along the test section port wall with the rotor and disturbance generator removed to capture the evolution of the boundary layer along the test section wall. These profiles are shown in figure 6.10b and as the boundary layer grows along the wall the velocity profiles become more full and the boundary layer thickens. By the time the boundary layer reaches the rotor it is approximately 98 mm thick. Figure 6.10a demonstrates the increasing favourable pressure gradient in the rotor near field as a result of the rotor thrust. In general this pressure gradient should act to reduce the thickness of the boundary layer as it is ingested however, for the chosen advance ratio of $J = 1.17$ the pressure gradient change appears minimal and the boundary layer thickness is likely to remain within a few mm of the measured boundary layer in figure 6.10b. The % of the rotor radius embedded in the boundary layer is then approximately 34% at bottom dead center of the rotor rotation. The PIV measurement planes are taken at 43 mm and 89 mm from the wall for 90% radius and 70% radius respectively.

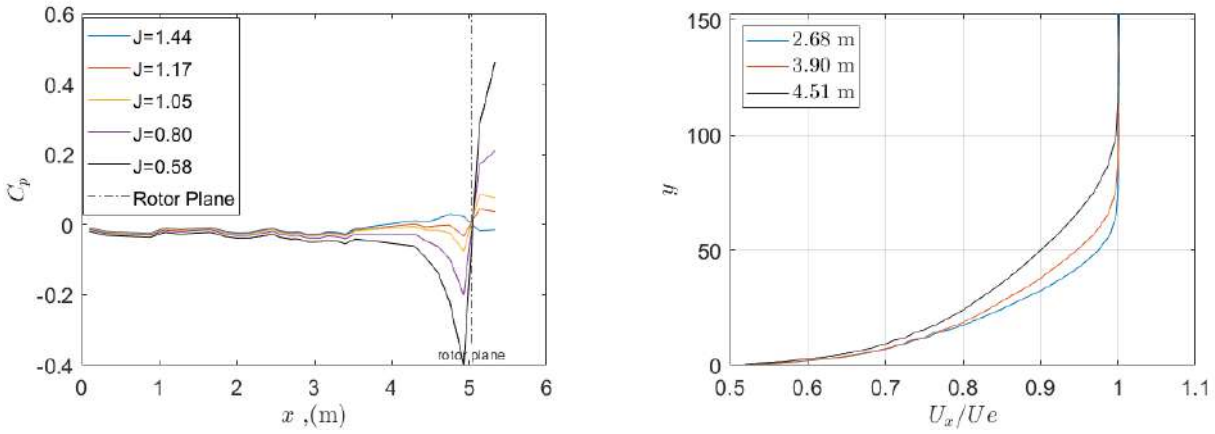

(a) (b)

Figure 6.10: Mean pressure measurements and boundary layer profiles taken along the port wall. a) shows the static pressure on the wall b) shows the boundary layer profile at 3 streamwise locations with the velocity normalized on the edge velocity.

Table 6.3: Boundary layer properties measured without the rotor and DG installed

Location (m)	Displacement Thickness δ^* (mm)	Momentum Thickness θ (mm)	Shape Factor H
1.48 m	8.18	6.32	1.29
2.69 m	9.30	7.28	1.28
4.52 m	12.53	9.75	1.29

6.6.2 Flow Velocimetry in the Rotor Near Field

PIV measurements of the undisturbed flow (no actuation) in the vicinity of the rotor serve as a baseline for comparison with measurements of the disturbance. This informs our understanding of the background turbulence and mean flow within the boundary layer. PIV data were taken for 2.5s at a rotor advance ratio of J=1.17 with a sampling frequency of 4 kHz. This resulted in 107 images per rotor rotation and 94 rotor rotations over the course of the measurement. Each image then corresponds to 3.37°of shaft rotation. The data were averaged for each blade position (or phase) providing 94 averages of 107 blade positions. Figure 6.11 is constructed using the phase averaged velocity quantities at a profile 0.2 diameters

upstream of the rotor plane for the quiescent condition (ie DG at 0°and no actuation). The solid lines show the path of the rotor mid-chord through the PIV plane and their location relative to the flow contours is determined using Taylor's frozen flow hypothesis. Profiles were extracted from the PIV and then contours of the velocity and turbulence shown with rotor phase angle ϕ on the horizontal axis and vertical space on the vertical axis. The resultant contours show little to no phase dependence of the velocities or turbulence indicating that the rotor has no effect on either quantity this far upstream. Contours taken closer to the rotor plane at 0.03 diameters upstream are shown in figure 6.12. The effect of the rotor thrust as each blade passes through the measurement plane is seen. The blade decelerates the flow in the streamwise direction just prior to its passage and accelerates it as it is passing. In the spanwise direction the velocity is accelerated upwards in the spanwise direction with each blade passage. These are clear indicators of rotor phase dependence however there is no evidence of phase dependence in the turbulence contours. Turbulence levels vary but the average value tends to be around 4 to 6 x $10^{-3}U_\infty^2$ which is consistent with typical turbulent boundary layer turbulence levels at this location within the boundary layer. This measurement plane is located 42.8 mm away from the wall, placing it in a region with a mean velocity around $0.85U_e$ as seen in figure 6.10b. The average U_x/U_∞ in figure 6.11 is around 0.85 agreeing with the boundary layer rake data.

6.6.3 Quasi-Steady Results

To show the effect of the unsteady flow on the rotor noise, PIV and microphone measurements were taken at stationary disturbance generator angles of attack. Comparison between the stationary angles of attack with the transient data should reveal the extent to which the motion investigated here is quasi-steady. The acoustic measurements were taken at disturbance generator angles of attack ranging from 0^o to 20^o in angle of attack increments

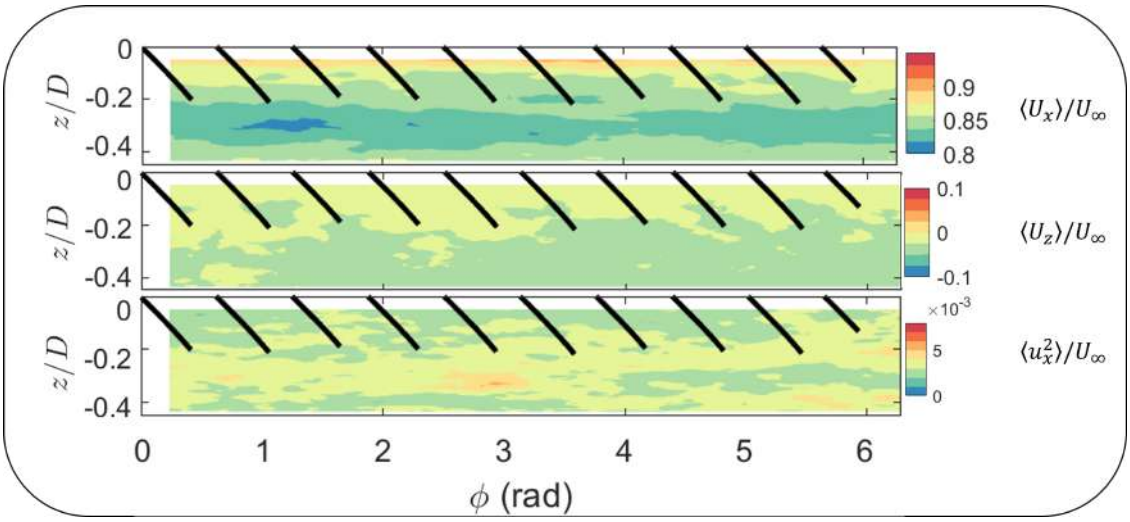

Figure 6.11: Phase averaged velocity field obtained from PIV images 0.2D upstream of the rotor plane plotted against rotor rotation phase for 1 revolution of the rotor ($\phi = 2\pi$).

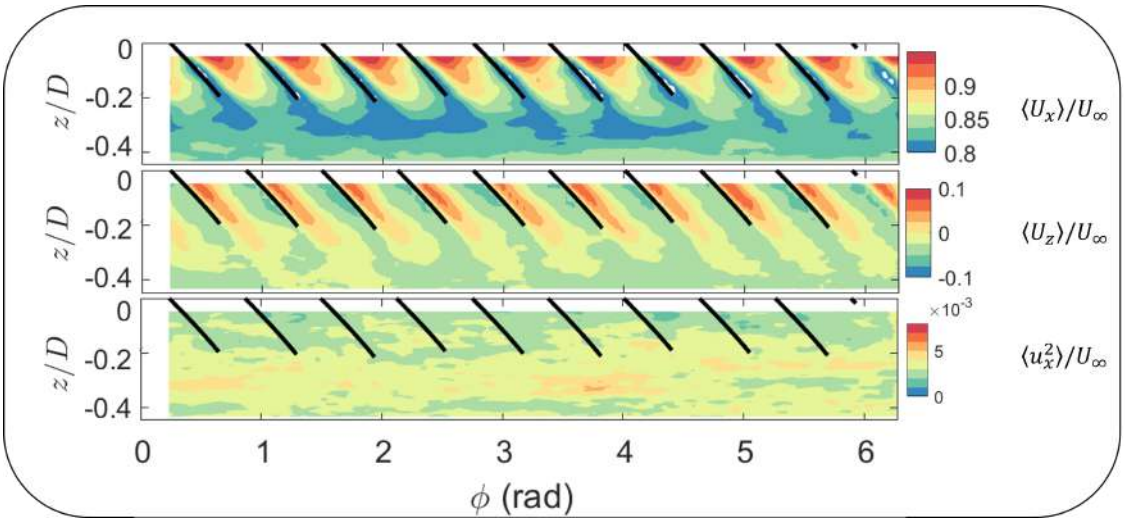

Figure 6.12: Phase averaged velocity field obtained from PIV images 0.03D upstream of the rotor plane plotted against rotor rotation phase for 1 revolution of the rotor ($\phi = 2\pi$).The black lines show the position of the rotor for each blade passage.

of 2^o while the PIV measurements were taken in increments of 4^o. The data investigated will be the overall spectra of the sound for each angle of attack, followed by a quasi-steady reconstruction of the disturbance flow using PIV data, and a quasi-steady reconstruction of the spectrograms using the stationary acoustic data. For both the acoustic and flow recon-

struction a convection velocity equal to the mean velocity at 43 mm was used and the data then time shifted by the distance between the disturbance generator trailing edge and the rotor plane, $(x_{rotor} - x_{TE})$, divided by the convection velocity, $U_c = 0.85U_\infty$. The quasi-steady reconstructions will be compared to the deterministic and stochastic portions of the acoustics and the extent to which each component is quasi-steady will be theorized.

The quasi-steady reconstruction of the flow from the steady angle of attack PIV measurements is presented in figure 6.13. From top to bottom are the streamwise fluctuations, flow angle, and mean flow in the streamwise and transverse directions. These data were extracted from a profile of the mean velocity and streamwise fluctuations taken $0.2D$ upstream of the rotor. The angle of attack of the disturbance generator, time shifted by the convection velocity, is shown in blue on each figure such that the angle of attack matches the velocity data at its location. Perhaps the most critical point in this reconstruction is noting the angle of attack that separation over the disturbance generator occurs. It is quite clear from examination of the mean velocities and flow angle that separation occurs where the flow angle stops increasing between 14^o and 16^o angle of attack. The flow is gradually deflected downwards for the first 14^o, from $\overline{\alpha}_{flow} = 0^o$ to -6.6^o. Above 14^o the angle of the flow makes a jump from -6^o to around -2.5^o and stays there for the remainder of the airfoil positions. This behaviour is consistent with separation off the suction side of the airfoil. Significant differences and some surprising similarities between the unsteady, and quasi-steady flow fields can be seen. Firstly with comparison to figure 6.20a the initial decrease in turbulence is remarkably similar to that seen 43 mm from the wall. Following that an increase in turbulence due to airfoil separation is seen at $U_\infty\tau/D$=3.15 for the quasi-steady reconstruction and around $U_\infty\tau/D$=4.5 in the unsteady flow field. As noted in the previous section the increase in the probabilistic spectra is more associated with the turbulence increase in the outer region of the boundary layer (at 89 mm away from the wall) and this turbulence is only evident in

the unsteady flow field after 150 ms. While there were no measurements for static angles of attack in 89 mm (an experimental oversight) it can be inferred that the flow remains attached for longer, as the turbulence onset is delayed compared to the measurements 43 mm from the wall.

The spectra of each angle of attack is shown in figure 6.14. The 0^o disturbance generator is shown in blue and the color gradient gradually moves from blue to red as the angle of attack increases to 20^o. The character of the acoustic spectra changes varies throughout the angle sweep. For low disturbance generator angles of attack, between 0^o and 6^o the first harmonic is humplike, consistent with the spectral shape associated with turbulence ingestion noise. Above 6^o angle of attack, when the flow deflection from the disturbance generator becomes significant, the first harmonic sharpens and appears nearly tonal by the time the angle of attack reaches 14^o. Above 14^o the broadband noise increases by about 5-8 dB and the first blade passage haystack returns to a more traditional haystack in appearance. It is clear that for different disturbance generator angles of attack, different types of noise types are displayed in the spectra. For low angles of attack the sound is dominated by the turbulence ingestion noise of the boundary layer. For medium angles of attack, between 6^o and 14^o, the blade has strong coherence between blade passages and the sound is likely generated by unsteady loading as the blade angle of attack changes during its passage through the flow deflection. Above 14^o the flow has separated off the disturbance generator and the turbulent kinetic energy the rotor is ingesting increases dramatically. This acts to radiate significantly increased broadband sound. The flow data shown in figure 6.13 supports this interpretation. Below 6^o angle of attack the flow angle is negligible ($< 2^o$), between 6^o and 14^o angle of attack the flow angle becomes significant ($> 5^o$), and above 14^o angle of attack the flow angle returns to negligible values and turbulence levels are drastically increased due to the flow separation.

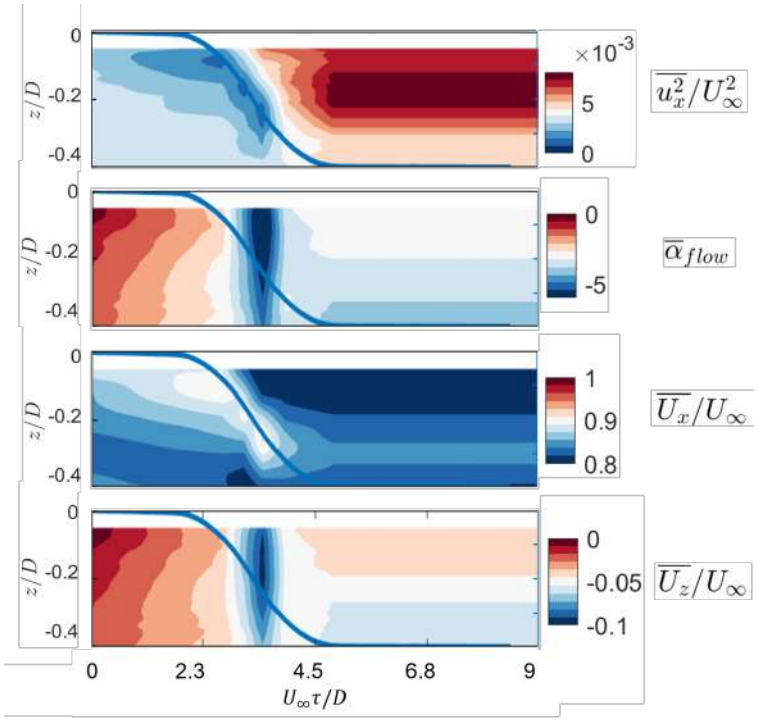

Figure 6.13: Quasi-steady flow reconstruction of the disturbance. The top plot shows contours of $\langle u_x^2 \rangle / U_\infty^2$ and the bottom plot shows the flow angle $\langle \alpha_{flow} \rangle = \tan^{-1}(\langle U_z \rangle / \langle U_x \rangle)$. The average angle of attack of the disturbance generator is plotted in blue over the top of each contour plot.

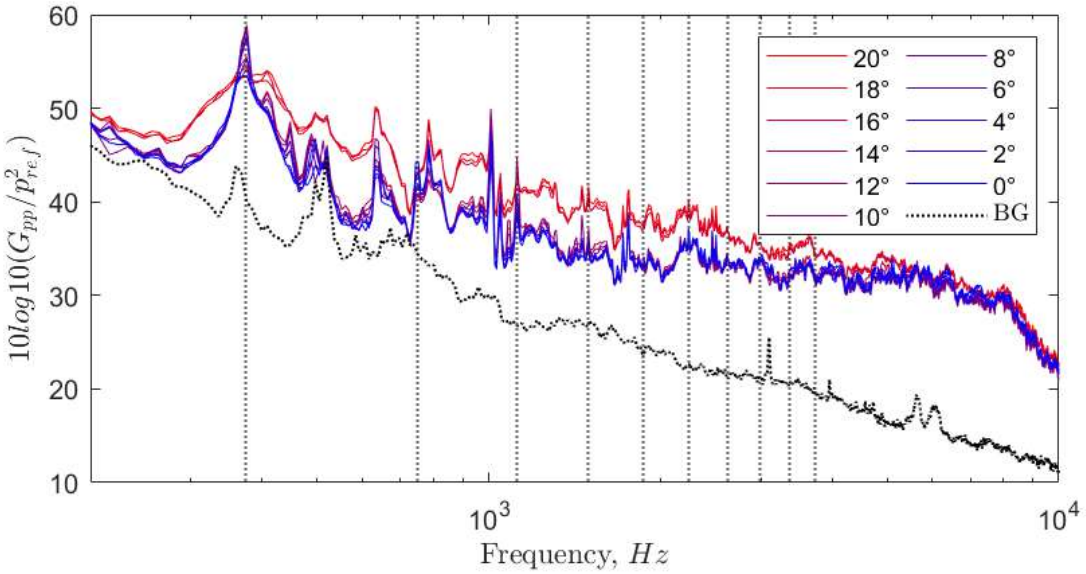

Figure 6.14: Spectra of the stationary angles of attack. The angle of attack varies from 0^o to 20^o in increments of 2^o and is indicated by the line colors varying from blue to red as the angle of attack increases.

The reconstruction of the quasi-steady spectrogram is shown in figure 6.15. The reconstructed quasi-steady spectrogram appears to show the noise increase by around 10 dB at $U_\infty \tau/D$=3.6. We know that the majority of the sound increase from the steady disturbance generator angle of attack occurs when flow over the disturbance generator airfoil is separated, thereby increasing the turbulence ingested into the rotor. Thus, for the quasi-steady motion, it should be expected that the increase in turbulence and sound occurs around the time when the airfoil reaches the critical angle of attack of 14^o. Including the convection time of the flow and sound propagation time to the microphone results in the noise increase occurring at 3.6 $U_\infty \tau/D$ after the actuator begins its motion. However, from the transient analysis in the previous section (see figure 6.20a), the increase in the sound pressure due to turbulence ingestion occurs at approximately 6.8 $U_\infty \tau/D$ after the actuator begins its motion. Quite clearly there is a significant delay between the onset of the turbulence ingestion noise in the transient when compared to the quasi-steady reconstruction which indicates that both the

flow and the noise generated as a result of the transient motion are unsteady in nature.

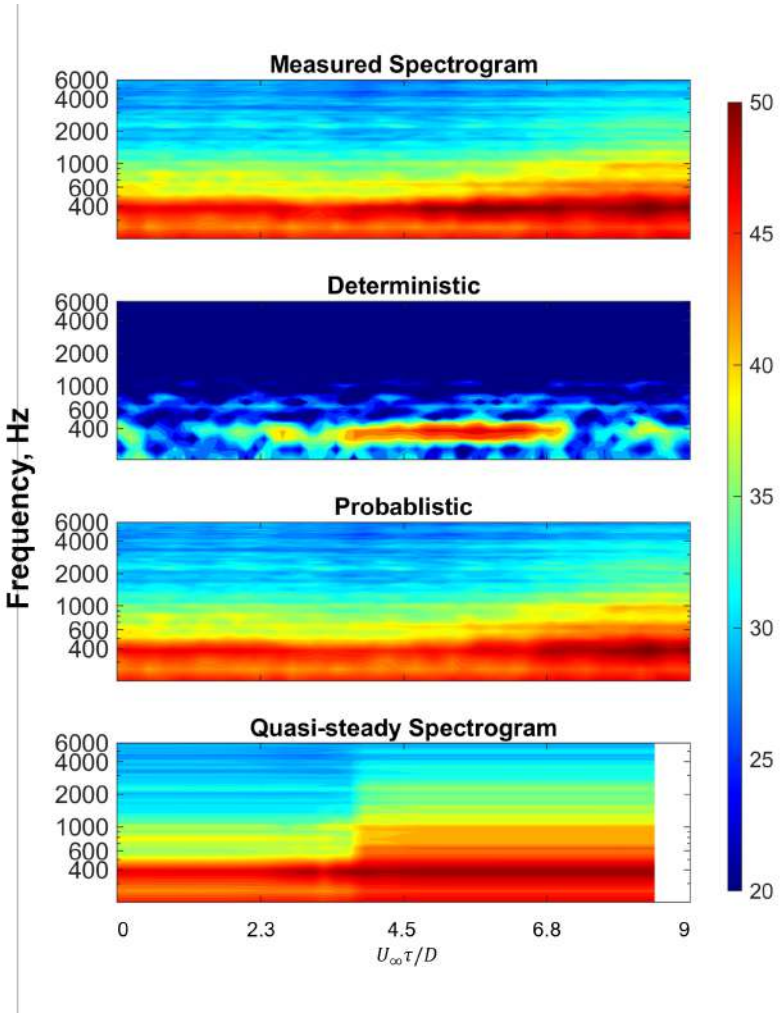

Figure 6.15: Spectrogram of the measured sound signal, the deterministic component of the sound signal, the probabalistic/stochastic portion, and the reconstructed quasi-steady spectrogram.

6.6.4 Transient Ingestion Results

In this section a discussion of the disturbance as well as the resulting acoustics for the 79 ms ramp and possible explanations of the responses using the flow data will be conducted. To evaluate the sound produced by the rotor both in a quiescent environment as well as during

the ingestion of the transient disturbance acoustic sound pressure data from microphone 1 will be analysed. This microphone position is shown in figure 6.2 and is mounted on the port wall at (x,y,z)=(2, 0.786, 0.587) m. With respect to the rotor these coordinates correspond to 3.08 m upstream of the rotor disc, 0.538 m away from the rotor axis in the positive y direction, and 0.587 m offset from the rotor axis in the positive z direction. Comparisons between the phase aligned velocity and acoustic measurements will be made. The pressure signal was broken down into two components termed the deterministic and probabilistic components. The deterministic component is the phase averaged pressure and is calculated by phase aligning the acoustic measurements with the actuator signal and taking the phase average of these measurements. This results in a transient pressure time history that consists of 105 repetitions for each actuator position. The pressure is then converted into a spectrogram by taking the fast Fourier transform of the pressure signal and averaging over all measurements. The probabilistic component is calculated by taking the difference between the instantanous pressure and phase averaged pressure and then averaging the mean square of the pressure fluctuations and generating a spectrogram in the same fashion as described for the deterministic component. For comparisons between the flow and rotor interaction and the resultant acoustics the velocity at a profile 0.2 diameters upstream of the rotor is taken. This location was taken as it was determined to be the closest point to the rotor with minimal rotor thrust effects on the resultant velocity. The transient convection time is accounted for by shifting the resultant profiles by $0.2D/\overline{U_x}$. This was done to obtain a more accurate source time for the acoustic comparison and makes the assumption that the disturbance is convected at the mean velocity at the location of the PIV plane which, for small distances, is an appropriate assumption. The velocity quantities examined are the phase averaged velocities in the streamwise (x) and transverse (z) directions less the corresponding mean for the undisturbed profile in figure 6.17a and 6.17b. The turbulent fluctuations in the streamwise direction are calculated by taking the instantaneous velocity

at each phase and subtracting the corresponding phase average and then computing the mean square of that quantity. The rotor path through the disturbance is shown by the black lines on each plot. This position is calculated by taking the position of the centerchord of the rotor and calculating its path through a vertical plane intersecting the 70% and 90% radius when the blade is perpendicular to the wall/floor. These lines appear mostly straight however are curved as the pass through the plane.

Disturbance Characteristics

Prior to inferring acoustic sources an examination of how the disturbance evolves over time prior to its interaction with the rotor is necessary. The phase averaged components are shown in figure 6.16 as described in the previous section. $\tau = 0$ corresponds to when the DG begins its motion and the disturbance arrives at the rotor plane at approximately 2.3 $U_\infty \tau / D$. There is a downward sweep of velocity seen in figure 6.16a at both measurement locations that initially results in an increase in the streamwise velocity relative to the mean and is rapidly followed by a decrease in the relative streamwise velocity. Figure 6.16b shows the delay in separation in the outer edges of the boundary layer compared to the inner region. In the outer region (70%R) the turbulence increase occurs around 6.8 $U_\infty \tau / D$ while at the inner region, this occurs closer to 4.5 $U_\infty \tau / D$. The effects of the boundary layer turbulence on the vorticity are shown in figure 6.16c. The vorticity is demonstrated to be more concentrated by the disturbance near the outer edge (70%R) than in the inner regions of the boundary layer. This is due to the role the turbulent kinetic energy (TKE) plays on vorticity transport and diffusion. Within the boundary layer the TKE is significantly higher than at the boundary layer edges so the viscosity term in the vorticity transport equation $\nu \frac{\partial^2 \omega_i}{\partial x_j \partial x_j}$ strengthens and the vorticity induced by the airfoil trailing edge is diffused.

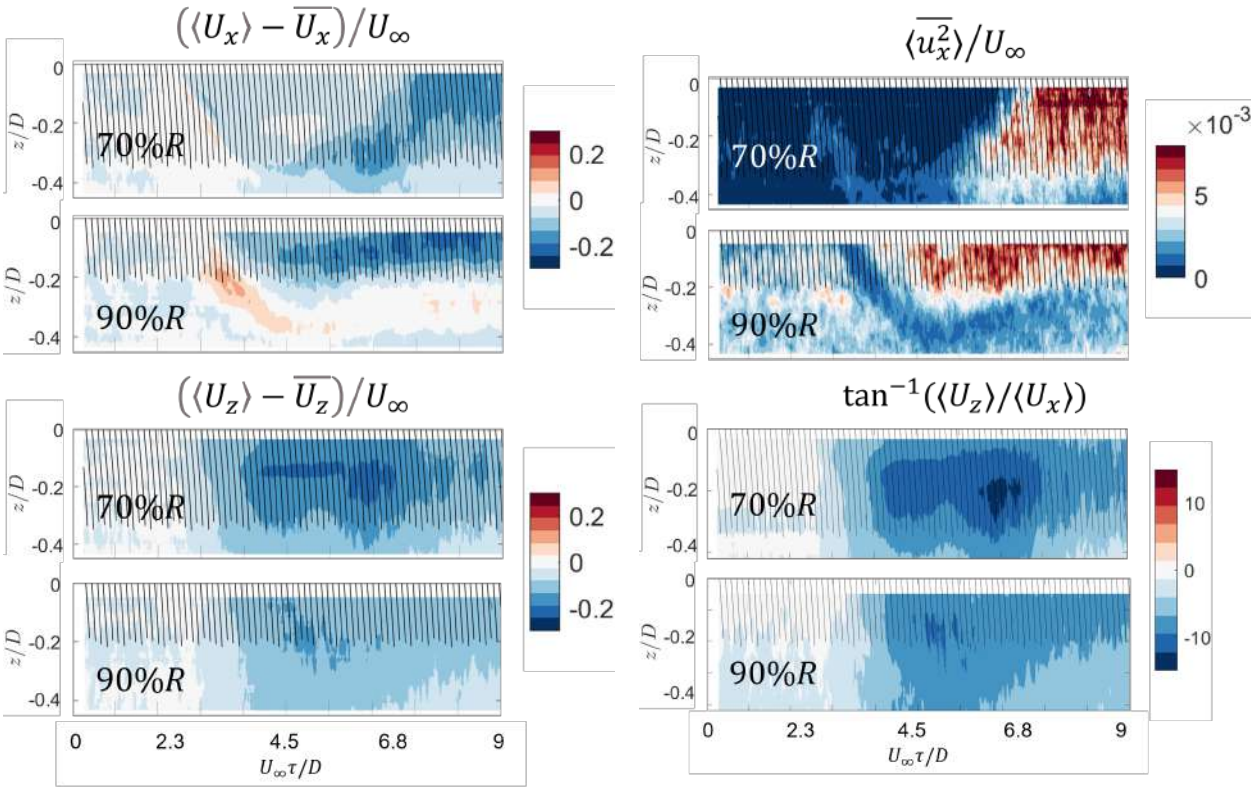

Figure 6.16: Contours of the phase averaged velocity components at a plane 0.2 diameters upstream of the rotor 43 mm from the wall (90%R) and 89 mm from the wall (70%R). (a) streamwise and transverse velocity, (b) streamwise normal stress and flow angle, (c) out of plane vorticity. The time axis is normalized on the freestream of the velocity and the rotor diameter. The black lines show where the rotor would cut the measurement plane.

Deterministic Pressure

We will begin the acoustic analyses by examining the deterministic pressure spectrum in figure 6.17. There appears to be a peak at the blade passage frequency. This peak is clearly evident as the disturbance passes through the rotor plane between $U_\infty \tau / D$=3.15 and 6.8. In an attempt to understand the source of the transient pressure peak we should examine the velocity data in Figures 6.17c, 6.17a, 6.17b. There does not appear to be a strong structural association between any component of the velocity, however if we examine the flow angle, defined as the angle of the flow relative to the freestream velocity vector, in figure 6.17c, the time at which the flow angle is most negative during the transient corresponds strongly to the time at which the deterministic pressure peaks at the blade fundamental frequency. To further understand the mechanism of the sound pressure increase the flow angle and velocities seen from the blade frame of reference is shown for each blade angular position in figure 6.18. The column on the left shows the flow angle, velocity in the streamwise direction (U_x), and velocity in the transverse direction (U_z) for the blade as it would cut through the disturbance. Each line seen tracks through the measurement plane at the centerchord of the blade. The deflection of the boundary layer by the disturbance generator is best visualized by examining the change in the U_z velocity. The spanwise motion of the disturbance generator deflects the flow in the negative z direction, changing the components of the velocity sampled by the blade as it rotates through the disturbance. This flow deflection induces a repeatable and easily determined variation in the blade angle of attack as it rotates through the disturbance. A varying angle of attack at that magnitude results in an unsteady force that repeats for every blade passage resulting in a peak in the phase averaged pressure at the blade passage frequency. This is known as loading noise and is caused by the variation of the compressive stress tensor over the blade surface. The second term in the Ffowcs-Williams and Hawkings

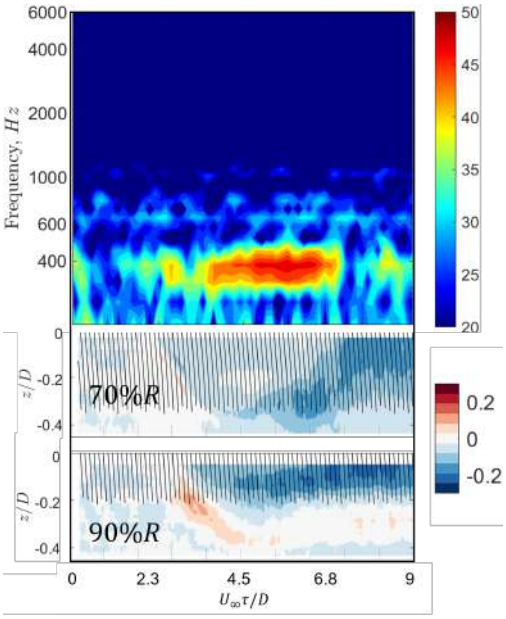

(a) $(\langle U_x \rangle - \overline{U_x})/U_\infty$

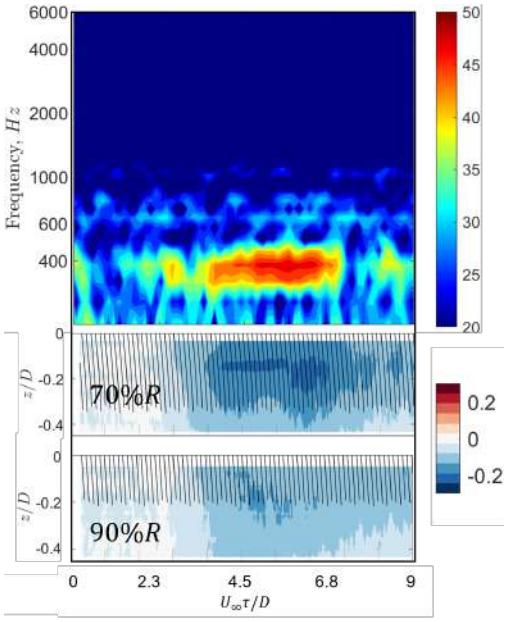

(b) $(\langle U_z \rangle - \overline{U_z})/U_\infty$

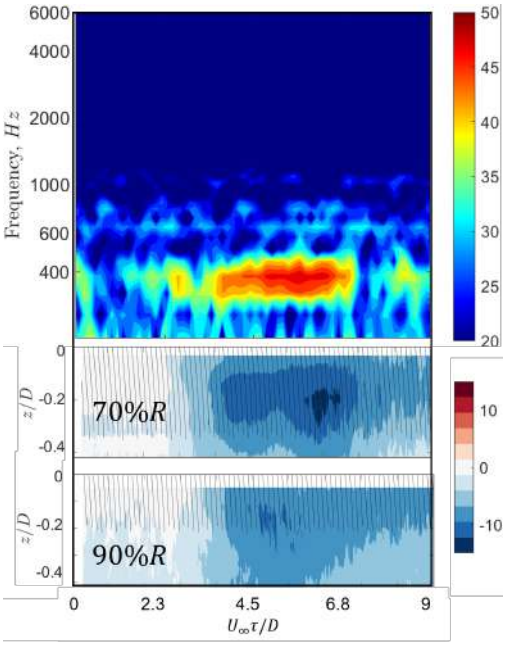

(c) α_{flow} $(^o)$

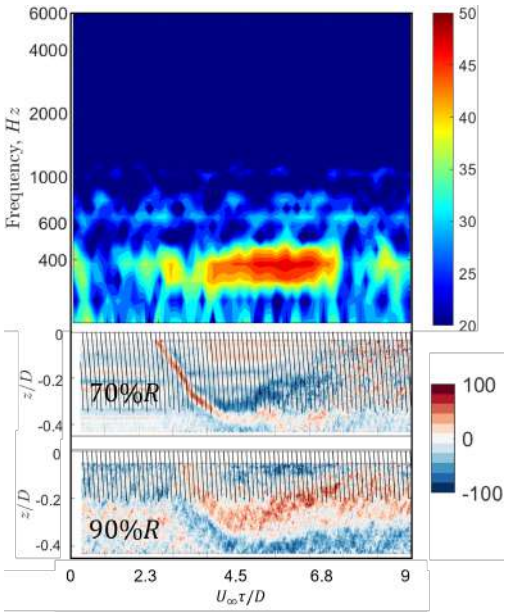

(d) ω (1/s)

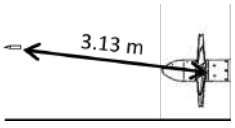

Figure 6.17: Contours of the deterministic part of the acoustic pressure signal compared to velocity measurements of the boundary layer 0.2 rotor diameters upstream of the rotor blade centerline. The location of the microphone for which this data is computed is shown relative to the rotor. The time axis is normalized on the freestream velocity and rotor diameter.

equation gives the noise as a result of this phenomenon and is shown in Equation 6.1 below,

$$p'(x,t)_{loading} = -\frac{\partial}{\partial x_i}\int_{S_0}\left[\frac{p_{ij}n_j}{4\pi r|1-M_r|}\right]_{\tau=\tau^*} dS(z) \tag{6.1}$$

This variation in angle of attack as the rotor cuts through the PIV plane is calculated in the following way. First the position of the mid chord of the blade was calculated as a function of the rotor phase, blade radius, rotational speed, and time. The following equation gives the position of the blade within the measurement plane.

$$z/D = 0.9R\tan\left(\phi_i + \frac{2\pi N}{60}\tau\right) \tag{6.2}$$

Then, knowing the position of the blade, z/D, as well as the amount of time that has elapsed since the DG began its motion, τ, allows the exact angle of attack the blade experiences to be calculated. This angle of attack, α_b, also depends on the blade section pitch angle and the rotor phase in the following way,

$$\alpha_b = \beta - (90 - \tan^{-1}\left(\frac{r(2\pi N/60) + U_z\cos(\phi)}{U_x}\right) \tag{6.3}$$

where β is the pitch angle and r is the distance along the blade from the rotor center line. This calculation is carried out throughout the ingestion of the disturbance into the rotor and illustrated in figure 6.19. Before the disturbance reaches the rotor plane, for non-dimensional times between 0 and 2.3 $U_\infty\tau/D$, the blade angle of attack as the blade passes through the measurement plane is consistently between 2 and 3 degrees at 90% radius and between 0 and 2 degrees at 70% radius. As the disturbance reaches the rotor plane and the flow angle changes significantly, the blade angle of attack changes.

Around 2.6 $U_\infty\tau/D$ the angle of attack of the blade jumps about a degree and then is

unsteady from the period that the disturbance is ingested until around 7.2 $U_\infty \tau / D$ where the flow has settled and becomes steady again. At 43 mm from the wall the blade angle of attack drops for each subsequent blade passage before increasing again to settle above the pre-disturbance conditions. The variations in the blade angle of attack for the passage of the disturbance are the likely mechanism for the increase in the deterministic sound seen in figure 6.17.

Probabilistic Pressure

The phase aligned streamwise turbulence normal stress compared to the probabilistic pressure is shown in figure 6.20a. There is an increase in both the broadband levels and around the blade passage frequencies after approximately 6.8 $U_\infty \tau / D$. In the flow measurements at the 70% radius this clearly corresponds to the increase in turbulence seen by the rotor. Towards the tip of the rotor (43 mm from the wall) there are increased turbulence levels starting around 4.5 $U_\infty \tau / D$. The largest increase in the overall sound pressure levels certainly appears to be when the rotor intersects the turbulence further away from the wall (89 mm from the wall) while there is some evidence of an increase in the probabilistic sound pressure resulting from the turbulence 43 mm from the wall.

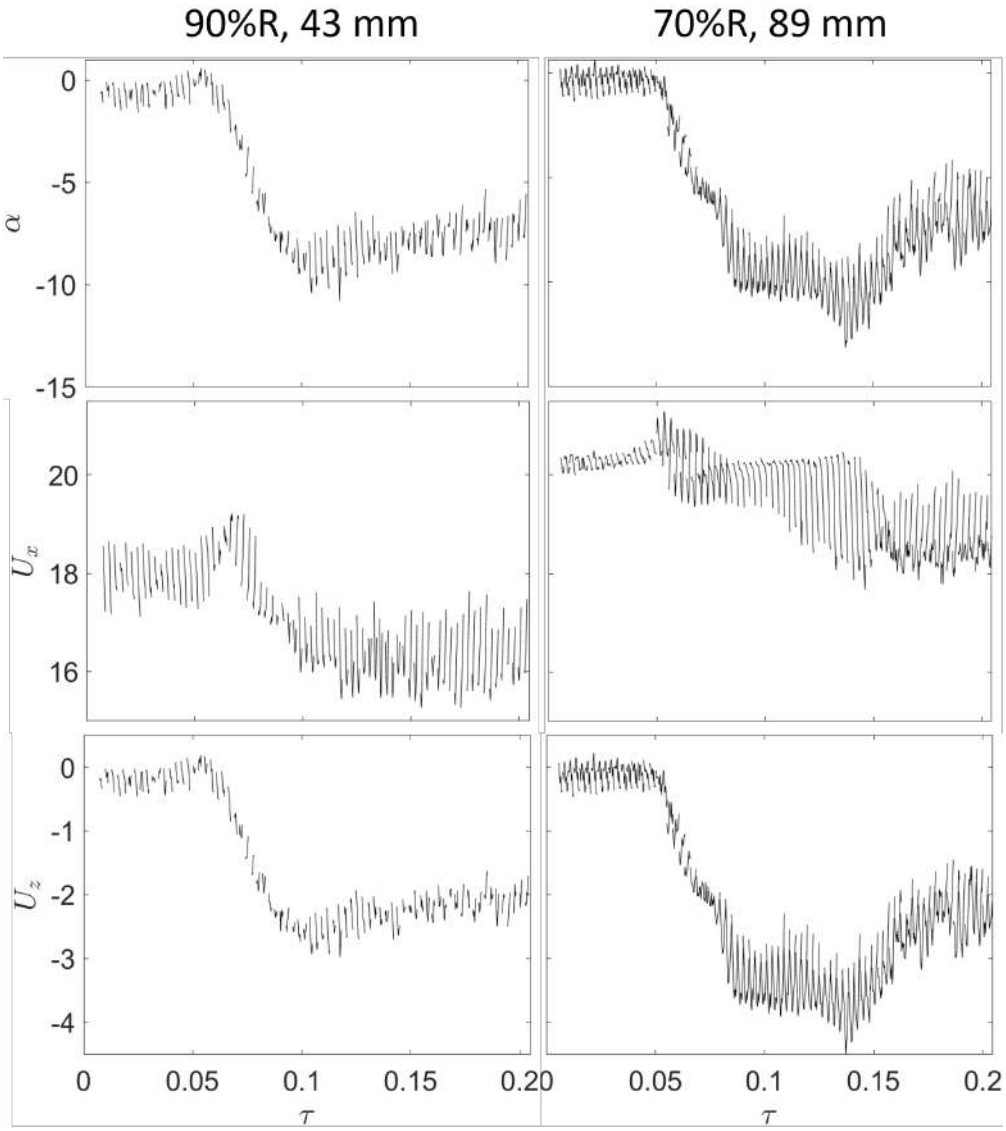

Figure 6.18: Velocities and flow angle seen by each blade as they pass through the measurement plane. The column on the left shows the 90% radius location 43 mm from the wall while the column on the right shows the 70% radius location 89 mm from the wall. The units for τ are in seconds, α in degrees, and U_x, U_z in m/s.

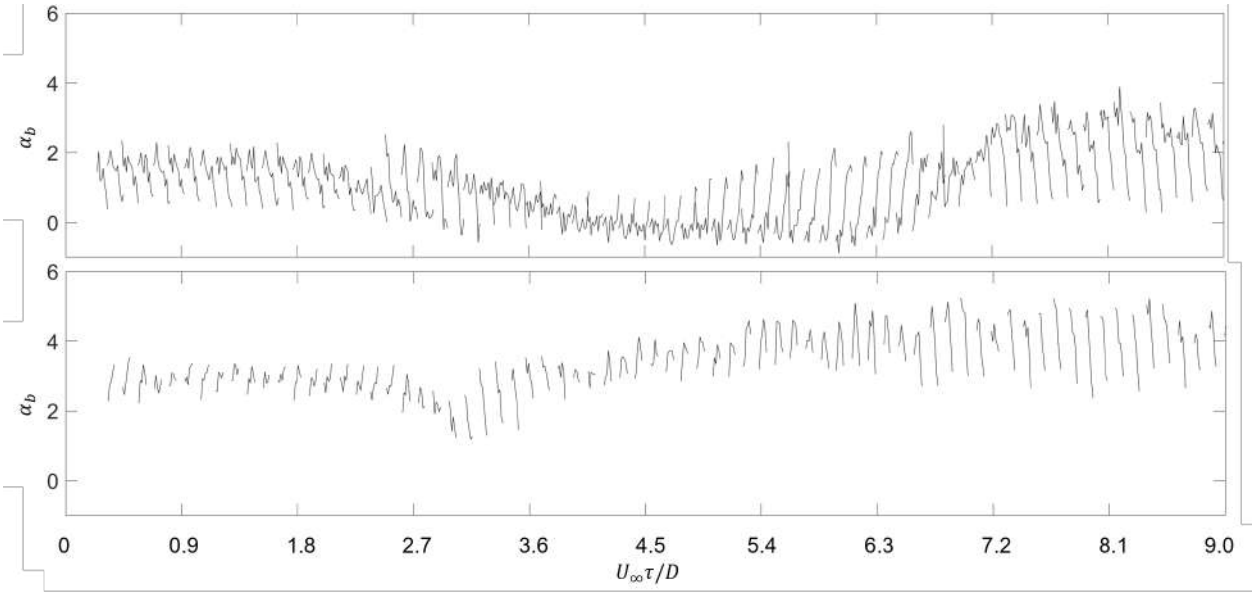

Figure 6.19: Phase averaged blade angles of attack measured at 70% radius (89 mm from the wall), and 90% radius (43 mm from the wall). α_b is in degrees, the time axis is normalized on the freestream velocity and the rotor diameter.

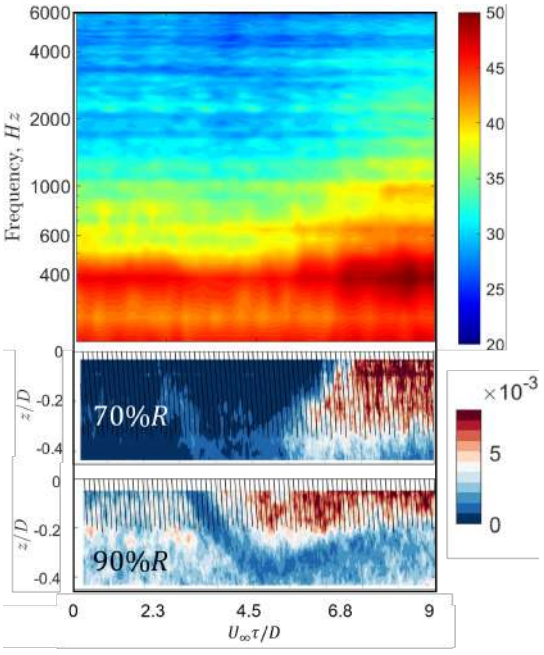

(a) $\langle \overline{u_x^2} \rangle / U_\infty$

Figure 6.20: Contours of the probabalistic part of the acoustic pressure signal compared to velocity measurements of the boundary layer 0.2 rotor diameters upstream of the rotor blade centerline. The time axis is normalized on the freestream velocity and rotor diameter.

6.7 Conclusion

The acoustics and flow characteristics of a rotor ingesting a planar boundary layer and periodic transient disturbances were measured. The transient disturbances were generated by an upstream appendage in the form of a 9" NACA 0021 airfoil actuated from 0^o to 20^o in 79 ms. Flow measurements were taken at a plane parallel to the wall 43 mm and 89 mm from the wall corresponding to 90% rotor radius and 70% rotor radius. Acoustic measurements were taken at microphones placed in the flow upstream of the rotor. The undisturbed flow at 90% radius was found to agree with the boundary layer probe data and the turbulence at the rotor inlet was shown to be unaffected by the rotor blade passage. To analyze the sound the sound pressure signal was broken down into the deterministic and probabilistic components. These were found to peak during different parts of the transient disturbance.

- The deterministic component was found to be the most prominent between 2.7 $U_\infty \tau/D$ and 7.2$U_\infty \tau/D$ and strongly correlated to the flow angle induced by the transient. Extending this analysis the blade angle of attack change as the transient passes through the rotor is shown and an increase in the angle of attack was noted during the transient. The increase in the deterministic sound is likely a form of unsteady loading in which the rotor blade experiences a change in angle of attack as each blade cuts the disturbance.

- The probabilistic component increases between 5.4 $U_\infty \tau/D$ and 7.2 $U_\infty \tau/D$ before reaching its steady state increase after 7.2 $U_\infty \tau/D$. This is attributed to airfoil separation that occurs when the disturbance generator exceeds 14^o angle of attack. The increased turbulence levels as a result of this separation increases the broadband sound and the sound about the fundamental and 2nd harmonics of the rotor blades. This mechanism seems more temporally aligned with the turbulence levels in the outer portion of the boundary layer which suggests that the sound is driven by the interaction between the rotor and the turbulence as it sweeps

away from the wall.

The extent to which the motion can be classified as unsteady was examined using a quasi-steady reconstruction of the flow and acoustics. This showed that there is a delay between when the airfoil reaches its critical separation angle of attack and when the turbulence levels are ingested by the rotor. This delay in the "switching on" of the separation demonstrates the unsteady behaviour of the flow and subsequent sound radiation as the rotor ingests the transient.

Funding Sources

The authors would like to thank the Office of Naval Research for sponsoring this work under grant N00014-20-1-2650, and specifically Drs. Yin Lu Young, Ki-Han Kim and John Muench.

Acknowledgments

Further acknowledgements go to Advait Borole, Agata Grzyb, Monica Shanmuga, and Derek Li, amongst others, for their assistance during the wind tunnel experiments. The authors would also like to thank Mr. Michael Marcolini for his ever present advice.

Chapter 7

Conclusions and Recommendations

7.1 Conclusions

In an attempt to provide insight into the impact of anisotropic, three dimensional flows on turbulence ingestion noise this dissertation presents measurements of two configurations. The first, a steady three dimensional flow developed over a body of revolution at angle of attack. The second, a transient three dimensional disturbance contained within a wall bounded boundary layer. In both cases the sound radiated by a rotor ingesting each flow was measured and links to the flow structure were inferred using flow measurements.

The flow about the body of revolution was shown to be characterized by three dimensional separation. On the port and starboard sides of the body a boundary layer embedded turbulent shear layer was shown to develop between 0.4δ and 0.7δ. Roll up of the turbulent kinetic energy sheet resulted in the development of a counterclockwise rotating vortex between the lee and starboard side of the body centered 23 mm from the body surface at a circumferential location of $\theta = 232^o$. It can be plausibly assumed that this vortex is mirrored on the port side based on the literature. The location of both the counter rotating vortices and the embedded shear layer were significant for sound production as they were within the rotor influence. This finding is consistent with numerous previous studies of bodies of revolution and slender bodies of revolution inclined at various angles of attack. Significant impacts to the structure of the turbulence in the flow surrounding the BOR result in directivities

and broadband noise contributions that could not be predicted by a homogenous turbulence assumption. Specifically modification of the structure of the turbulence was evident in the skewing and stretching of the zero time delay, two point correlation function on the lee side streamwise plane. In comparison the port side correlation function was less stretched than the lee side with a length scale ratio of 1.8. Surprisingly the structure of the zero time delay, two point correlation function in the $r - \theta$ plane appeared isotropic. Regardless of the location of the anchor point the function was circular and the length scales were similar at all points, and in both directions, within the boundary layer. Proper orthogonal decomposition of a surface normal velocity profile taken at the tail exit on the lee and port side showed the port side modes are dominated by the fluctuations within the embedded shear layer, while the lee side modes span much of the boundary layer. Compact eddy structures on the port side appeared to be stretched versions of an equilibrium boundary layer. CES modes on the lee side have a structural inclination that matches the zero time delay, two point correlation function when normalized on the boundary layer thickness and edge velocity.

The impact of the shear layer and vortices on the sound was significant, an increase both in the overall broadband sound and the haystack intensities is evident relative to the zero degree angle of attack measurements done by Balantrapu [14] and Hickling [47]. The interaction of the rotor with the vortex should have produced a tonal response, however, this effect was dominated by the turbulence ingestion noise and was negligible for this angle of attack. The directivity of the sound radiated by the rotor is also affected. An increase of approximately 7-10 dB was measured between the array on the lee side and the array on the starboard side at a zero thrust advance ratio.

The transient sound and flow measurements in the second configuration showed that there are significant differences between the quasi steady reconstruction and the unsteady measurements in both the sound and flow. This indicates that the flow is truly unsteady and

cannot be described as quasi-steady. The measurements further revealed a deterministic sound source at the blade passage frequency that aligned well with the change in the blade angle of attack as it interacts with the disturbance. This source is tonal in nature and is identified as a form of unsteady loading. The blades interact with the disturbance coherently at the blade passage frequency and the lift for each blade changes sharply as it moves through the disturbance resulting in coherence between blades at the blade passage frequency. The probabilistic sound spectrum is shown to increase during the interaction of the latter portions of the ramp motions and is closely associated with an increase in the streamwise fluctuations. It is also more closely associated with the turbulence in the outer region of the boundary layer. These two results demonstrate the identification of two types of sound and their associated flow characteristics prominent in transient turbulence ingestion.

This dissertation has given insight into the coupling of the rotor interaction with the disturbance phase and shown that the interaction can have a tonal response even if the interaction is not cyclically identical in time. Additionally it has shown that an interaction that could be expected to be tonal, such as the interaction between a rotor and the organized vortices shown in Chapters 4 and 5, can be dominated by the stochastic interaction between the boundary layer turbulence and rotor. It has addressed currently unresolved issues in the literature by examining the phase coupling of an unsteady disturbance with a rotor and its impact on the noise radiated during the transient. The efficacy of the homogenous turbulence assumption in noise predictions for real world rotor interactions has been challenged and demonstrated that sufficiently anisotropic and unsteady flow fields result in sound fields that are not predictable with the analytical methods currently available.

7.2 Recommendations

Further research into documenting the sound directivity around the body of revolution, both in two and three dimensions, is necessary to further improve the understanding of how the turbulent structure as a result of the bodies inclination affects the sound radiated. Also worth consideration is the point at which the vortices generated by the three dimensional separation become relevant to the sound spectra. The measurements within this dissertation show that at this angle of attack and Reynolds number they are more or less negligible when compared to the turbulence ingestion noise. However the literature shows a positive correlation between the vortex strength, angle of attack, and Reynolds number so there may be a point at which the rotor interaction with the vortices is sufficient to produce identifiable tones in the sound spectra.

The ability of the existing anisotropic turbulence correlation models such as those of Glegg et al. [39] and Catlett et al. [24] are not able to make predictions for transient ingestion. Further modelling efforts are therefore required for which the data in this dissertation can serve as validation. Further experimental research is also required of smaller time scale disturbances than those investigated in Chapter 6.

Bibliography

[1] R. J. Adrian. *Stochastic Estimation of the Structure of Turbulent Fields*, pages 145–195. Springer Vienna, Vienna, 1996. ISBN 978-3-7091-2676-9. doi: https://doi.org/10.1007/978-3-7091-2676-9_3.

[2] S. K. Ahn. *An experimental study of flow over a 6 to 1 prolate spheroid at incidence*. PhD Dissertation, Virginia Tech, 1992.

[3] W. N. Alexander, W. J. Devenport, M.A. Morton, and S.A.L. Glegg. *Noise from a Rotor Ingesting a Planar Turbulent Boundary Layer*. American Institute of Aeronautics and Astronautics Inc., Berlin, 2013. doi: https://doi.org/10.2514/6.2013-2285.

[4] W. N. Alexander, W. J. Devenport, D. Wisda, M. A. Morton, and S. A. L. Glegg. *Sound Radiated from a Rotor and Its Relation to Rotating Frame Measurements of Ingested Turbulence*. American Institute of Aeronautics and Astronautics Inc., Atlanta, GA, 2014. doi: https://doi.org/10.2514/6.2014-2746.

[5] W. N. Alexander, W. J. Devenport, and S. A. L. Glegg. Noise from a rotor ingesting a thick boundary layer and relation to measurements of ingested turbulence. *Journal of Sound and Vibration*, 409:227–240, 2017. ISSN 0022460X. doi: https://doi.org/10.1016/j.jsv.2017.07.056.

[6] W. N. Alexander, W. J. Devenport, N. J. Molinaro, N. A. Balantrapu, C. Hickling, S. A. L. Glegg, and J. Pectol. *Turbulence Ingestion Noise from an Open Rotor with Different Inflows*, pages 113–129. Springer International Publishing, Cham, 2018. ISBN 978-3-319-76780-2.

[7] J. M. Anderson, M. R. Catlett, and D. Stewart. *Modeling Rotor Unsteady Forces and Sound due to Ingestion of Spatially Inhomogeneous Turbulence*. American Institute of Aeronautics and Astronautics Inc., Atlanta, GA, 2014. doi: https://doi.org/10.2514/6.2014-2607.

[8] J. M. Anderson, M. R. Catlett, and D. Stewart. Modeling rotor unsteady forces and sound due to homogeneous turbulence ingestion. *AIAA Journal*, 53(1):81–92, 2015. ISSN 0001-1452 1533-385X. doi: https://doi.org/10.2514/1.j052874.

[9] J. M. Anderson, A. Buono, and M. R. Catlett. *Airfoil Unsteady Loading and Sound Radiation due to Incident and Self-Generated Turbulent Flows*. American Institute of Aeronautics and Astronautics Inc., Lyon, France, 2016. doi: https://doi.org/10.2514/6.2016-2735.

[10] A. Ashok and A. J. Smits. *The turbulent wake of a submarine model in pitch and yaw*. American Institute of Aeronautics and Astronautics Inc., Grapevine TX, 2013. doi: https://doi.org/10.2514/6.2013-1121.

[11] A. Ashok, T. Van Buren, and A. J. Smits. Asymmetries in the wake of a submarine model in pitch. *Journal of Fluid Mechanics*, 774:416–442, 2015. ISSN 0022-1120 1469-7645. doi: https://doi.org/10.1017/jfm.2015.277.

[12] H. M. Atassi and M.M. Logue. *Fan Broadband Noise in Anisotropic Turbulence*. American Institute of Aeronautics and Astronautics Inc., Miami, Florida, 2009. doi: https://doi.org/10.2514/6.2009-3148.

[13] Joby Aviation. Joby delivers first evtol aircraft to edwards air force base ahead of schedule, 2023. URL https://www.jobyaviation.com/news/joby-delivers-first-evtol-edwards/.

[14] A. N. Balantrapu. *The Space-time Structure of an Axisymmetric Turbulent Boundary Layer Ingested by a Rotor*. PhD Dissertation, Virginia Tech, 2021.

[15] A. N. Balantrapu, C. Hickling, N. Alexander, and W. Devenport. The structure of a highly-decelerated axisymmetric turbulent boundary layer. *Journal of Fluid Mechanics*, 929:A9, 2021. doi: https://doi.org/10.1017/jfm.2021.845.

[16] J. T. Banks, H. Butt, W. N. Alexander, and W. J. Devenport. *Turbulence Ingestion of a Non-Axisymmetric Wake by an Open Rotor*. American Institute of Aeronautics and Astronautics Inc., Southampton, 2022.

[17] J. T. Banks, H. Butt, W. N. Alexander, and W. J. Devenport. Turbulence ingestion of an axisymmetric and non-axisymmetric wake into an open rotor. *Journal of Fluid Mechanics (under review)*, 2024.

[18] G. K. Batchelor and I. Proudman. The effect of rapid distortion on a fluid in turbulent motion. *Quarterly Journal of Applied Mathematics*, 7(1):83–103, 1954. doi: https://doi.org/10.1093/qjmam/7.1.83.

[19] G. Berkooz, P. Holmes, and J. L. Lumley. The proper orthogonal decomposition in the analysis of turbulent flows. *Annual Review of Fluid Mechanics*, 25(1):539–575, 1993. doi: https://doi.org/10.1146/annurev.fl.25.010193.002543.

[20] W. Blake. *Mechanics of Flow Induced Sound and Vibration*. Elsevier Inc., 2017. ISBN 978-0-12-809273-6.

[21] K. S. Brentner. Prediction of helicopter rotor discrete frequency noise for three scale models. *Journal of Aircraft*, 25(5):420–427, 1988. ISSN 0021-8669 1533-3868. doi: https://doi.org/10.2514/3.45598.

[22] Kenneth S. Brentner and Henry E. Jones. *Noise prediction for maneuvering rotorcraft*. 6th Aeroacoustics Conference and Exhibit. American Institute of Aeronautics and Astronautics Inc., Lahaina, HI, USA, 2000.

[23] G. A. Bres, K. S. Brentner, G. Perez, and H. E. Jones. Maneuvering rotorcraft noise prediction. *Journal of Sound and Vibration*, 275(3-5):719–738, 2004. ISSN 0022460X. doi: https://doi.org/10.1016/j.jsv.2003.07.005.

[24] M. Catlett, J. M. Anderson, and D. Stewart. *Aeroacoustic Response of Propellers to Sheared Turbulent Inflow*. American Institute of Aeronautics and Astronautics Inc., Colorado Springs, Colorado, 2012. doi: https://doi.org/10.2514/6.2012-2137.

[25] H. Chen, K. S. Brentner, L. V. Lopes, and J. F. Horn. *A study of rotorcraft noise prediction in maneuvering flight*, pages 9549–9563. American Institute of Aeronautics and Astronautics Inc., Reno, NV, USA, 2004.

[26] C. Chesnakas. Three-dimensional velocity measurements on a 6:1 prolate spheroid at 10 degree angle of attack. Report, Department of Aerospace and Ocean Engineering, Virginia Tech, 1994.

[27] C. Chesnakas and R. Simpson. Measurements of the turbulence structure in the vicinity of a 3-d separation. *Journal of Fluid Mechanics*, 118:268–275, 1996. doi: https://doi.org/10.1115/1.2817373.

[28] C. Chesnakas and R. L. Simpson. Full three-dimensional measurements of the cross-flow separation region of a 6:1 prolate spheroid. *Experiments in Fluids*, 17:68–74, 1994. doi: https://doi.org/10.1007/BF02412805.

[29] C. J. Chesnakas and R. L. Simpson. Detailed investigation of the three-dimensional

separation about a 6:1 prolate spheroid. *AIAA Journal*, 35(6):990–999, 1997. doi: https://doi.org/10.2514/2.208.

[30] K. Choi and R. Simpson. Some mean velocity, turbulence, and unsteadiness characteristics of the vpisu stability wind tunnel. Report, Department of Aerospace and Ocean Engineering, Virginia Tech, 1987.

[31] W. J. Devenport, C. Muthanna, R. L. Ma, and S. A. L. Glegg. Two-point descriptions of wake turbulence with application to noise prediction. *AIAA Journal*, 39(12):2302–2307, 2001. doi: https://arc.aiaa.org/doi/abs/10.2514/2.1235.

[32] W. J. Devenport, R. A. Burdisso, A. Borgoltz, P. A. Ravetta, M. F. Barone, K. A. Brown, and M. A. Morton. The kevlar-walled anechoic wind tunnel. *Journal of Sound and Vibration*, 332(17):3971–3991, 2013. doi: https://doi.org/10.1016/j.jsv.2013.02.043.

[33] E. A. Eichelbrenner and A. Oudart. Methode de calcul de la couche-limite tridimensionelle. *Office National d'Etudes et de Recherches Aeronautiques*, 76, 1955.

[34] F. Farassat and G. P. Succi. A review of propeller discrete frequency noise prediction technology with emphasis on two current methods for time domain calculations. *Journal of Sound and Vibration*, 71(3):399–419, 1980. doi: https://doi.org/10.1016/0022-460X(80)90422-8.

[35] S. Glegg, M.A. Morton, and W.J. Devenport. *Rotor Inflow Noise Caused by a Boundary Layer: Theory and Examples*. American Institute of Aeronautics and Astronautics Inc., Colorado Springs, Colorado, 2012.

[36] S. Glegg, J. Grant, H. Murray, W. Devenport, and N. Alexander. *Sound Radiation from a Rotor Operating at High Thrust Near a Wall*. American Institute of Aeronautics and Astronautics Inc., Lyon, France, 2016.

[37] S. A. Glegg, C. Hickling, N. A. Balantrapu, J. T. Banks, H. Butt, W. N. Alexander, and W. J. Devenport. *Beamforming of Broadband Rotor Noise*. American Institute of Aeronautics and Astronautics Inc., 2021. doi: https://doi.org/10.2514/6.2021-2189.

[38] S. A. L. Glegg and W. J. Devenport. Proper orthogonal decomposition of turbulent flows for aeroacoustic and hydroacoustic applications. *Journal of Sound and Vibration*, 239(4):767–784, 2001. doi: https://doi.org/10.1006/jsvi.2000.3128.

[39] S. A. L. Glegg, W. J. Devenport, and W. N. Alexander. Broadband rotor noise predictions using a time domain approach. *Journal of Sound and Vibration*, 335:115–124, 2015. doi: https://doi.org/10.1016/j.jsv.2014.09.007.

[40] S.A.L. Glegg, K. S. Wittmer, W.J. Devenport, and D. S. Pope. *Broadband Helicopter Noise Generated by Blade-Wake Interactions*. American Helicopter Society, Williamsburg, Virginia, 1997. doi: https://doi.org/10.4050/JAHS.44.293.

[41] M.E. Goldstein. *Aeroacoustics*. McGraw-Hill International Book Company, 1976. ISBN 9780070236851.

[42] J.M.R. Graham. The effect of a two-dimensional cascade of thin streamwise plates on homogeneous turbulence. *Journal of Fluid Mechanics*, 356:125–147, 1998. doi: https://doi.org/10.1017/S0022112097007799.

[43] D.B. Hanson. Spectrum of rotor noise caused by atmospheric turbulence. *Journal of the Acoustical Society of America*, 56(1):110–136, 1974. doi: https://doi.org/10.1121/1.1903241.

[44] R. P. Harrington. *An Attack on the Origin of Lift of an Elongated Body*. Daniel Guggenheim Airship Institute, 1935.

[45] J. Val. Healey. Establishing a database for flight in the wakes of structures. *Journal of Aircraft*, 29(4):559–564, 1992. doi: https://doi.org/10.2514/3.46202.

[46] C. C. Hennes, H. Chen, K. S. Brentner, S. Ananthan, and G. Leishman. *Influence of transient flight maneuvers on rotor wake dynamics and noise radiation*, pages 607–624. American Helicopter Society, San Francisco, CA, United states, 2004.

[47] C. Hickling. *Inhomogeneous, Anisotropic Turbulence Ingestion Noise in Two Open Rotor Configurations*. PhD Dissertation, Virginia Tech, 2020.

[48] C. Hickling, A. N. Balantrapu, A. J. Millican, N. Alexander, W. Devenport, and S. Glegg. *Turbulence Ingestion into a Rotor at the Rear of an Axisymmetric Body*. American Institute of Aeronautics and Astronautics Inc., Delft, The Netherlands, 2019.

[49] E. Huse. Propeller-hull vortex cavitations. *Norw. Ship Model Exp. Tank*, 19(212), 1971.

[50] S. A. Huyer and D. Beal. A turbulent inflow model based on velocity modulation. *Journal of Sound and Vibration*, 308(1-2):28–43, 2007. doi: https://doi.org/10.1016/j.jsv.2007.06.051.

[51] S. A. Huyer and S. R. Snarski. Analysis of a turbulent propeller inflow. *Journal of Fluids Engineering*, 125(3):533, 2003. ISSN 00982202. doi: https://doi.org/10.1115/1.1570860.

[52] C. W. Jiang, M. S. Chang, and Y. N. Liu. The effect of turbulence ingestion on propeller broadband thrust. Report, David Taylor Research Center, 1991.

[53] M. K Johns and J. Val. Healey. The airwake of a dd-963 class destroyer. *Naval Engineers Journal*, 101(3):36–42, 1989. doi: https://doi.org/10.1111/j.1559-3584.1989.tb02184.x.

[54] P. Kumar and J. K. Prasad. Side force over slender body with rings at different location at subsonic speed. *Proceedings of the Institution of Mechanical Engineers, Part G:*

Journal of Aerospace Engineering, 231(8):1478–1491, 2016. ISSN 0954-4100 2041-3025. doi: https://doi.org/10.1177/0954410016654180.

[55] R. G. Lee and S. J. Zan. Unsteady aerodynamic loading on a helicopter fuselage in a ship airwake. *Journal of the American Helicopter Society*, 49(2):149–159, 2004. doi: https://doi.org/10.4050/JAHS.49.149.

[56] G. Leishman. *Principles of Helicopter Aerodynamics*. Cambridge University Press, Cambridge, UK, 2000. ISBN 978-0-521-85860-1.

[57] J. W. Leverton and F. W. Taylor. Helicopter blade slap. *Journal of Sound and Vibration*, 4:345–357, 1966. doi: https://doi.org/10.1016/0022-460X(66)90132-5.

[58] H. W. Liepmann, J. Laufer, and K. Liepmann. On the spectrum of isotropic turbulence. Report, NACA, 1951.

[59] A. Lloyd and L. Campbell. *Experiments to investigate the vortices shed from a submarine-like body of revolution*. Advisory Group for Aerospace Research and Development, Southampton, 1986.

[60] D. A. III Lynch, W. K. Blake, and T. J. Mueller. Turbulence correlation length-scale relationships for the prediction of aeroacoustic response. *AIAA Journal*, 43(6):1187–1197, 2005. doi: https://doi.org/10.2514/1.2200.

[61] D. A. III Lynch, W. K. Blake, and T. J. Mueller. Turbulent flow downstream of a propeller, part 1: Wake turbulence. *AIAA Journal*, 43(6):1198–1210, 2005. doi: https://doi.org/10.2514/1.2435.

[62] D. A. III Lynch, W. K. Blake, and T. J. Mueller. Turbulent flow downstream of a propeller, part 2: Ingested, propeller-modified turbulence. *AIAA Journal*, 43(6):1211–1220, 2005. doi: https://doi.org/10.2514/1.2439.

[63] D.A. III Lynch. *An Experimental Investigation of the Unsteady Response of a Stator Located Downstream of a Propeller Ingesting Broadband Turbulence*. PhD Dissertation, University of Notre Dame, 2001.

[64] S. J. Majumdar and N. Peake. Noise generation by the interaction between ingested turbulence and a rotating fan. *Journal of Fluid Mechanics*, 359:181–216, 1998. doi: https://doi.org/10.1017/S0022112097008318.

[65] R. Martinez. Asymptotic theory of broadband rotor thrust, part i: Manipulations of flow probabilities for a high number of blades. *Transactions of the ASME*, 63:136–142, 1996. doi: https://doi.org/10.1115/1.2787188.

[66] R. Martinez. Asymptotic theory of broadband rotor thrust, part ii: Analysis of the right frequency shift of the maximum response. *Journal of Applied Mechanics*, 63:143–148, 1996. doi: https://doi.org/10.1115/1.2787189.

[67] N. J. Molinaro, A. N. Balantrapu, C. Hickling, W. N. Alexander, W. J. Devenport, and S. A. Glegg. *The Ingestion of Wake Turbulence into an Open Rotor*. American Institute of Aeronautics and Astronautics Inc., Denver CO, 2017. doi: https://doi.org/10.2514/6.2017-3868.

[68] M. A. Morton, W. J. Devenport, and S. A. L. Glegg. *Rotor Inflow Noise Caused by a Boundary Layer: Inflow Measurements and Noise Predictions*. American Institute of Aeronautics and Astronautics Inc., Colorado Springs, Colorado, 2012. doi: https://doi.org/10.2514/6.2012-2120.

[69] M.A. Morton. *Rotor Inflow Noise Caused by a Boundary Layer: Inflow Measurements and Noise Predictions*. M.S. Thesis, Virginia Polytechnic Institute and State University, 2012.

[70] J. D. Muench. *Periodic Acoustic Radiation from a Low Aspect Ratio Propeller*. PhD Dissertation, University of Rhode Island, 2001.

[71] H. Murray, D. Wisda, N. Alexander, M. A. Nelson, W. J. Devenport, and S. Glegg. *Sound and Distortion Produced by a Braking Rotor Operating in a Planar Boundary Layer with Application to Wind Turbines*. American Institute of Aeronautics and Astronautics Inc., Dallas, TX, 2015. doi: https://doi.org/10.2514/6.2015-2682.

[72] H. Murray, W. Devenport, N. Alexander, S. Glegg, and D. Wisda. Aeroacoustics of a rotor ingesting a planar boundary layer at high thrust. *Journal of Fluid Mechanics*, 850:212–245, 2018. doi: https://doi.org/10.1017/jfm.2018.438.

[73] Y. Nacakli. *Analysis of Helicopter Downwash/Frigate Airwake Interaction Using Statistically Designed Experiments*. PhD Dissertation, Old Dominion University, 2010.

[74] S. T. Palanganda. *Design and Analysis of a Deterministic Disturbance Generator*. M.S. Thesis, Virginia Tech, 2023.

[75] P. E. Roach. The generation of nearly isotropic turbulence by means of grids. *Heat and Fluid Flow*, 8(2):83–92, 1987. doi: https://doi.org/10.1016/0142-727X(87)90001-4.

[76] E. J. Rodgers. Real flow over a body of revolution at angle of attack. Report, Ordnance Research Laboratory, May 28 1968 1953.

[77] D. F. Scharpf and T. J. Mueller. An experimental investigation of the sources of propeller noise due to the ingestion of turbulence at low speeds. *Experiments in Fluids*, 18:277–287, 1995. doi: https://doi.org/10.1007/BF00195098.

[78] D. M. Schatzman and F. O. Thomas. An experimental investigation of an unsteady adverse pressure gradient turbulent boundary layer: embedded shear layer scaling.

Journal of Fluid Mechanics, 815:592–642, 2017. ISSN 0022-1120 1469-7645. doi: https://doi.org/10.1017/jfm.2017.65.

[79] M. Sevik. Sound radiation from subsonic rotor subjected to turbulence. *Fluid Mech., Acoustics, and Design of Turbomachinery*, pages 493–512, 1974. NASA-SP-304.

[80] S. Shukla, S. S. Sinha, and S. N. Singh. Ship-helo coupled airwake aerodynamics: A comprehensive review. *Progress in Aerospace Sciences*, 106:71–107, 2019. ISSN 03760421. doi: https://doi.org/10.1016/j.paerosci.2019.02.002.

[81] A. Spence and W.J.G. Trebble. *Low Speed Tunnel Tests on the Flow Structure Behind a Body of Revolution of Fineness Ratio 162/3:1.* Royal Airforce Establishment, 1955.

[82] K. R. Sreenivasan and R. Narasimha. Rapid distortion of axisymmetric turbulence. *Journal of Fluid Mechanics*, 84(3):497–516, 2006. ISSN 0022-1120 1469-7645. doi: https://doi.org/10.1017/s0022112078000294.

[83] B. E. Tinling and Q. A. Clyde. An investigation of the normal-force and vortex-wake characteristics of an ogive-cylinder body at subsonic speeds. *NASA Technical Note D-1297*, 1962.

[84] M. Wang and Di Zhou. Flow over a body of revolution at nonzero angles of attack from rans simulations, August 24 2020. Personal Communication.

[85] J.E. F. Williams and D. L. Hawkings. Sound generation by turbulence and surfaces in arbitrary motion. *Philosophical Transactions of the Royal Society of London A: Mathematical, Physical and Engineering Sciences*, 264(1151):321–342, 1969. ISSN 1364-503X.

[86] D. Wisda, H. Murray, N. Alexander, M. A. Nelson, W. J. Devenport, and S. Glegg. *Flow Distortion and Noise Produced by a Thrusting Rotor Ingesting a Planar Turbulent*

Boundary Layer. American Institute of Aeronautics and Astronautics Inc., Dallas, TX, 2015.

[87] K. S. Wittmer and W.J. Devenport. *Interaction of a Streamwise Vortex with a Full-Span Blade*. American Institute of Aeronautics and Astronautics Inc., San Diego, California, 1995.

[88] K. S. Wittmer and W.J. Devenport. Effects of perpendicular blade-vortex interaction, part 1: Turbulence structure and development. *AIAA Journal*, 37(7):805–812, 1999. doi: https://doi.org/10.2514/2.7527.

[89] K. S. Wittmer, W. J. Devenport, and S. A. L. Glegg. Effects of perpendicular blade-vortex interaction, part 2: Parameter study. *AIAA Journal*, 37(7):813–817, 1999. doi: https://doi.org/10.2514/2.7528.

[90] J. P. Wojno. *An Experimental Investigation of the Aeroacoustic Response of a Ten-Bladed Rotor Ingesting Grid-Generated Turbulence*. PhD Dissertation, University of Notre Dame, 1999.

[91] J. P. Wojno, T. J. Mueller, and W. Blake. Turbulence ingestion noise, part 1: Experimental characterization of grid-generated turbulence. *AIAA Journal*, 40(1):16–25, 2002. doi: https://doi.org/10.2514/2.1636.

[92] D. Zhou, K. Wang, and M. Wang. *Computational Analysis of Noise Generation by a Rotor at the Rear of an Axisymmetric Body of Revolution*. American Institute of Aeronautics and Astronautics Inc., 2022. doi: https://doi.org/10.2514/6.2022-3090.

Appendices

Appendix A

Additional Figures: Transient flow

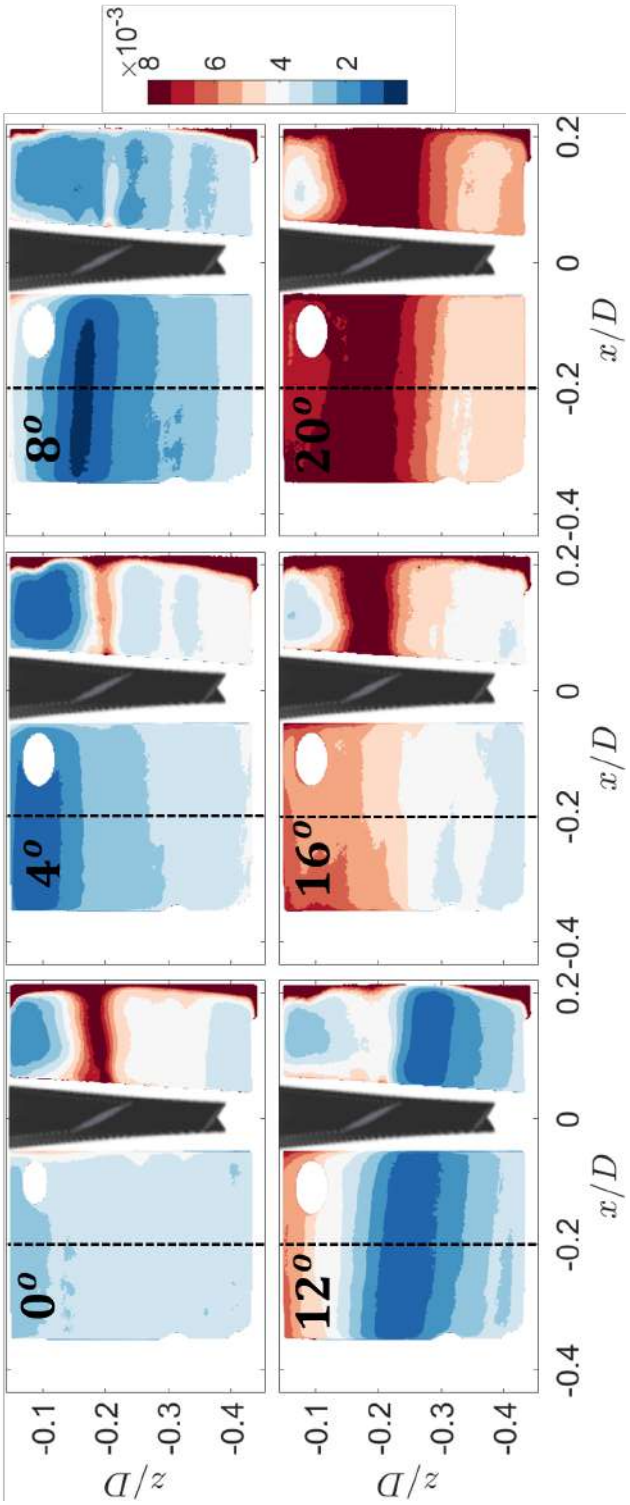

Figure A.1: Mean streamwise fluctuations, $\overline{u_x^2}/U_\infty^2$, for disturbance generator stationary angles of attack.

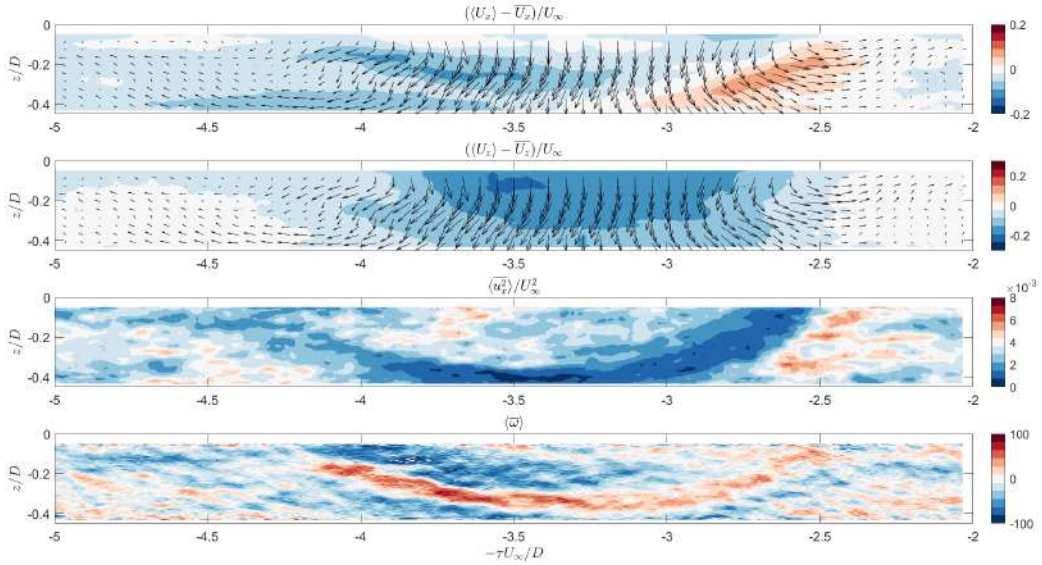

Figure A.2: Phase averaged, mean subtracted time series for the 63 ms flap motion taken 43 mm from the wall. The time is normalized on the freestream velocity and rotor diameter. Vectors of the velocity are shown overlaid on the U_x and U_z plots.

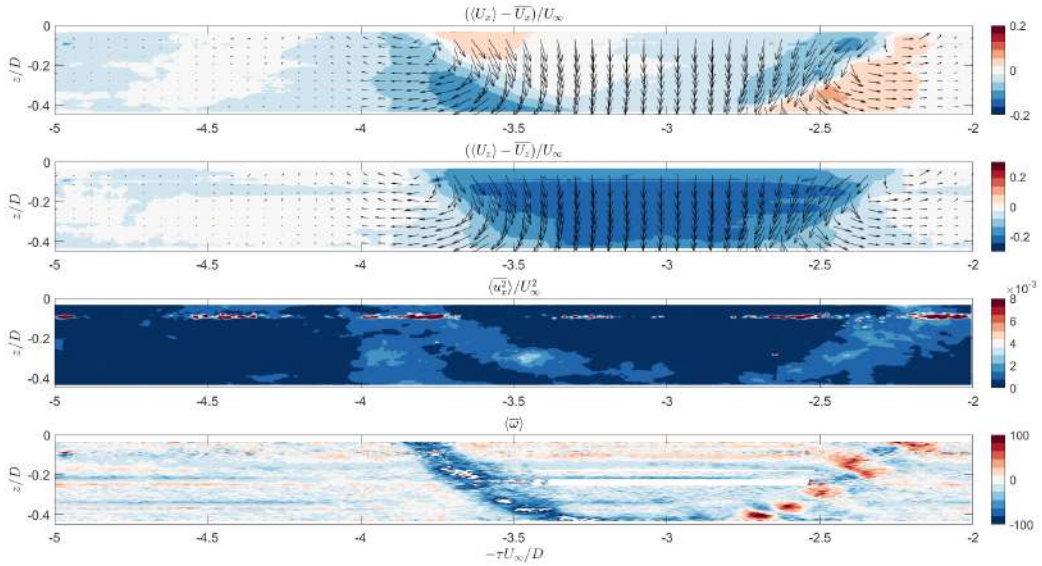

Figure A.3: Phase averaged, mean subtracted time series for the 63 ms flap motion taken 89 mm from the wall. The time is normalized on the freestream velocity and rotor diameter. Vectors of the velocity are shown overlaid on the U_x and U_z plots.

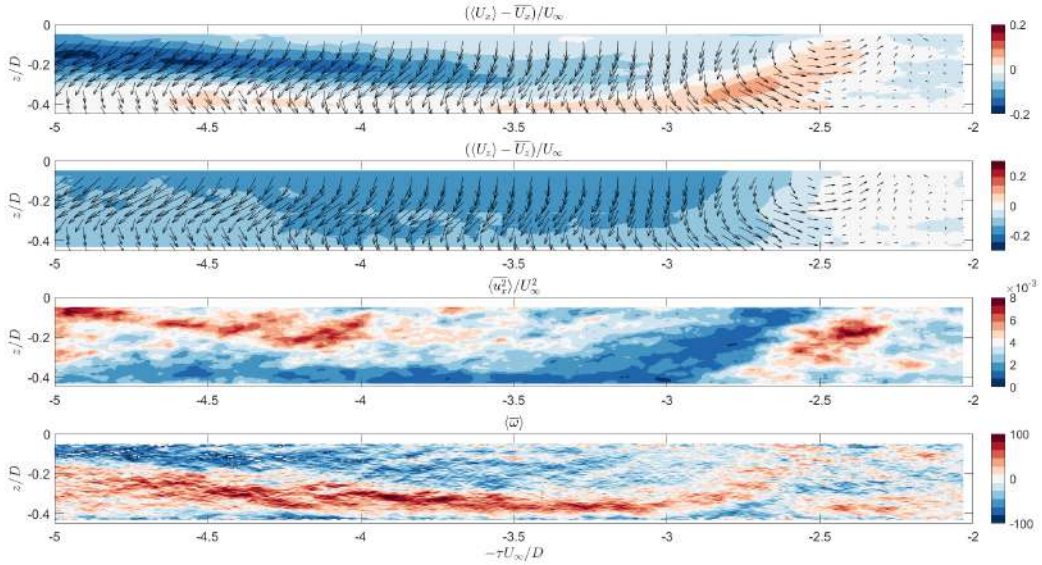

Figure A.4: Phase averaged, mean subtracted time series for the 37 ms ramp motion taken 43 mm from the wall. The time is normalized on the freestream velocity and rotor diameter. Vectors of the velocity are shown overlaid on the U_x and U_z plots.

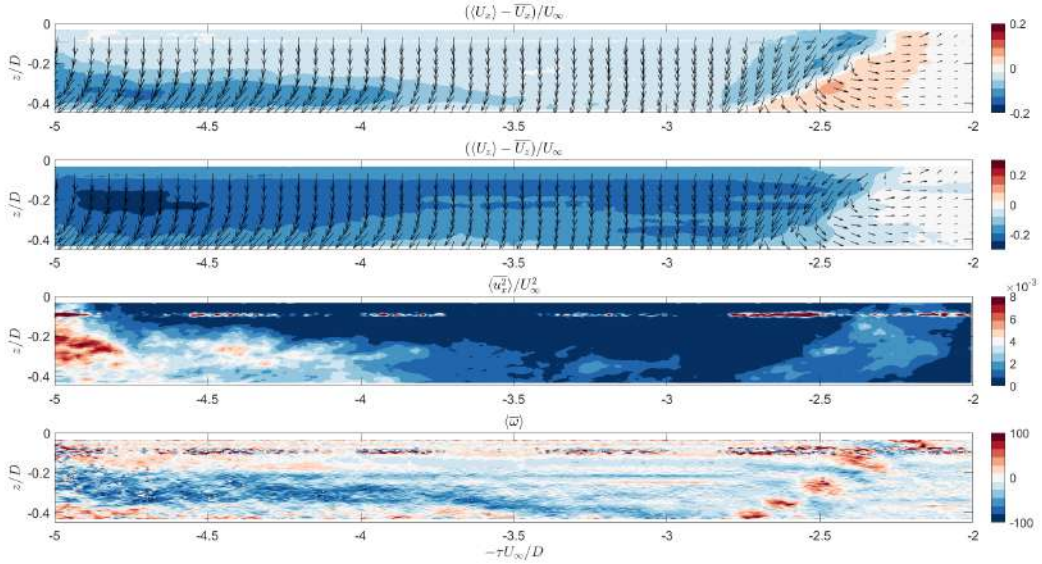

Figure A.5: Phase averaged, mean subtracted time series for the 37 ms ramp motion taken 89 mm from the wall. The time is normalized on the freestream velocity and rotor diameter. Vectors of the velocity are shown overlaid on the U_x and U_z plots.

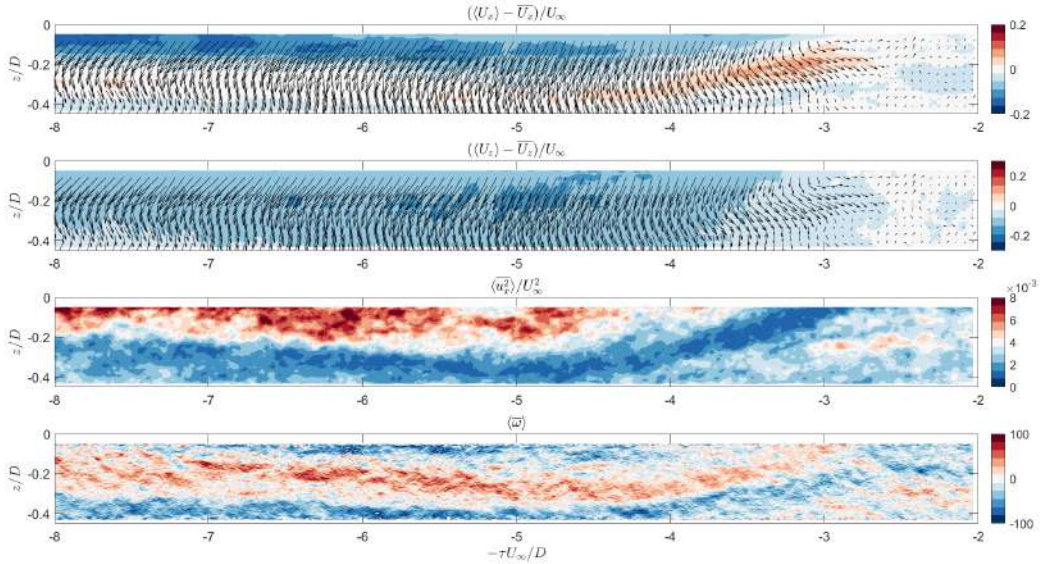

Figure A.6: Phase averaged, mean subtracted time series for the 151 ms flap motion taken 43 mm from the wall. The time is normalized on the freestream velocity and rotor diameter. Vectors of the velocity are shown overlaid on the U_x and U_z plots.

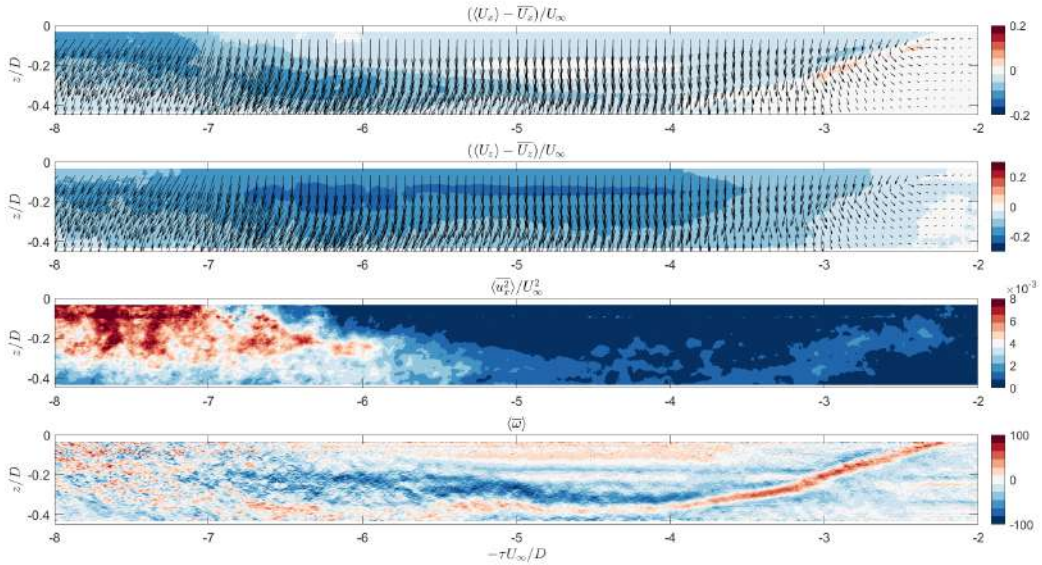

Figure A.7: Phase averaged, mean subtracted time series for the 151 ms flap motion taken 89 mm from the wall. The time is normalized on the freestream velocity and rotor diameter. Vectors of the velocity are shown overlaid on the U_x and U_z plots.